2-2013

Investigations of Surface-Tension Effects Due to Small-Scale Complex Boundaries

Jiansheng Feng
University of Massachusetts Amherst, jianshen@physics.umass.edu

INVESTIGATIONS OF SURFACE-TENSION EFFECTS DUE TO SMALL-SCALE COMPLEX BOUNDARIES

A Dissertation Presented

by

JIANSHENG FENG

Submitted to the Graduate School of the
University of Massachusetts Amherst in partial fulfillment
of the requirements for the degree of

DOCTOR OF PHILOSOPHY

February 2013

Physics

INVESTIGATIONS OF SURFACE-TENSION EFFECTS DUE TO SMALL-SCALE COMPLEX BOUNDARIES

A Dissertation Presented

by

JIANSHENG FENG

Approved as to style and content by:

Jonathan P. Rothstein, Co-chair

Mark T. Tuominen, Co-chair

Narayanan Menon, Member

Ryan C. Hayward, Member

Donald Candela, Department Chair
Physics

ACKNOWLEDGMENTS

I would like to acknowledge my graduate research advisor, Professor Jonathan Rothstein, for giving me the opportunity to do research in his lab, for allowing me the freedom to study problems I am interested in, and for the many years of mentoring. I would like to thank my co-advisor, Professor Mark Tuominen, for opening the door of nanotechnology for me and giving me the opportunity to practice and develop my skills. I also want to thank my other committee members, Professor Narayanan Menon, for teaching me new intuitions on the fundamental concepts in physics, and Professor Ryan Hayward, for introducing me to the world of interfacial phenomena.

To my parents who have made all the experiences of my life possible, who teach me to be a good person, who allow me to pursue my dreams, I will be forever grateful.

This thesis represents several years of my efforts, and I appreciate anyone who takes the time to read it through.

ABSTRACT

INVESTIGATIONS OF SURFACE-TENSION EFFECTS DUE TO SMALL-SCALE COMPLEX BOUNDARIES

FEBRUARY 2013

JIANSHENG FENG

B.S., UNIVERSITY OF SCIENCE AND TECHNOLOGY OF CHINA

M.S., UNIVERSITY OF MASSACHUSETTS AMHERST

Ph.D., UNIVERSITY OF MASSACHUSETTS AMHERST

Directed by: Professor Jonathan P. Rothstein and Professor Mark T. Tuominen

The earliest man-made irrigation systems in recorded history date back to the ancient Egypt and Mesopotamia era. After thousands of years of experience, exploration, and experimenting, mankind have learned how to construct canals and dams and use pipes and pumps to direct and control water flow, but till this day, there are still some behaviors of water and other simple fluids that surprise us. One such example is the lotus effect: a surface-tension effect which allows raindrops to roll freely on a lotus leaf as if they were drops of mercury. One of the key factors that determine how a fluid system behave is the size-scale. Fluids flow at small scales very differently than they do at large scales. The standard comparing to which small and large are defined is the capillary length. A number of surface-tension related phenomena are unfamiliar because they are only noticeable at length-scales of a few millimeters or below, and they look nothing like what we would expect fluids to behave when dominated by gravity. As fascinating as many of them may seem at first glance, surface-tension phenomena are actually not that far away from our daily lives.

Surface tension is everywhere because it costs energy to create areas of surfaces and interfaces, just like it costs energy to deform a solid (resulting in elasticity) or to elevate a weight (resulting in gravity). To minimize energy, a surface or an interface has the tendency to contract, and this tendency generates surface tension. The size of a system significantly affects the relative strengths of surface-tension effects comparing to effects of body forces, most commonly gravity. By equating the estimated magnitudes of surface tension and gravitational forces of a system, a length scale, know as the capillary length, can be defined. The capillary length of water on earth is about 2.7 mm. At the length scale of everyday objects, which is usually above the capillary length, surface-tension effects are not always prominent, because at those scales the competing force, gravity, is often much stronger. That is why the surface of a glass of water is more or less flat. However, as the size-scale decreases, surface tension decreases a lot slower than gravity, so when the size of a fluid system gets down to below the capillary length, surface tension takes over.

One of the defining characteristics of this moment in human history, is the tremendous efforts we are putting into the research and engineering of micro- and nano-scale materials and structures − systems where surface tension is often the predominant force. It is important to study surface-tension effects so that we can use them to our advantage. In this Ph.D. dissertation, we have investigated some important surface-tension phenomena including capillarity, wetting, and wicking. We mainly focus on the geometric aspects of these problems, and to learn about how structures affect properties. Understanding these phenomena can help develop fabrication methods (**Chapter 2**), study surface properties (**Chapter 3**), and design useful devices (**Chapter 4**) at scales below the capillary length.

In the first project (**Chapter 2**), we used numerical simulations and experiments to study the meniscus of a fluid confined in capillaries with complicated cross-sectional geometries. In the simulations, we computed the three-dimensional shapes of the menisci formed in polygonal and star-shaped capillaries with sharp or rounded corners. Height variations across the menisci were used to quantify the effect of surface tension. Analytical solutions were derived for all the cases where the cross-sectional geometry was a regular polygon or a regular star-shape. Power indices that characterize the effects of corner rounding were extracted from simulation results. These findings can serve as guide for fabrications of

unconventional three-dimensional structures in Capillary Force Lithography experiments [J. Feng (2011) (a)]. Experimental demonstrations of the working principle was also performed. Although quantitative matching between simulation and experimental results was not achieved due to the limitation of material properties, clear qualitative trends were observed and interesting three-dimensional nano-structures were produced.

A second project (**Chapter 3**) focused on developing techniques to produce three-dimensional hierarchically structured superhydrophobic surfaces with high aspect ratios. We experimented with two different high-throughput electron-beam-lithography processes featuring single and dual electron-beam exposures. After a surface modification procedure with a hydrophobic silane, the structured surfaces exhibited two distinct superhydrophobic behaviors − high and low adhesion. While both types of superhydrophobic surfaces exhibited very high (approximately 160°) water advancing contact angles, the water receding contact angles on these two different types of surfaces differed by about $50^\circ \sim 60^\circ$, with the low-adhesion surfaces at about $120^\circ \sim 130^\circ$ and the high-adhesion surfaces at about $70^\circ \sim 80^\circ$. Characterizations of both the microscopic structures and macroscopic wetting properties of these product surfaces allowed us to pinpoint the structural features responsible for specific wetting properties. It is found that the advancing contact angle was mainly determined by the primary structures while the receding contact angle is largely affected by the side-wall slope of the secondary features. This study established a platform for further exploration of the structure aspects of surface wettability [J. Feng (2011) (b)].

In the third and final project (**Chapter 4**), we demonstrated a new type of microfluidic channel that enable asymmetric wicking of wetting fluids based on structure-induced direction-dependent surface-tension effect. By decorating the side-walls of open microfluidic channels with tilted fins, we were able to experimentally demonstrate preferential wicking behaviors of various IPA-water mixtures with a range of contact angles in these channels. A simplified 2D model was established to explain the wicking asymmetry, and a complete 3D model was developed to provide more accurate quantitative predictions. The design principles developed in this study provide an additional scheme for controlling the spreading of fluids [J. Feng (2012)].

The research presented in this dissertation spreads out across a wide range of physical phenomena (wicking, wetting, and capillarity), and involves a number of computational and experimental techniques, yet all of these projects are intrinsically united under a common theme: we want to better understand how simple fluids respond to small-scale complex surface structures as manifestations of surface-tension effects. We hope our findings can serve as building blocks for a larger scale endeavor of scientific research and engineering development. After all, the pursue of knowledge is most meaningful if the results improve the well-being of the society and the advancement of humanity.

TABLE OF CONTENTS

LIST OF TABLES

Table **Page**

LIST OF FIGURES

Figure **Page**

CHAPTER 1

INTRODUCTIONS TO SURFACE TENSION AND OTHER RELEVANT CONCEPTS

The main goal of this chapter is to introduce some general concepts in the field of my research. First, the relevance of this research to other fields in modern science and technology will be mentioned. A brief introduction to the related physics concepts and principles will follow. The content of this chapter is expected to help establish a theoretical foundation for the rest of this dissertation.

1.1 Surface-tension Effects and Modern Science and Technology

In recent decades, major efforts have been devoted to understanding and engineering micro- and nano-structured systems. These efforts have had significant impacts on numerous research fields in physics, chemistry, biology, electrical and computer engineering, material science and engineering, and mechanical engineering. One of the fundamental origins of the unique properties exhibited by micro- and nano-structured systems is the enormous surface area per unit volume of material. We can do a simple estimation: if an object is shrunk to 1/1,000,000,000 of its original size, its surface area is only reduced to 1/1,000,000, which means the surface-area-to-volume ratio has increased by a factor of 1,000. That is what happens when a millimeter-cube turns to a micrometer-cube. Many unique surface-related properties offered by these small-scale systems make them interesting in scientific research as well as practical applications in various fields. For example:

(a) Suspensions of metal (such as gold) or semiconductor (such as CdSe and CdS) nanoparticles exhibit a wide range of size-dependent colors, because nanoparticles of different diameters have different surface-plasmon resonance frequency and absorb light at different wavelengths [Said-Mohamed (2012), Y. W. Lin (2006)].

(b) Geckos can climb up very smooth vertical and even inverted walls thanks to the millions

of micron-scale adhesive seta on the bottom of their toes. Each seta splits into hundreds of sub-micron tips to maximize the contact area and generate tremendous adhesion force based on Van der Waals interactions [Autumn (2000)].

(c) Activated carbon is widely used in water filtration owing to the ability of its enormous internal surface to preferentially adsorb organic chemicals over water [Mattson (1969), Holden (1971)].

Amongst the numerous surface-related effects, we have chosen to focus on the surface-tension effects. As mankind's explorations into the micrometer- and nanometer-scale science and technology extend deeper and wider, surface-tension effects are gaining increasingly more attention not only because they are powerful and often can be the major factor that dictate the behavior of a system, but also because the way they are affected by the surface topography and uniformity. Surface tension exists anywhere there is a surface regardless of length-scale, but, on earth, only at small length-scales it becomes an important force as a result of the high surface area to volume ratios. In low gravity environments such as the outer space, surface tension is important at big scales as well. Surface tension is especially important for systems consist of one or more fluid components, often referred to as soft condensed matter, because fluids can be easily deformed under applied stresses and in turn reshape their surfaces and interfaces. The interplay between fluid flow and surface tension gives rise to a large variety of scientifically intriguing, functionally unique, and application-relevant properties, for example: (a) self-propel and uphill motion of drops of water [Bico (2002), Chaudhury (1992)], (b) formation and stabilization of multiple emulsions [W. Wang (2011)], (c) uni-axial and uni-directional spreading [Y. Chen (2005), K. H. Chu (2010)], (d) the lotus effect and droplet bouncing [Yarin (2006), Shieh (2010)], (e) capillary origami [Py (2007)], (f) curvature-driven migration and assembly [Cavallaro (2011)], (g) surface-tension powered spore dispersal of fungi [Dumais (2012)], (h) droplet motion controlled by vibrations [Brunet (2007)]. These only represent a corner of the iceberg of the spectacular world of surface tension effects in small-scale fluidics. By and large, surface-tension effects have substantial relevance to fabrication, assembly, characterization, and control of micro- and nano-systems.

Surface tensions come from the fact that surfaces and interfaces have the tendency to contract, but they do not always cause every surface and interface in a specific system to contract. For example, under the right conditions, surface tensions can bend the meniscus inside a capillary into a bowl-shape (more detail on this in the following sections). The sources of the richness of surface tension effects include surface topography, surface chemistry, surface response to fluid contact, and the addition of surfactants. In my research, I mainly targeted the structural aspect, and the specific question of interest is: how do simple fluids, where only surface tension is important, respond when put into contact with small-scale complex boundaries? Here a complex boundary often involves two tiers of structures: capillaries with various corners, micro-blocks with nano-pillars on top, or micro-channels decorated with fin-like structures on the walls. Knowledge related to this topic can potentially help us understand and mimic natural systems (**Chapter 3**), develop new fabrication techniques (**Chapter 2**), and engineer novel devices (**Chapter 4**). To systematically approach the problem regarding structured-induced surface-tension effects, these are the first steps: To begin with, a basic microscopic model of a surface and the origin of surface tension should be established. Then, in the context of a simple case where two surfaces meet at a line, the definition of contact angle and the Young's equation should be introduced. The various factors that can affect surfac tension and contact angle will also be discussed. Finally, the concept of Laplace pressure and the quantification by the Laplace equation based on the local curvature of the surface should be explained

1.2 Surface Tension: Physical Origins

Physically, a surface or an interface is a collection of a few layers of atoms, molecules, or ions that are located in the vicinity of a two-dimensional manifold across which there exists a large spatial gradient of the density of these particles. A schematic diagram of a surface is shown in **Figure 1.1**. As a result, the physical and chemical properties change drastically over distances comparable to the molecular separation scale. Conventionally, a surface often refers to the border separating a solid or a liquid and air, while an interface usually refers to the border separating a liquid and a solid, two immiscible liquids, or two solids in contact at the molecular level. Inside a surface, the constituent particles are closely spaced at a high

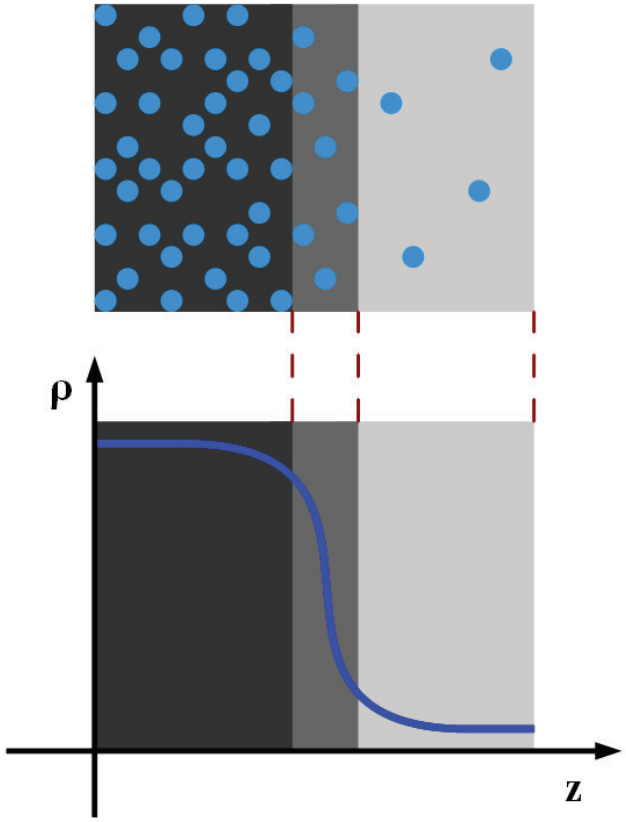

Figure 1.1. Schematics of distribution (top) and plot of volume density (bottom) of the constituent particles in the bulk (dark gray), in the surface layer (gray), and outside (light gray). Notice the large gradient in density at the interface. This plot only represents the general qualitative trend in arbitrary unit. The exact values on the plot depends on the specific surface or interface. The details of the shape of the plot also depend on the spacial resolution. When the resolution is high, often times there will be fluctuations and peaking in the density distribution near the interface.

density (they may or may not be mobile depending on whether they are in the liquid or solid state), while outside the surface, the density of these particles is very low (gas or vapor) or sometimes can even be effectively zero (vacuum). In the case of an interface, similar density changes apply to each type of liquid or solid molecules. Based on the definition, a surface or an interface is always microscopic and discrete on its normal direction, typically a few nanometers thick. On its tangential direction, a surface or an interface can be microscopic and discrete (e.g., surface of iron oxide nanoparticles [Desautels (2012)]), microscopic and continuous (e.g., surface of an oil micro-drop in a microfluidic channel), or macroscopic (e.g., surface of water in a pond). In this dissertation, we only consider surfaces and interfaces in the continuum limit, either microscopic or macroscopic. This is because surface tension is mostly defined in the continuum limit [de Gennes (2003)]. A stable surface or interface is rarely a static entity, rather, the constituent particles are under constant diffusion departing and re-entering the bulk at a well-defined dynamic equilibrium, so temperature often plays an important role in determining the properties [Lautrup (2009)].

A surface or interface can exist between two different materials or between two different phases of the same material. Whenever there is a surface, there is a surface tension associated with it. Surface tension originates from the imbalance of the physical and chemical environments on either side of a surface or an interface felt by the interfacial molecules, atoms, or ions. In the simplest model, as shown in **Figure 1.2 (a)**, a molecule inside the bulk of a solid or a liquid experiences more attractive interactions from the neighboring molecules than a molecule at the surface does, simply because it is surrounded by more molecules of the same kind. That is to say that, a molecule has to be at a higher energy state, for losing a portion of the (negative) binding energy between itself and its neighbors, when it becomes a surface molecule, so naturally, a system wants to minimize the number of surface molecules as much as possible, which effectively is also minimizing the surface area. Moreover, the surface molecules only have interacting neighbors on one side, the net force on these molecules points towards the bulk of the liquid, and therefore the reduction of surface area is not only energetically favorable but also dynamically accessible. Surface tension, γ, represents the amount of energy (in this case the Helmholtz free energy, F) it would take to generate a unit area of a specific surface or interface, under constant temperature, T,

volume, V, and number of molecules, n:

$$\gamma = \left[\frac{\partial F}{\partial A}\right]_{T,V,n}. \tag{1.1}$$

Surface tension is measured in unit of energy per area or, equivalently, force per length. This equivalence is based on the concept that force, f, is the negative spacial gradient of energy, E:

$$\vec{f} = -\vec{\nabla} E. \tag{1.2}$$

Physically, this means on per unit length of surface boundary, or contact line, there is a force with magnitude γ and direction perpendicular to the local segment of that contact line towards the inside of the surface, as schematically shown in **Figure 1.2 (b)**. For homogeneous materials in the continuum limit, surface tension is independent of the surface area or the contact line length, but is specific to the material pair (i.e., the chemical composition and phase of either side of the surface or interface), and therefore it is generally considered a material property. At equilibrium and under saturated partial pressure, surface or interfacial tension is usually a function of temperature, and sometimes can be altered by exposure to light [Demirel (2011)] or specific chemicals [de Gennes (1998)], or by an applied electric field [Bateni (2005), Mugele (2005)]. For a surface, of either a liquid (e.g., water-air) or a solid (e.g., silica-air), a positive amount of energy is required to create additional surface area because of the absence of attractive interactions on the outside. For an interface between two different liquids (e.g., water-oil), if the liquids are immiscible, then it is energetically more favorable (the gain from enthalpy outweighs the penalty from entropy) for the same liquid molecules to be in close proximity, and therefore the surface tension must be positive. For an interfaces between a solid and a liquid, if the solid can be dissolve in the liquid, then the surface tension can be negative, otherwise it should be positive. In modern scientific and technological applications, there are more complicated scenarios. For rubber-like materials, or cross-link polymer networks, it is possible to find liquids which can swell a network up to a certain degree. This indicates that mixing of the two materials (liquid and polymer) on the molecular level is energetically favorable but the chemical bonds in the cross-linked network prevents it from deforming infinitely. In this

Table 1.1. Surface tension of various liquids, mixtures, and polymers. The listed values for silicone oil and the polymers are meant to only represent approximate ranges. The exact surface tension values for those materials depend on the molecular weight and degree of branching, and vary case-by-case.

Water	Water	Ethanol	IPA	Mercury	Silicone oil
25 °C	50 °C	20 °C	20 °C	20 °C	20 °C
72 mN/m	59 mN/m	23 mN/m	22 mN/m	486 mN/m	20 ∼ 21 mN/m
20% ethanol + 80% Water	50% ethanol + 50% Water	80% ethanol + 20% Water	Cross-linked PDMS	Teflon	Polystyrene
25 °C	25 °C	25 °C	25 °C	25 °C	25 °C
30 mN/m	26 mN/m	23 mN/m	20 ∼ 23 mN/m	20 mN/m	33 ∼ 40 mN/m

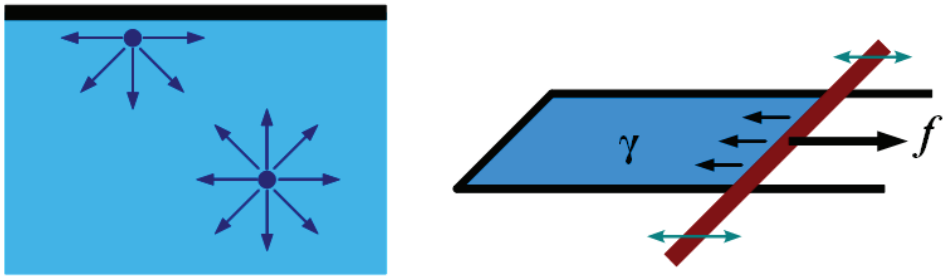

(a) (b)

Figure 1.2. Schematics of the origin and a representative effect of surface tension. (a) A surface molecule experiences attractive interactions only on one side (towards the bulk). The origin of surface tension is the imbalance of interactions on either side of a surface. (b) As a manifestation of surface tension, a surface pulls on the boundary (red bar) in attempt to reduce its area.

case, it would seem like the network-liquid interfacial tension is initially negative, for that the interface spontaneously expand, then it turns zero (or negative) as the swelling stops. In the cases where there are surfactants, surface and interfacial tension can be drastically reduced. This principle is often used in stabilizing emulsions. Experimentally, surface tension of a liquid can be determined with the Wilhelmy-plate method [Holmberg (2002)] or the pendant-drop method [Hauser (1948), Roe (1967)], interfacial tension between liquids can also be measured with spinning drop method [Vonnegut (1942), Princen (1967)]. For solid surfaces, measurements of surface tension are not as straightforward [Shuttleworth (1950), Sullivan (1981)]. The surface tensions of some common solids and liquids (in contact with air) are listed in **Table 1.1** [Owens (1969), Vazquez (1995), de Gennes (1998)].

The total amount of surface energy of a system grows proportionally to the total area of surfaces and interfaces, which is typically the characteristic length to the second power. Gravitational energy, on the other hand, scales with the volume, or the characteristic length to the third power. Due to this difference in scaling factor, there exists a cross-over at which point surface energy of a system is on the same order of magnitude as gravitational energy. This cross-over point, known as the capillary length, κ^{-1}, can be estimated by comparing the surface force and gravity:

$$\kappa^{-1} = \sqrt{\frac{\gamma}{\rho g}}, \tag{1.3}$$

where ρ is the volumetric mass density and g is the acceleration due to gravity. On earth, g = 9.8 m/s^2; at 20 °C and 1 atm, the surface tension and the density of water are 72.8 mN/m and 998 kg/m^3, respectively. The resulted capillary length of water under these conditions is about 2.7 mm. In the case of mercury, although it has a very high surface tension (486 mN/m), it also has a very high density (13.5 $\times$ 10^3 kg/m^3), and its capillary length is found to be lower than that of water, at about 1.9 mm. Other common liquids generally have lower surface tensions (in the 20 $\sim$ 70 mN/m range) and similar density (in the 500 $\sim$ 1500 kg/m^3 range) comparing to water, and their capillary lengths are usually around 1 $\sim$ 3 mm under normal terrestrial conditions. Fluids aboard space shuttles exhibit much larger capillary lengths. This demands special fuel-container design from engineers and drinking techniques from astronauts [Finn (1986)]. It is worth mentioning that the capillary length does not correspond to a sharp transition, but rather it provides a rough estimation of the range at which the influences of surface tension can reach. The capillary length signifies the transition between gravity-dominated regime and surface-tension-dominated regime. In other words, capillary length provides a standard length-scale for describing whether a system is large scale or small scale in the context of surface-tension effects.

1.3 Surface Tension: Contact Angle

Gently put a small drop of water on a wooden table top, and one will notice the drop stays in a (more or less) spherical-cap shape, because surface tension is holding the droplet together. Now do the same test but with ethanol. This time the droplet spread out much

farther − almost completely stretching itself into a flat disc. If the droplets are small enough, gravity is negligible comparing to surface tension, so whether or not and how much a fluid spreads on a surface depends on the balance of the surface and interfacial tensions of the system. To rule out gravity effects, the same experiments can be done on a downward-facing wooden surface, and the observations should stay almost unchanged. Since the surface tension of water is a few times higher than that of ethanol, it would seem as though, perhaps somewhat counter-intuitively, surface tension makes a surface curved instead of flattening it. However, if the constraint of volume conservation is also taken into consideration, then it would make sense that surface tension prefers to shape a surface as close to spherical as it can.

Let's consider a process where a drop of liquid (with surface tension γ_{LV}) is deposited on a solid surface (with surface tension γ_{SV}), and the interfacial tension between the liquid and the solid is γ_{SL}. It turns out there are three possible scenarios:

(a) Total wetting. This happens when γ_{SV} is greater than or equal to the sum of γ_{LV} and γ_{SL}. In this case, the liquid will spread completely on the solid surface because the system can get to lower energy state by replacing the solid-air interface with the same area of a liquid-air interface and a solid-liquid interface.

(b) Partial wetting. This happens when γ_{SV} is less than the sum of γ_{LV} and γ_{SL}, and the energy barrier (excitation energy) for the solid-liquid interface to expand can be overcome by thermal fluctuations or the effects of hydrostatic and/or hydrodynamic pressures. In this case, the liquid will spread to a certain degree and form a spherical-cap (for small droplets) or a compressed cap (for big droplets).

(c) Non-wetting. This happens when γ_{SV} is less than the sum of γ_{LV} and γ_{SL}, and the energy barrier (excitation energy) for the solid-liquid interface to expand can not be overcome by thermal fluctuations or the effects of hydrostatic and hydrodynamic pressures. In this case, the system will be dynamically trapped at a metastable state and liquid will not spread at all on the surface (but may flatten due to gravity), and may bounce off the surface if a small normal velocity is applied right before impact.

These scenarios may also occur between two immiscible liquids. For example, a drop of

silicone oil spreads completely on the surface of water and form a very thin surface film (total wetting).

In the case of partial wetting, a quantity known as the contact angle is often used to described in more detail the wettability of a solid surface by a certain liquid. The contact angle is a material property, and it is defined as the local angle at the contact line between the liquid-vapor interface and the solid-liquid interface, as shown in **Figure 1.3**. A low contact angle mean high wettability and a high contact angle means poor wettability. The definition of contact angle can also be extended to the case where, instead of air, there is an other liquid. Contact angle can be calculated by Young's equation:

$$\gamma_{LV} \cos\theta = \gamma_{SV} - \gamma_{SL}. \tag{1.4}$$

The cosine of an angle is always range between 1.0 and -1.0. At the limit where $\cos\theta = 1$, the system approaches total wetting. At the limit where $\cos\theta = -1$, the system approaches completely non-wetting. It has been proposed that the interfacial tension between a solid and a liquid can be calculated by:

$$\gamma_{SL} = \gamma_{SV} + \gamma_{LV} - W_{SL}, \tag{1.5}$$

where W_{SL} is the work of adhesion per area between the solid and the liquid. This equation is based on the reasoning that creating a solid-liquid interface is effectively the same as first separately creating a solid surface and a liquid surface and then bringing them together into intimate contact. Questions still remains on whether the work of adhesion can be exactly zero. Nonetheless, it has been shown experimentally that some special surfaces have water contact angles that are effectively 180° [L. Gao (2006) (a)]. Derivation of Young's equation can be obtained either by force balance (i.e., trigonometry) at an infinitesimal section of the contact line (**Figure 1.3**), or by minimization of energy under the constraint of volume conservation (i.e., Laplace multiplier method), and these two methods are equivalent. For practical applications, contact angle can be considered a geometric constraint which requires that, at equilibrium, two surfaces meet at a certain angle. From the energy point of view,

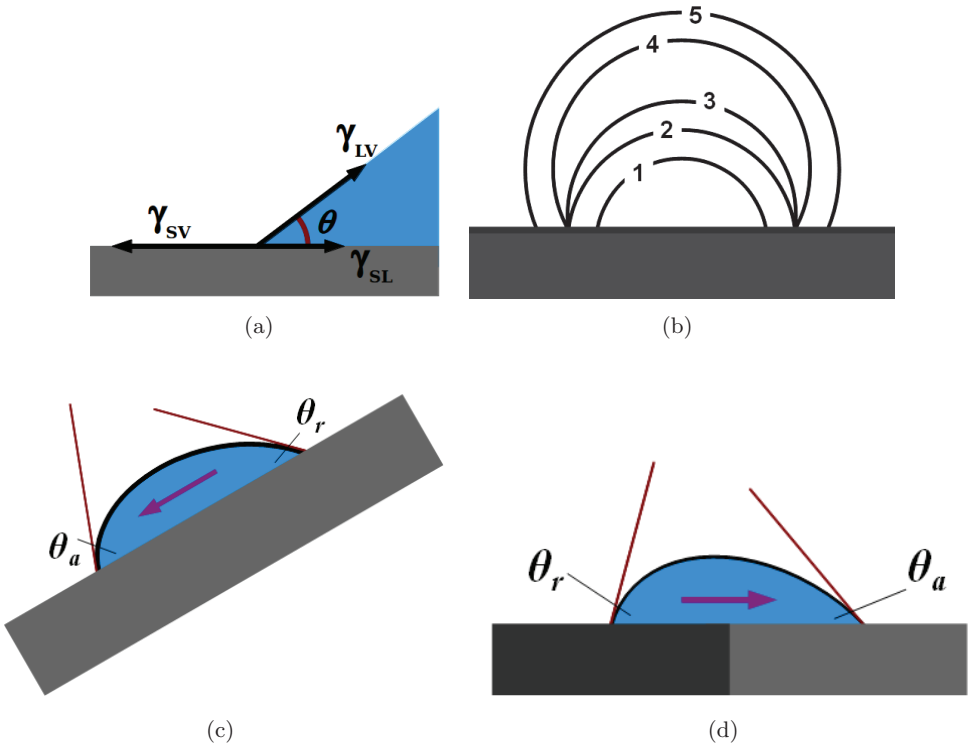

Figure 1.3. Schematics of: (a) Contact angle, θ, can be calculated based on force balance along the solid surface at the contact line. (b) Receding contact angle (1 and 2), equilibrium contact angle (3), and advancing contact angle (4 and 5) can all be reached by cyclically changing the volume of fluid [Gao (2006) (b)]. (c) The effect of contact angle hysteresis on droplet motion. (d) On an inhomogeneous surface, the advancing contact angle of a drop can be lower than the receding contact angle, causing the drop to move spontaneously.

contact angle can be thought of as the result of a system finding a configuration which represents one of its energy local minima. This local minimum is not always the global minimum, that is to say that the system can be dynamically trapped at a configuration from which thermal excitation alone is not powerful enough to get it out. This is one of the mechanisms that can cause the pinning of a contact line. This mechanisms is one of the most important cornerstones of **Chapter 3** and **Chapter 4**.

Experiential measurements of contact angle can be performed with a sessile-drop goniometer straightforwardly based on definition. It is nonetheless critical to make sure the droplet profile is correctly extracted with proper lighting conditions and the sampling point of the liquid-air interface is as close to the contact line as possible. Since surface tension

is affected by physical and chemical conditions including temperature and chemical composition, so is contact angle. On one hand, this provides a means for tuning the contact angle or wettability by mixing two liquids together and varying the mixing ratio. On the other hand, this suggests that processes (such as evaporation and absorption) that can alter the relative concentration or surface conditions can play a significant role in affecting the contact angle. Further more, most of the time in practice the complication and difficulty in determining the contact angle comes from unevenness of the surface, including surface roughness, chemical inhomogeneity, contamination and sediments on the surface, etc. Unless a carefully cleaned atomically smooth solid surface is used, experimentally measuring the contact angle of a certain liquid-solid pair often result in a range which contains the value of equilibrium contact angle (can be found by applying **Equation 1.4**) [de Gennes (2003)]. As shown in **Figure 1.3 (b)**, the contact angles above which is required for the contact line to advance is known as the advancing contact angle (θ_{adv}); the contact angles below which is required for the contact line to recede is known as the receding contact angle (θ_{rec}). On many surfaces the advancing and receding contact angles represent the contact angle at the advancing and receding front (at the moment right before the contact line moves), and they correspond to the upper and lower limits of contact angle, respectively. In those cases, the difference between the two limits (θ_{adv} and θ_{rec}), known as the contact angle hysteresis ($\Delta\theta$), corresponds to the angle at which the solid surface needs to be tilted in order for a droplet of the liquid to roll down from it (schematics shown in **Figure 1.3 (c)**). The exact causes of $\Delta\theta$ is not yet fully understood, but one model suggests that contact-line pinning is largely responsible [Gao (2006) (b)]. More detailed discussions on this topic will be provided in **Chapter 3**. There are, nonetheless, quite a few special cases where the definitions of θ_{adv} and θ_{rec}, or even contact angle in general, are ambiguous. For example, a surface, a tube, or a micro-channel with gradually changing properties due to a density gradient of coating chemicals. In these cases, it is possible to achieve θ_{adv} lower than θ_{rec}, and the droplet move spontaneously (schematics shown in **Figure 1.3 (d)**). It is important to recognize that here the θ_{adv} and θ_{rec} are defined based on the point of view of the droplet, not with respect to a specific location on the surface. Similarly, if a plug of fluid A is situated in between two different fluids B and C, assuming fluid A is immiscible in both

B and C, it is possible to find material combination such that fluid A can spontaneously move towards one side due to a lower θ_{adv} and a higher θ_{rec} (they are, again, defined based on the droplet's viewpoint). Also, sometimes a droplet or a plug of fluid can spontaneously move due to the effects of Laplace pressure, even though θ_{adv} and θ_{rec} are the same. For example, when it is placed inside a slightly conical tube (schematics shown in **Figure 1.4 (e)**, more explanations will be included in the following section). In all these cases (where motion spontaneously start on a droplet or a plug of fluid), kinetic energy is converted from potential energy stored in the surfaces and interfaces (equivalently, the potential energy can be regarded as been stored in the configuration or relative location between the solid and liquids). The same reasoning is also applicable to some of the previously mentioned examples including: drop running uphill, uni-directional spreading, curvature-driven migration, and surface-tension powered spore dispersal.

1.4 Surface Tension: the Laplace Pressure

Contact-line motions, characterized by advancing and receding contact angles, is one aspect of the correlations between configuration and dynamics. Besides that, there is another important aspect of these correlations − the Laplace pressure. While contact angle embodies the local kinetics at the contact line, Laplace pressure represents the collective effect of surface tension on a curved surface or interface. For this reason, in many practical applications (such as in the pendant-drop method and the spinning-drop method) Laplace pressure is directly related to the measurements of surface tension. Existence of Laplace pressure is independent of contact line. For example, the inside of a freely falling raindrop experiences Laplace pressure which makes its internal pressure higher than the atmospheric pressure outside. Nonetheless, in cases where there are contacts, Laplace pressure and contact angle are intimately linked to each other in many aspects, including: (a) contact angle (sometimes in conjunction with volume conservation) often serves as a geometric boundary condition which determines whether and how much liquid surfaces are curved, and thus how much Laplace pressure should present. (b) surface tension and Laplace pressure share the same origins − surface energy and volume conservation, yet they each is useful for describing a different aspect of the physics.

A flat plane can not enclose a finite, none-zero volume. In fact, at least four flat planes are required to enclose a finite volume (in a tetrahedron configuration) in the Eulerian space. If the number of surfaces is less than four, volume conservation requires at least one surface to be curved, and that give rise to Laplace pressure. Laplace pressure is the pressure difference between the inside and the outside of a curved surface or interface. At each point on a surface or an interface, the Laplace pressure is proportional to the surface tension as well as the local mean curvature. Calculation of Laplace pressure is based on the Young-Laplace equation:

$$\Delta P = 2\gamma H = \gamma\left(\frac{1}{R_1} + \frac{1}{R_2}\right), \tag{1.6}$$

where γ is the surface tension (or previously denoted as γ_{LV}), H is the mean curvature, R_1 and R_2 are the two principle curvatures. It should be mentioned that the sign of the mean curvature depends on the definition of the inside and outside of the surface or interface, and so does the Laplace pressure. In any case, for a surface or an interface with positive surface tension, the Laplace pressure always adds on to the side with a convex boundary. This is due to the fact that if a local portion of a surface move inwards respect to the side that sees it as a convex boundary, its area is reduced thus it lowers its energy due to surface tension. As shown in **Figure 1.4 (a)**, if R reduces by a mount of ΔR, then the corresponding arc length reduces fro dl_1 to dl_2, and when extended to a two-dimensional surface, that corresponds to a reduction in area. Force is the negative gradient of energy, and pressure is the area density of force. This is also how the Young-Laplace equation (**Equation 1.6**) can be mathematically derived (at the limit of $\Delta R/R \to 0$). Based on this model, a simple way to think of Laplace pressure is that it is an additional pressure (or pressure difference) locally induced by surface curvatures because curvatures cause areas to change when translated radially.

Laplace pressure is related to many phenomena, and capillary rise is perhaps the most familiar one amongst them. As shown in **Figure 1.4 (b)**, in a capillary with hydrophilic inner surface, a column of water can be pulled up above the water level outside. There are two explanations for this phenomenon which are equivalent: pressure balance and energy minimization. The equivalency is established by the Young's equation (**Equation 1.4**).

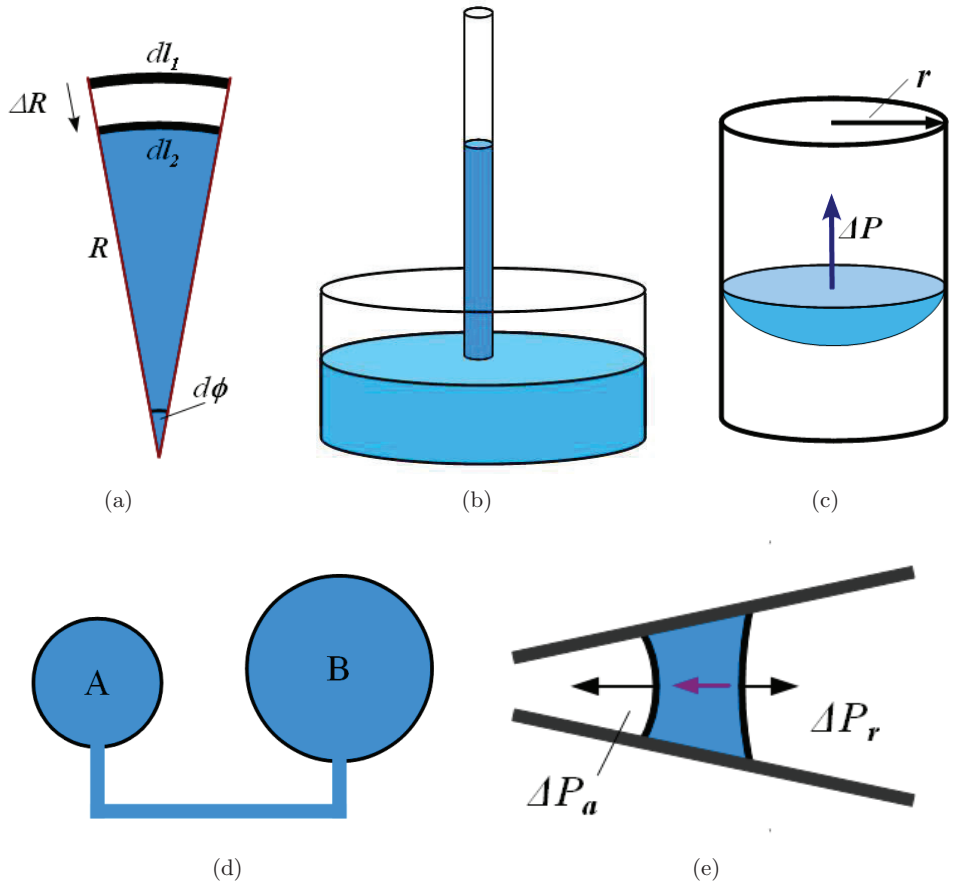

Figure 1.4. Schematics of several aspects of the Laplace pressure. (a) Schematics for deriving the Young-Laplace equation. (b) Capillary rise as a manifestation of the Laplace pressure. (c) Schematics for estimating the Laplace pressure generated by a curved meniscus formed in a capillary. (d) A smaller volume, A, and a bigger volume, B, of the same fluids are connected together. They can represent either two air balloons or two soap bubbles. (e) Laplace pressure is larger on the advancing meniscus than on the receding meniscus, causing the plug of wetting fluid to move spontaneously towards the thinner end of the slightly conical tube.

The pressure balance approach states that the concave meniscus adds a negative pressure to the infinitesimal volume of fluid right underneath it, so that volume must rise to a height where it can have enough hydrostatic pressure to balance the Laplace pressure, and the height, h, is found to be:

$$h = \frac{2\gamma \cos\theta}{\rho g r}, \tag{1.7}$$

where r is the inner radius of the capillary. The energy minimization approach shows that the same height h corresponds to a stable equilibrium state. In the mathematical equation for calculating the Laplace pressure, there is a noticeable lack of information about surface orientation. This indicates a symmetry: as shown in **Figure 1.4 (c)**, a fluid which occupies the upper portion experience the exact same Laplace pressure as a fluid which occupies the lower portion as long as their free surfaces are formed in the same shape (although to satisfy this requirement their contact properties to the inner wall of the capillary must be very different). In other words, as much as a wetting fluid (with θ ¡ 90°) will be sucked into the capillary, a non-wetting fluid (with θ ¿ 90°) will be rejected by the capillary. This is one of the bases of the working mechanism behind superhydrophobic surfaces (hydrophobic surfaces with micro-textures). It can be estimated, if a fluid comes from the top and form a convex meniscus, it will be supported by an upward-pointing Laplace pressure which is a function of the contact angle, θ, and the radius of the capillary, r:

$$\Delta P = \frac{2\gamma \cos\theta}{r}. \tag{1.8}$$

Consider some realistic values, say $\theta = 120°$, then:
(1) When $r = 5$ μm, $\Delta P = 14.6$ kPa, which is about equal to (a) the hydrostatic pressure generated by a 1.5-meter-tall water column, or (b) the hydrodynamic pressure generated by a water flow running at 5.4 m/s. (2) When $r = 100$ nm, $\Delta P = 730$ kPa, which is about equal to (a) the hydrostatic pressure generated by a 74-meter-tall water column, or (b) the hydrodynamic pressure generated by a water flow running at 38 m/s. For reference, the terminal speed of raindrops is in the range of $9 \sim 13$ m/s [Beard (1976)]. More details on the significant ramifications of these values in the context of hierarchical structures will be discussed in **Chapter 3**.

An important characteristics of Laplace pressure is that the larger the curvature (i.e., the smaller the radius of curvature) the larger the pressure. This indicates instability. To explain this, two interconnected bodies of fluids are shown in **Figure 1.4 (d)**. First, imagine A and B are two initially identical balloons but are inflated to different levels. Intuition says if they are connected, they should eventually stabilize at the same final size (assuming some mechanism of energy dissipation such as heat), because the bigger the balloon, the more it's skin is stretched, and the larger elastic tension are present. Now, if instead A and B are two soap bubbles, the result would be completely opposite. The bigger bubble would expand and the smaller bubble would shrink, because the bigger bubble always has a larger radius of curvature than the smaller bubble, the pressure inside the bigger bubble is always lower, and the pressure difference increases as time goes by. Eventually the smaller bubble empty itself into the bigger one. This curvature dependency of Laplace pressure causes the larger crystals in a solution to grow at the expenses of the smaller crystals disappearing, a phenomenon known as the Ostwald ripening. On the energy viewpoint, to enclose a same total volume, one large sphere is more area-efficient (takes less total surface area), and thus more energy-efficient, than two small spheres. In another scenario, as shown in **Figure 1.4 (e)**, under the same force law, a plug of wetting fluid (with $\theta < 90°$) will spontaneously move towards the thinner end of a slightly conical tube. This can be explained by (a) $\Delta P_a > \Delta P_b$ (vector comparison, assume left is the positive direction) and thus the net force acting on the body of fluid is pointing to the thinner end, or (b) with the same volume, the fluid can increase its contact area with the tube (as it stretches longer in the axial direction) by moving towards the thinner end and by doing so lower the energy of the system. If the fluid is non-wetting (with $\theta > 90°$), the analysis is more complicated and will not be discussed here. In all, the important implication of this example is that a feasible approach for using asymmetric structures to induce asymmetric behaviors is via the mechanics controlled by Laplace pressure. This concept inspires the work of **Chapter 4**.

1.5 Pressure Driven, Low Reynolds Number Flow

This section is included as an attempt to provide a brief introduction to fluid dynamics. Fluid dynamics is a very large field of study and only a very small portion of it which is directly related to the projects in this dissertation can be covered here.

By definition, a fluid is a substance that deforms continuously under an applied shear stress. In other words, a fluid is not defined based on its internal microscopic structure, but rather on its external macroscopic behavior under externally applied shear stresses. The simplest model often applied to think about the behavior of a fluid is a one-dimensional flow between two infinite parallel plates. The bottom plate is fixed and a force is applied tangentially to the top plate. A shear stress can be exerted onto the fluid as it moves along with the top plate. The larger this stress, the faster the fluid deforms. For the purpose of assisting the research of fluid behaviors, within the science and engineering community, fluids are often divided into two categories − Newtonian and non-Newtonian. In a Newtonian fluid, shear rate is linearly proportional to the shear stress, the proportionality constant is known as the viscosity. Any deviation on this relation between shear rate and shear stress would make a fluid non-Newtonian. Typical non-Newtonian responses can be captured by the viscosity being complex (also known as viscoelasticity), frequency or rate dependent (relaxation, shear-thinning, shear-thickening), and strain dependent.

At micro- and nano-scales, surface and interfacial tensions, due to their large strength, can be dominating factors in determining fluid behaviors, especially for those fluids that (above a certain time scale) do not sustain shear stresses in the bulk (although, for the completeness of discussion, it is conceivable that for a droplet of fluid, such as one which is confined in between two parallel plates and with both contact line completely pinned, its surface area can be increased by shear strain, so surface energy can provide some resistance to shear). When a fluid is continuously deformed under shear, a flow field will develop. One of the most important characteristics of a flow field is its flow pattern C laminar, turbulent, or the transition between them. In a laminar flow, fluid flows in parallel layers with no disruption between the layers, the flow field adopts a regular pattern which is analytically solvable. In a transitional flow, stationary eddies are developed in the flow. In a turbulent flow, transient vertices, eddies, and wakes are constantly formed and dissipated, the flow

field is highly chaotic and unpredictable. The parameter which characterizes the nature of a flow field is the Reynolds number, Re, which provides an estimation of the relative strengths of inertial effects compared to viscous effects:

$$Re \equiv \frac{\rho v L}{\eta}, \tag{1.9}$$

where ρ is the fluid density, v is the flow velocity, L is the characteristic length-scale, and η is the viscosity. A small Reynolds number corresponds to a laminar flow. This occurs when the fluid has high viscosity, or when the flow field has a low velocity and/or a small dimension. The expression of the Reynolds number (**Equation 1.9**) indicates, in some sense, decreasing the characteristic length-scale is effectively equivalent to increasing the viscosity of the fluid.

In any continuous flow, the fluid motion can be fully described by the Navier-Stokes equations. The derivation of Navier-Stokes equations is based on conservation of mass and conservation of momentum. In laminar flows, the exact solutions for Navier-Stokes equations can be obtained. For incompressible (under conservation of volume) Newtonian (viscosity is independent of stress or strain) fluids, the momentum equations of the Navier-Stokes equations are written as:

$$\rho\left(\frac{\partial \vec{v}}{\partial t} + \vec{v} \cdot \vec{\nabla}\vec{v}\right) = -\vec{\nabla}p + \eta\nabla^2\vec{v} + \vec{f}, \tag{1.10}$$

where p is the dynamic pressure, and f represents the sum of all the body forces. For small scale fluid systems with non-vanishing viscosity values, inertial effects are generally minimal, and the resulting fluid flows are laminar. For fluid flows with low Reynolds numbers and negligible gravity, the only important physical quantities are the dynamic pressure and the viscous stress, so **Equation 1.10** can be reduced to:

$$\vec{\nabla}p = \eta\nabla^2\vec{v}, \tag{1.11}$$

In **Equation 1.11**, the left-hand-side can be viewed as the driving force, and the right-hand-side can be interpreted as the resistance originated from the viscous nature of the fluid.

When a small-scale flow field, such as one which is inside a capillary or a micro-channel, is powered by a constant applied pressure drop, the flow velocity decreases drastically as the diameter of the tube or the channel decreases (here we approximate tubes and channels of any cross-sectional geometry as a cylindrically symmetric tube for an order-of-magnitude estimation). This is known as the Poiseuille flow, and its velocity field can be solved as:

$$v(r) = \frac{P}{4\eta L}\left(R^2 - r^2\right), \tag{1.12}$$

Based on this solution, the peak velocity $v(r = 0)$, scales with the diameter, R, to the second order. The volumetric flow rate can be found to scale with to R the fourth order. That is to say, in order to push a certain amount of fluid through a tube within a certain amount of time, one needs to push a lot harder as the tube gets thinner. This is why pumping fluid through microfluidic devices with externally applied pressure is rather inefficient. An alternative way of driving fluids through small tubes or channels is using the Laplace pressure (**Chapter 2**) or by wicking (**Chapter 4**). Solution for the velocity field of a uni-directional flow driven by Laplace pressure can be obtained by combining **Equation 1.8** and **Equation 1.12**:

$$v(r, x) = \frac{\gamma \cos\theta}{2R\eta x}\left(R^2 - r^2\right), \tag{1.13}$$

This expression shows that the dependence of velocity on tube diameter is weaker because as the tube gets thinner, the Laplace pressure gets larger. The filling rate and length of filling as a function of time can also be calculated as:

$$\frac{dx}{dt} = \frac{1}{2}\sqrt{\frac{\gamma R \cos\theta}{2\eta t}}, \tag{1.14}$$

and

$$x = \sqrt{\frac{\gamma R t \cos\theta}{2\eta}}. \tag{1.15}$$

The time it takes to fill up to a 1:1 aspect ratio (based on diameter) is:

$$t_1 \equiv t(x = 2R) = \frac{8\eta R}{\gamma \cos\theta}. \tag{1.16}$$

Equations 1.16 indicates that it actually takes less time, in a Capillary Force Lithography (CFL) procedure (more details in **Chapter 2**), to achieve a 1:1 aspect-ratio structure as the capillaries get smaller. This gives CFL a considerable advantage in terms of efficiency.

CHAPTER 2

THE EFFECTS OF CORNERS IN CAPILLARY FORCE LITHOGRAPHY

High aspect ratio three-dimensional nano-structures are of tremendous interest to a wide range of fields such as photonics, plasmonics, fluid mechanics, and biology. As the limit of imprint lithography is pushed to smaller length scales, a great deal of research effort has focused on utilizing capillary forces to the advantage of lithography techniques. Recent developments in Capillary Force Lithography (CFL) have focused on taking advantage of the formation of menisci to implement additional features and enhance the functionality of small size-scale structures. In this project, we extended this exploration of surface-tension effects to a variety of capillary geometries. Systematic studies on the three-dimensional shapes of equilibrium menisci formed in capillaries with polygonal and star-shaped cross-sections were performed based on Surface Evolver simulations. Experimental attempts have also been made to verify the simulation results. The uniqueness of this project is that surface-tension effects at corners are heavily utilized, which leads to formation of novel three-dimensional structures with promising application potentials.

2.1 Introductions to Capillary Force Lithography

Due to their extremely small feature sizes, micro- and nano-structures are generally very difficult to construct by traditional manufacturing techniques and systems. New technologies are in demand for micro- and nano-fabrications. There are in general two basic schemes for micro- and nano-fabrications: the top-down and the bottom-up approaches. The top-down methods, which mainly include a number of lithographic techniques, such as photolithography, electron-beam lithography (EBL), and dip-pen lithography (DPL), generally provide outstanding control, flexibility, and versatility, but require highly advanced fabrication tools (e.g., a mask-aligner, an SEM, or an AFM) and special operation skills. On

the other hand, bottom-up methods such as self-assembly, deposition, and etching, are much more economic, efficient, and robust, but only allow very limited set of structural variations. It has been shown that by combining these two approaches, it is possible to get the benefits of both approaches, and a large variety of well defined micro- and nano-structures can be efficiently produced. A good example of combining top-down and bottom-up approaches is guided self-assembly, where self-assembly takes place in predefined structural confinements and, as a result, a large variety of structures can be produced efficiently. CFL is based on the same idea.

In a typical CFL experiment, as shown in **Figure 2.1 (a)**, an elastic patterned mold (usually made of cross-linked PDMS) is first brought into conformal contact with a polymer film (usually a thermoplastics, such as polystyrene, heated above its glass transition point), then the fluid fills the cavities on the mold via capillary action which, after phase transition, forms nano-structures on the substrate, and finally the mold is separated from the solidified substrate [Suh (2001)]. Although this procedure is very similar to the traditional method of wax-sealing official documents known as hot-embossing, the uniqueness of CFL is that, due to the much smaller feature size, the main driving force implementing the filling of fluids into the cavities on the mold is capillary force rather than external applied pressure. Capillary force, as one of the predominant forces at the nanometer size-scale, can be used not only to expedite micro- and nano-scale imprint lithography, but also to enable the formation of diverse functional features on the lithographic products with details finer than those of the original molds [Suh (2001), Suh (2002), Bruinink (2006)]. These additional features are produced in the form of meniscus, and thus can only be obtained in cases of partial filling, as shown in **Figure 2.1 (b)**. Previously, Bruinink *et al.* have reported a technique of using the edge of a meniscus formed by capillary force lithography (CFL) as a mold of making second-generation stamps with increased resolution. Moreover, it has also been shown in CFL experiments that ring-like structures can be made taking advantage of the height variations of menisci formed in cylindrical capillaries [Jung (2007)]. However, so far only linear or ring-like structures have been reported.

In this work, we extended previous research in this area by exploring a variety of geometric shapes that contain more than one corners, starting from the simplest, most symmetrical

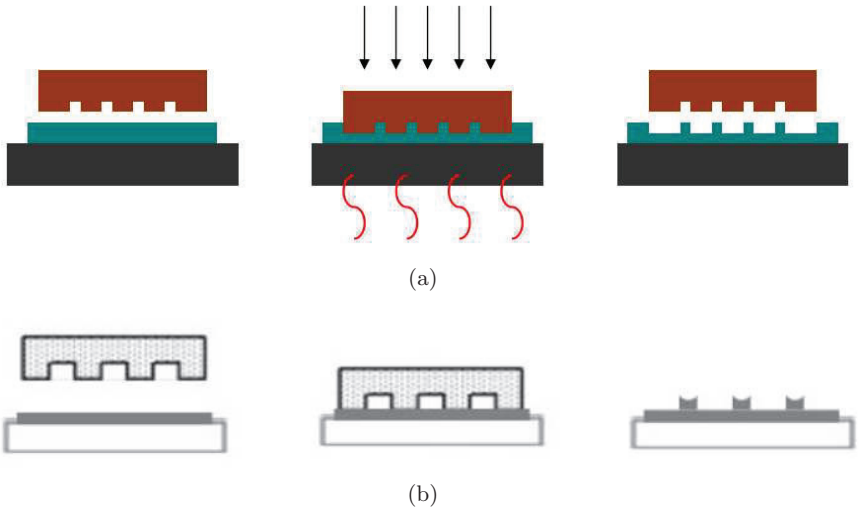

Figure 2.1. Schematics of capillary force lithography. (a) In the case of a thick polymer film, cavities in the mold are fully filled by the imprinted polymer. No meniscus is formed. (b) Curved menisci are formed when the polymer film is thin enough, and the cavities in the mold are only partially filled by the polymer.

shapes − triangle and rectangle. The emphasis was on understanding how menisci respond to confinements at these corners. Our speculation was that confinement due to a corner would cause the formation of a spike: imagine a cylindrical capillary partially filled with a wetting fluid, a concave bowl shaped meniscus is formed at the top of the fluid; if similar capillary action occurs in a capillary with rectangular cross section, the meniscus should still look like a bowl towards the middle. With the same curvature extend outwards, the meniscus would intersect the side walls at four curves, and spikes would form wherever two curves meet, i.e., at the corners, and crown-like structures should be resulted, as shown in **Figure 2.2**. In fact, this effect has been shown in previous studies addressing a very different set of problems C liquid fuel storage in the weightlessness of space flight [Finn (1986)]. Although they serve as an excellent proof-of-concept for the work, their focus was primarily the existence criteria for dichotomous behavior of the meniscus and the meniscus shape and height were not fully quantified. Moreover, The formation of this type of crown-like menisci under corner confinements and proper wetting condition is of particular interest at the micro- and nano-scale, both in terms of providing us with new understanding of

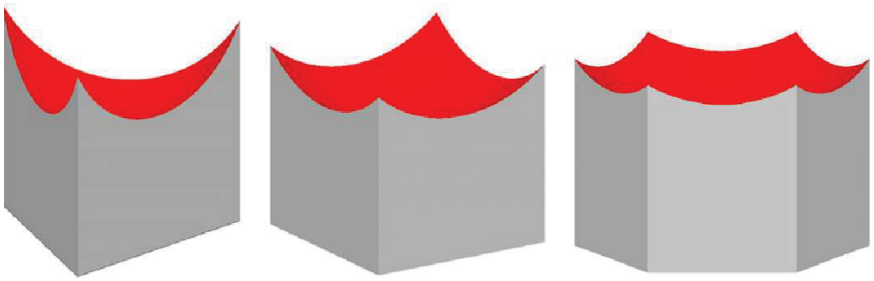

Figure 2.2. Spike formation on the meniscus due to the confinement effects generated by corners.

the basic physical mechanism behind the combined effects of surface tension and geometric confinement, and on the engineering perspective, to develop an efficient parallel method for producing hierarchical micro- and nano-structures. Specifically, this mechanism indicates that surfaces with three-dimensional nano-scale structures can be fabricated from templates with micron or sub-micron features through the development of cusps in the corners of the polygonal capillaries.

2.2 Numerical Simulations

There is a relatively small number of previous simulation studies addressing the issues specific to the three-dimensional shape of capillary surfaces in complex, non-circular, geometries [H. Wong (1992), Mittelmann (1996), Concus (2000), Y. K. Chen (2004)]. Additionally, it is important to note that none of these papers specifically addressed CFL or the issues specific to CFL. In these studies, the contact line was sometimes neglected. Even when proper boundary conditions were applied, the height variation was usually not specified, or the geometry was simply too general. For CFL, it is of great importance to specifically focus on the height variation of the meniscus because that dictates the additional functionality associated with the third dimension, specifically, the contrast of anisotropic etching if the resulting structures are to eventually be used as an etching mask. The geometries and wetting properties implemented in our simulations were chosen to investigate a number of important practical aspects of CFL, including the impact of rounding the corners of the polygons. In our numerical simulations, the position of the contact line and the

shape of menisci at equilibrium was obtained via minimization of total surface energy under geometric confinements and volume conservation. The important factors that govern the geometric characteristics of the resulting structures were investigated. These parameters included contact angle, surface tension, number of sides of the polygon or star as well as the radius of curvature and angle of the polygonal corners. We will show that smaller contact angles, cross sections with smaller internal angles or smaller corner rounding lead to taller cusps on the crown-like-menisci. Our results present the dependence of the height of those cusps on contact angle and cross-sectional geometry. Finally, we will show that star-shaped capillaries can be used to produce super-fine, high aspect ratio, three-dimensional hierarchical structures in capillary force lithography. It is worth mentioning that, in CFL a viscous liquid (e.g., polymer melt) is typically used instead of a Newtonian liquid. Also, the hydrostatic pressure inside the cavity is changing with time [Suh (2004)]. These factors play critical roles in the kinetics of the fluids. In our study, however, since we are mostly interested in the thermodynamic equilibrium, these factors do not affect the results. Specifically, the non-Newtonian nature of the fluids might affect the growth process due to their viscoelasticity the variation of their viscosity as response to shear, but that does not change the equilibrium states. The hydrostatic pressure inside the cavity is always isotropic, which means that it could only affect the height of the fluid column but not the shape of the meniscus.

2.2.1 Surface Evolver

Surface Evolver (SE) was used to simulate the equilibrium state of a fluid body inside a capillary. The Surface Evolver is an open-source computer program which uses a gradient descent method to minimize the energy of a surface subject to constraints [Brakke (1992)]. In SE, the numerical representation of the physical system is based on the finite element discretization. More specifically, each surface is discretized by triangulation into a set of vertices and a set of edges each of which connects two nearby vertices. To facilitate modeling, several types of geometric elements are predefined, including vertex, edge, facet, body, and constraint. Basically, a vertex is parametrized by a set of coordinates, then an edge (a straight line) is uniquely defined by a pair of vertices, then a facet (a flat triangle)

is uniquely defined by an oriented list of three edges that complete one of the smallest closed loops (i.e., there is no edge inside the loop if it is a smallest loop), and finally a body is defined by a set of facets that enclose a volume. Any one of the vertices, edges, and facets may be required to lie on one or more level-set constraints as long as they are geometrically consistent, and any one body may be constrained by a fixed volume. If a higher-level entity is subject to constraints, all the lower-level entities that belongs to it are automatically subject to at least the same set of constraints (or more if individually specified). If the mesh is refined, the new entities generated during the refinement will inherent the same constraints as the entities from which they are produced. For example, when a facet undergoes a normal refinement procedure, the mid-points of each of the three side-edges of this facet will first be generated, and then the three edges connecting every two of these mid-points will be generated, and finally the initial facet is divided into four smaller facets. If the initial facet was bounded on a plane, then all the new vertices, edges, and facets generated during the above procedure are automatically bounded on the same plane. The fixed-volume constraint of a body is implemented by the following procedure: at each interaction step, the integral of z over x and y, which is the volume, of each body is computed. Then the gradients of constrained volume at each vertex is calculated, so that the direction and the distance by which the configuration vector needs to be moved to reach the constraint target can be solved.

In numerical simulations where continuous entities (with one, two, or three spacial dimensions) are each represented by a set of discrete nodes (a node has zero spacial dimension, i.e., it has position but no physical size), also know as finite-element type methods, the discretization (meshing) scheme (mainly including the mesh density and the mesh density distribution) can significantly affect the simulation results quantitatively and sometimes even qualitatively. Generally, for a first order method, such as the ordinary gradient descent used in SE, the uncertainty of the simulation result is proportional to the mesh density (which can be linear density, area density, or volume density, depending on the dimension of the continuous entities it represents), and so is the simulation time. Similarly, for second order methods, such as the conjugate gradient in SE, those quantities are proportional to the second power of the mesh density. To balance error tolerance and resource consump-

tion, a popular meshing scheme is to have nodes more densely populated within the regions of interest while more sparsely populated anywhere else. Quantitatively, it is desirable to have the local mesh density set to be proportional to the local curvature of the surface. SE generally gives high-quality meshes because of the physics model and the evolution algorithm it uses. In each evolution step, the length and orientation of the edges connected to each vertex are modified to reduce the energy of this vertex. As a result, for surfaces with positive surface energies, the vertices will spontaneously aggregate to regions with high curvatures, while for surfaces with negative effective surface energies, the opposite is true. The reason why here we choose an alternating evolve and refine strategy is because this strategy provides both high efficiency and high precision. At the beginning of the evolution when the mesh is coarse, fast movements of the vertices and large deformations of the meniscus take place, and as a result the energy converges quickly. At the end of the evolution when the shape of the meniscus is close to its equilibrium shape, fine and locally concentrated mesh enables precise adjustments of the vertices to capture the energy minimum.

A typical evolution in SE is usually carried out as the following (**Figure 2.3**): Initially, a bulk of fluid, represented by a very coarse mesh, is defined with a fixed volume bounded by a set of planar and/or one-sided constraints. As many steps as needed are then performed to bring the simulation system to its lowest energy state under this coarse mesh. After that, the mesh undergoes one refinement, which means the mid-points of every edges (except for those that are declared no_refine) are generated, and so are the new edges connecting them and the new facets resulting from the edge generations. Next, the system evolves to its lowest energy state again but under a new, finer mesh. By repeating this process of alternating refining the mesh and evolving the system, it is possible, after finite steps, to reach the equilibrium state with a certain target mesh density (or resolution). There are three factors to be paid attention to during this process. First, if allowed, vertices spontaneously migrate towards higher curve regions of the surface, which in turn amplifies the local curvature variations of the surface. This behavior is helpful for developing a high-quality mesh, because in order to capture the same level of detail, regions with higher curvatures need to be populated with higher vertex density so that the smoothness is more or less uniform across the entire surface. However, due to this effect, it is possible that

some vertices may get very closed to one another, or some facets may shrink to very small areas. These tiny edges and facets need to be eliminated, otherwise they could significantly slow down the simulation or even cause instability issues. Second, it is often possible to accelerate the evolution by using a conjugate gradient method, in which case the cumulative history vector is combined with the ordinary step-wise gradient to figure out the conjugate gradient direction. Conjugate gradient method is design only for quadratic energy functions and should only be used when the system is not too far away from equilibrium to prevent overshooting. Third, depending on the initial condition and the energy landscape, at any point of the evolution, the system can be arbitrarily far away from equilibrium and can be approaching equilibrium arbitrarily slowly. The equilibrium state of a system is generally path independent unless the system has more than one state with the exact same energy equal to the global minimum of the energy landscape, so in most cases the initial condition should not affect the simulation result. However, there are a few more situations where the equilibrium state of a system might be hard to get to by simulations based on gradient descent: (a) for systems that have deep local minimums comparing to thermal excitation, the simulation might be dynamically trapped inside a local metastable state. (b) for systems whose energy landscape near equilibrium is flat comparing to the resolution of the data-type used in the simulation (assuming, as common practice to reduce rounding errors and achieve best efficiency, all relevant parameters in the simulation have already been properly rescaled by normalizing the characteristics quantities to be 1), the program might not be able to reach the energy minimum within a reasonable amount of time and error range. Hence, it is generally a good idea to check the convergence by (a) starting the simulation at various initial states and see whether the final equilibrium states are the same, and (b) giving a small perturbation to the numerically converged system to kick it away from convergence and then evolve it again.

2.2.2 Setup for the CFL Simulations

For simulations in this project specifically, a bulk of fluid first is defined with a fixed volume bounded by a set of vertical planar constraints which represent the side walls (with no penetration) of the capillary and a horizontal planar constraint at the bottom (to rep-

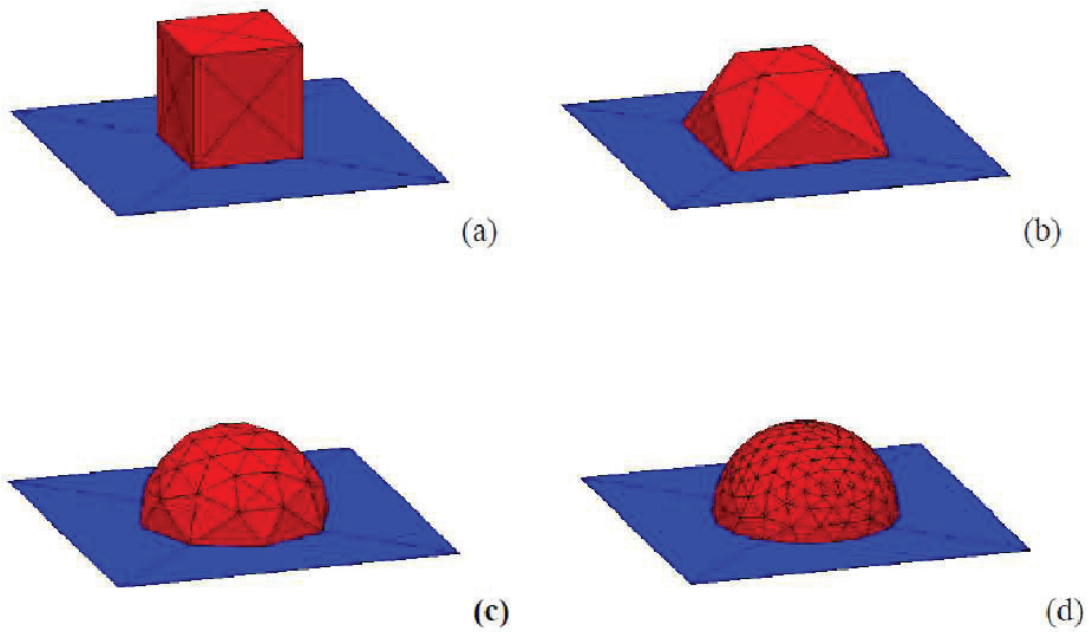

Figure 2.3. A typical evolution in a Surface Evolver simulation.

resent permanent attachment on the substrate). This simulation technique cannot be used to simulate the dynamics of capillary rise. However, this model will give the correct result for the equilibrium state of the meniscus because the equilibrium state is path independent. To study the evolution of the equilibrium meniscus in capillary force lithography, two categories of cross-sectional geometries were simulated − polygons and stars. In each category, geometries with both sharp corners and rounded corners with a broad range of radii of curvature were studied. Regular convex polygonal cross sections were centered at the origin and circumscribed by a circle corresponding to a radius of physical dimension $r = 100$ nm. Polygonal cross sections with rounded corners are created by trimming the corners of the regular polygons into circular arcs with radii of curvature from $R = 0.1\ r$ to $R = 0.3\ r$. Each of these round arcs is tangent to both sides of the corner in which it is placed, as seen in **Figure 2.4**. To facilitate comparisons between different geometries, all rounded polygons with the same symmetry order share the same regular polygonal frame. Similarly for star geometries, the radius of circumscribed circle is fixed to be $r_o = 100$ nm, while the radius of inscribed circle (on which all the concave corner vertices lie), r_i varies between 20 nm and

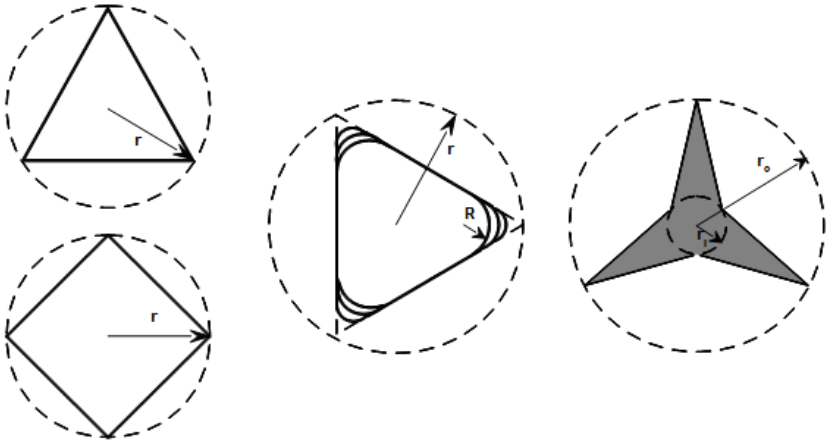

Figure 2.4. Schematic diagrams of cross sectional geometries: (left) regular triangle and rectangle, with radius of circumscribed circle r; (middle) rounded corner triangle with various corner rounding radius R; (right) three-armed star with sharp corners, the convex corners of which all lie on the circumscribed circle with radius r_o, while the concave corners all lie on the inscribed circle with radius r_i. Additional note for star-shapes: the convex corners can also be rounded just like those of the triangle (figure not shown here).

50 nm. This is shown schematically in **Figure 2.4**. The same manipulations are carried out in order to generate star geometries with rounded corners as described previously for polygonal geometries.

After a cross-sectional geometry is generated, it is defined to the Surface Evolver as a set of planar constraints which are applied to x and y and apply for all values of z. Vertices on the constraint planes are bounded on the plane at all time (but are allowed to move along the plane). The tube defined by these constraints is then filled with a column of fluid with an initial height equals to the circumscribing radius. As an initial state, the top and bottom surfaces of the fluid column are both flat and horizontal. During an evolution, all the side surfaces of this fluid column are in intimate and permanent contact with the walls of the tube, and its bottom surface is permanently bounded on the plane constraint $z = 0$. The top surface is free to adopt any shape that minimize the total energy of the system consists of both the fluid body and the capillary tube.

Typically, surface forces scale with the length of the contact line and therefore the first power of the characteristic length, which in our case is the radius of the circumscribed

circle. Conversely, body forces scale with the volume and therefore as the third power of the characteristic length. As a result, the smaller the length, the more dominant the surface forces become. For this reason, surface forces play an important role in material behaviors at small size-scales while gravitational effects can be neglected [de Gennes (1985)]. In this study, the characteristic length scales of the fluid systems are set between 100 nm and 1 μm. Since the algorithm used by the Surface Evolver is unit independent, the size effects are translated into the value of the gravitational constant. By using a unit analysis based on comparing the gravitational force and the surface tension, it is calculated that the effective gravitational constant for our characteristic length scale is essentially zero.

In this discussion, only the partial wetting regime is considered, where the contact angle between the fluid and the side walls of the capillary is $\theta < 90°$. The contact angle, θ, always refers to the (equilibrium) material contact angle defined by the Young equation. The side walls of capillary are always assumed to be smooth, homogeneous, and rigid. Additionally, no hysteresis of contact angle is considered, although in the corresponding experiments the results will likely be dependent on the advancing contact angle because it is a capillary filling process. For every cross-sectional geometry there exists a critical contact angle due to Plateau-Rayleigh interfacial instability [Brakke (1996), Concus (2000), Y. K. Chen (2004)]. Under partial wetting condition, if the contact angle between the fluid and the wall of the capillary is larger than or equal to that critical value, the equilibrium extent of the meniscus growth along the length of the capillary is finite. However, if the contact angle is smaller than this critical value, the equilibrium meniscus can become infinitely long. Finn *et al.* have shown through a rigorous mathematical analysis that at a sharp corner the critical contact angle is $\theta_c = \pi/2 - \alpha$, where α is half of the internal angle of the corner.

2.2.3 Termination Criteria for the CFL Simulations

Once the geometry was defined, Surface Evolver was used to determine the equilibrium shape of the meniscus. Each simulation consisted of three stages − initiating, approaching, and stabilizing − to gain faster convergence. In the initiating stage, three refinements to each edge with length greater than $0.05r$ (or $0.05r_o$ in the star geometry cases) were performed. Each refinement was done by putting a vertex at the midpoint of a targeted

edge so that it could be split into two edges each with half the length of the initial one. At this stage, as many steps as needed were performed to bring the energy gradient down to less than 10×10^{-8} per 10 steps. The simulations were continued to the stabilizing stage, where as many refinements and evolutions as needed were performed to satisfy a set of equilibrium criteria.

The extent and shape of the final, equilibrium meniscus was extracted and analyzed to understand the trends. With respect to Capillary Force Lithography, the quantity of most interest is the difference in elevation between the highest and the lowest points on a meniscus, which we will refer to as h from this point on. To match the sign of elevation with that of the cosine of the contact angle, a convention is used where concave menisci have positive elevations while convex menisci have negative elevations. Since the final state of the meniscus is usually a curved surface, and in Surface Evolver a curved surface is discretized into a union of flat triangular facets, the sizes of these facets, or grid resolution, can affect the final shape of the meniscus [Mittelmann (1996)]. Finer grid resolutions give more accurate shapes but the simulations take a longer time to converge. Moreover, the change in energy with each step slows as the system approaches equilibrium. Thus a threshold of this energy gradient is needed to determine whether the system has reached equilibrium. A series of convergence tests were performed using the regular polygon geometries. Based on these test results, a set of criteria according to which equilibrium is determined are chosen as following: maximum length of a single edge less than 5.0 nm; minimum length of a single edge greater than 0.5 nm; equiangulation is completed; the change of energy (as evaluated by Surface Evolver) within the last ten steps is smaller than 10×10^{-10}. This set of equilibrium criteria corresponds to a less than 1% change in the value of elevation in all the geometries and contact angle values that have been studied. Since the maximum elevation we have observed is on the order of 100 nm, one percent of the elevation corresponding to actual physical dimension less then 1.0 nm. When plotted at a log-log scale to find the characteristic power index, this error has no measurable effect on the results. The dependence of elevation on the other parameters studied produced variations in the meniscus height much larger than the 1.0 nm uncertainty due to resolution effects.

2.3 Simulation Results

The shape of meniscus formed in a cylindrical capillary is a classically studied problem. Below the capillary length, surface tension dominates over gravity and the meniscus formed inside the capillary adopts a shape very close to a portion of a sphere. For pure water at standard temperature and pressure, the capillary length is about 2.7 mm. Polymeric fluids typically have much lower surface tensions then water resulting in capillary lengths on the order of hundreds of microns. For a cylindrical capillary with a radius of $r = 100$ nm, it can be therefore assumed that the shape of the meniscus is a spherical cap. In this case the analytical solution for elevation, h, as a function of cross-sectional radius, r, and contact angle, θ, can be shown to be:

$$h = r\left(1 - \sqrt{1 - \cos^2\theta}\right) / \cos\theta. \tag{2.1}$$

When $\cos\theta \to 0$, $h \to (r/2)\cos\theta$; and when $\cos\theta \to 1$, $h \to r\left[1 - \sqrt{2(1-\cos\theta)}\right]$. The predictions of the meniscus height from our simulation of cylindrical capillaries are superimposed over the analytical solution in **Figure 2.5** inset. The simulations match the theory very well over all the contact angles tested. Plotting h versus $\cos\theta$ in a log-log scale (**Figure 2.5**), we can see that at small and medium $\cos\theta$ the slope mostly remains constant, which indicates a power law dependence of elevation over $\cos\theta$; at the regime where $\cos\theta$ is close to one, however, the slope increases very rapidly. The power index measure from the linear portion of the log-log plot is approximately 1.05 (the slope of the fit line varies slightly depending on the range of $\cos\theta$ over which fitting is performed).

For patterns of lines, the elevation of the meniscus due to the confinement of parallel walls can be easily calculated analytically: $h_L = (1 - \sin\theta)d/2$, where d is the spacing between the parallel walls. This, of course, is only an exact solution for an infinitely long straight line where the effects on the meniscus from the ends of the line can be neglected. If, however, we consider a straight line with finite length, the existence and shape of the line's endcap must be accounted for, as it will induce a secondary curvature along the length of the line. The majority of the meniscus located towards the midpoint of the line and away from the ends should remain two-dimensional. However, the exact the shape of the

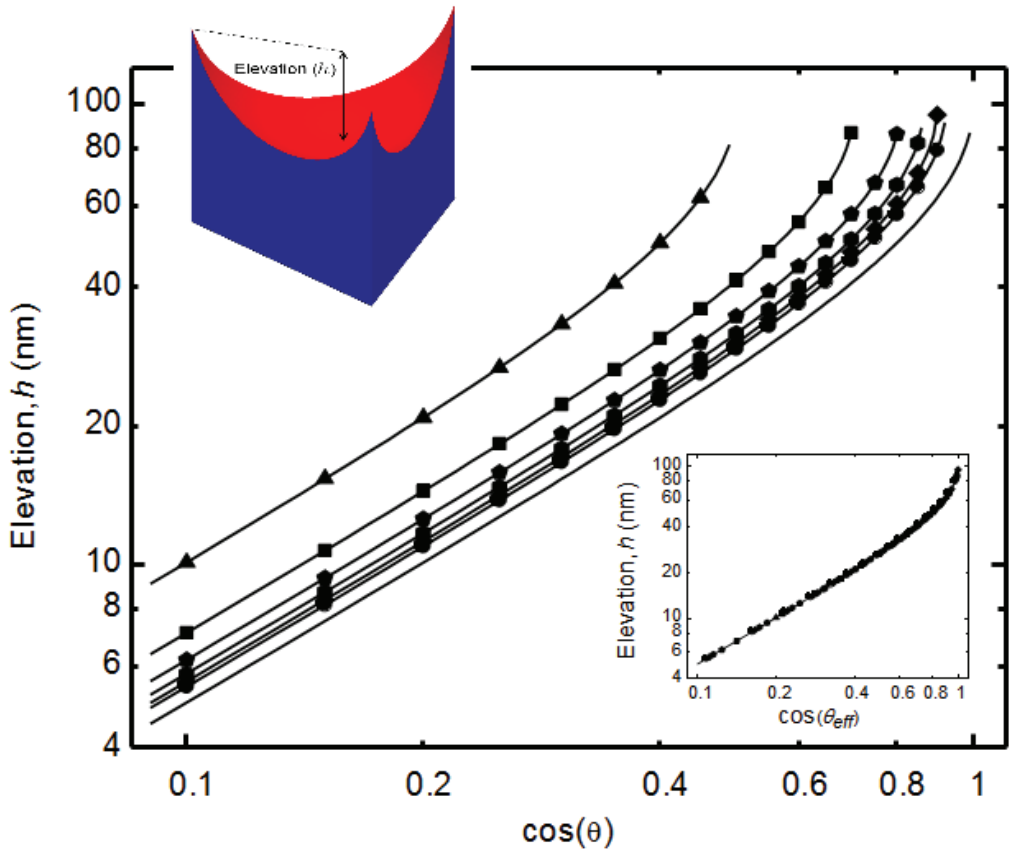

Figure 2.5. Elevation of meniscus, h, as a function of contact angle, θ, for capillaries whose cross-sections are regular polygons with sharp corners. Data points are from simulation. Cross-sectional geometries including: ($\triangle$) triangle, ($\square$) square, ($\pentagon$) pentagon, ($\hexagon$) hexagon, ($\diamond$) heptagon, and ($\bigcirc$) octagon. Also plotted are the analytical solutions of elevation resulted in regular polygonal and circular cross section as a function of contact angle (solid lines). The inset shows the elevation curves collapse onto a single line when plotted against cosine of effective contact angle; discrepancy for any one of those data points is less than 1% .

meniscus near the ends of the lines is more complicated and, as we will see in the case of regular polygons, is directly related to the details of the shape of the endcap (polygonal or circular), the contact angle between the fluid and the walls of the capillary and the curvature of any sharp corners.

2.3.1 Simulation Results: sharp regular polygons

For sharp regular polygons, the shape of a capillary can have a large impact on the resulting meniscus shape and height. Here we investigate a series of capillaries with cross sections as regular polygons each of which is circumscribed by a circle with radius $r = 100$ nm. As before, gravity is negligible and the fluid partially wets the capillary. For these geometries it has been shown that these menisci are in fact sections of a sphere much like the cylindrical capillary if the material contact angle is not less than the critical contact angle [Finn (1990)]. A simple way to understand this solution is shown schematically in **Figure 2.6**. Start with a vertical plane P intercepting a sphere S whose center is point O. Fix the distance, d, between plane P and point O, while allowing the radius, R_S, of sphere S to vary. When $R_S = d$, P is tangent to S, and the normal of P lines up with the local normal of S at the tangent point, i.e., intercepting angle $\beta = 0°$; when $R_S \to \infty$, the intercepting angle $\beta \to 90°$. For any particular value of R_S between d and ∞, the intercepting angle β is a constant at every point on the intercepting circle due to rotational symmetry about every horizontal line that go through point O. The value of β can be anywhere between 0° and 90°, and it is a function of R_S only. Since all the sides of a regular polygon have the same distance to its center, based on the argument above, a spherical meniscus (here, in fact, only the lower hemisphere is needed; the upper hemisphere corresponds to cases where contact angle is between 90° and 180°) can satisfy any specified contact angle at every point on the contact line on every side wall. Moreover, a sphere has constant mean curvature at every point, which satisfies the requirement of uniform Laplace pressure across the interface.

Changing the cross-sectional geometry from a circle to a regular polygon is effectively only changing the radius of the spherical surface on which the meniscus lies. This in turn is physically consistent with changing the contact angle θ. For a regular polygon, it can be found that the new radius is $R_S = r \sin\alpha / \cos\theta$, where $\alpha = (n-2)\pi/2n$ is half of

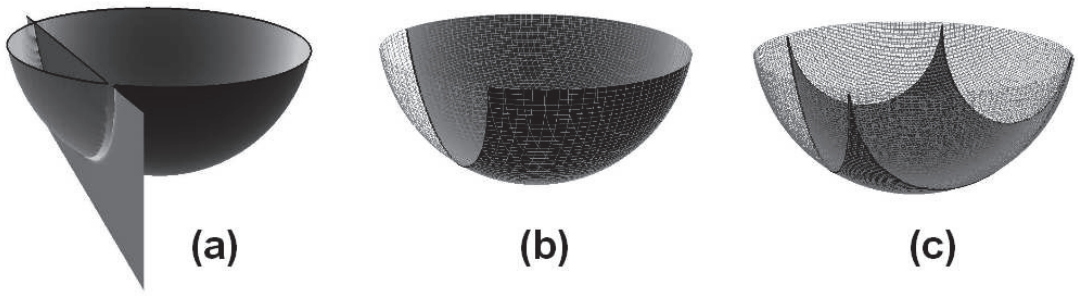

Figure 2.6. Schematics of the construction of analytical solution. (a) a hemisphere intercepted by a plane; (b) the intercepting angle between the plane and the hemisphere is the same at every point due to rotational symmetry; (c) the meniscus formed in a rectangular capillary is part of a hemisphere.

the internal angle of a corner of an n-sided regular polygon. The elevation, or the height difference of the meniscus between the center and a corner of the capillary, is:

$$h = r \sin\alpha \left[1 - \sqrt{1 - (\cos\theta / \sin\alpha)^2}\right] / \cos\theta. \tag{2.2}$$

At the limit of $n \to \infty$, the result for a circular cross section is obtained. **Figure 2.5** shows elevation as a function of contact angle calculated based on this analytical solution for cross-sectional geometries as triangle, rectangle, pentagon, and hexagon. It is immediately clear that if the available contact angles are limited to relatively close to 90°, which is usually the case for CFL due to the low surface tensions of PDMS and polymer melts, it is possible to take advantage of triangular geometry to achieve relatively high elevation differences across the meniscus.

Define an effective contact angle, θ_{eff}, such that $\theta_{eff} = \cos\theta / \sin\alpha$, then all the data for the sharp regular polygons in **Figure 2.5** collapse onto a single master curve, as shown in the inset of **Figure 2.5** which plots h as a function of θ_{eff}. Physically, this effective contact angle θ_{eff} is the angle between the differential portion of the meniscus at the corner of the cross section and the side edge of the capillary. Notice that when $0° < \theta < 90°$, θ_{eff} is always less than θ. The instability of a meniscus formed in a polygonal capillary occurs at the corners first. As a result, the critical contact angle for a regular polygonal capillary

Table 2.1. Reciprocal sine of half internal angles, critical contact angles and the cosine of critical contact angles for cross-sectional regular polygons with different orders of symmetry.

Geometry	Triangle	Rectangle	Pentagon	Hexagon	Heptagon	Octagon	Circle
$1/\sin\alpha$	2.000	1.414	1.236	1.155	1.110	1.082	1.000
θ_c	60.0°	45.0°	36.0°	30.0°	25.7°	22.5°	0.0°
$\cos\theta_c$	0.500	0.707	0.809	0.866	0.901	0.924	1.000

is reduced to $\theta_c = \pi/n$, where n is the number of sides. Values of critical contact angle for regular polygons are listed in **Table 2.1**.

The equivalency between changing cross-sectional geometry and rescaling of the contact angle also implies that the upper limit of elevation of a stable meniscus is the radius of the circumscribed circle of the cross-sectional polygon, r, because that is the best of what a circular cross section can provide (with 0° contact angle so that the meniscus is exactly the lower hemisphere). However, with a triangular cross section, for example, the stability limit can be approached with much larger contact angles and such heights cannot be achieved. In order to understand the effect of wettability of the meniscus shape, simulations were performed for material contact angles in the range between θ_c and 90°. **Figure 2.5** plots the simulation results of the elevation of menisci formed in polygonal cross sections versus the cosine of material contact angles. All curves for regular polygonal cross sections follow the same trend, and when θ is converted into θ_{eff}, as shown in the inset, all those curves collapse on top of the curve for circular cross section. When the simulation results are compared with the analytical results, the discrepancy of any individual data point is below 1%, which demonstrates the reliability of the simulation procedure. Notice on the log-log plot, within the range where $\cos\theta_{eff}$ from 0.1 up to 0.7, or equivalently θ_{eff} from 85° down to about 45°, the response of elevation to the change of $\cos\theta_{eff}$ is fairly linear (the portion is fairly straight and the slope is close to 1.0), and this linear portion covers about 40% of the elevation range. For the other half of the effective contact angle range, from 45° to 0°, the height *v.s.* contact angle behavior is highly non-linear. As a result, a relatively small reduction in θ_{eff} can result in a significant increase of elevation. As a side note, when the contact angle is between 90° and 180°, it is easy to prove based on symmetry that the

equation $h = r\left(1 - \sqrt{1 - \cos^2\theta_{eff}}\right)/\cos\theta_{eff}$, only now the resulting elevation is negative because the meniscus lies on the upper hemisphere, or $h(\cos\theta) = -h(\cos(\pi - \theta))$ when 90° $\leq \theta \leq$ 180°. Practically, this means that if one chooses to use a low adhesion pair of fluid and solid for easier separation between the mold and the product after CFL, one needs to also realize that this choice may also hinder the filling of fluid into capillary especially in small dimensions and at sharp corners.

2.3.2 Simulation Results: rounded polygons

Experimentally, it is difficult to fabricate nano-scale capillaries with perfectly sharp corners. In fact, when doing CFL of nano-scale features, the corners of the structures on the mold are always rounded to some degree. To better guide the design of CFL experiments, a series of simulations were performed for geometries with regular polygonal cross-sections and rounded corners. As a first approach the rounding of polygon corners was chosen to be circular and tangent to both sides of the included angle. The intuitive expectation is that the rounding of corners should reduce the elevation of the meniscus when compared to the same geometry with sharp corners and the same material contact angle. In addition, we expect rounding the corners will allow the meniscus to be stable over a larger range of contact angles because as the rounding radius increases the meniscus formed within the polygonal capillary should eventually approach that formed in a circular capillary.

The response of meniscus elevation to the change of contact angle is shown in **Figure 2.7 (a)**. The results for triangular cross sections with rounded corners with rounding radii of 10 nm, 20 nm, and 30 nm behave similarly with changing contact angle to those of regular polygons, showing an elevation decrease as the corner rounding is increased. All curves appear to be qualitatively similar, but shifted with respect to $\cos\theta$. One way to quantify the change in response is to determine the slopes of the linear portion of curves in **Figure 2.7 (a)**. Although they appear very similar at small values of $\cos\theta$, there are small differences in the functional dependence of $h \propto \cos^k\theta$. The power of the polynomial is found to decrease from k = 1.08 for the sharp case to k = 1.04 for the case where R = 30 nm. In particular, with increasing rounding radii curves shift to the right, but the shifting becomes slower when rounding radii get larger. These observations indicate that

the effective contact angle increases with increasing rounding radius. If one instead looks at the elevation of the meniscus as a function of rounding radius, as shown in the inset of **Figure 2.7 (a)**, this shifting effect can be quantified. The characteristic length scale (the radius of circumscribed circle) is kept to be 100 nm, and the rounding radii are 10 nm, 20 nm, and 30 nm in the simulation results presented here. As seen in the inset of **Figure 2.7 (a)**, there are clear power-law dependencies of elevation on rounding radius, which vary from -0.29 to -0.45 over the span of $\cos\theta$ values from 0.1 to 0.8. The specific values of the slope of **Figure 2.7 (a)** inset are listed in **Table 2.2**. It is worth emphasizing that the power law relations we present here are useful in understanding dependencies, however, they should not be extrapolated to the region where R (rounding radius) is significantly smaller than 10 nm because they lead to a singularity at $R = 0$, the case where corners are perfectly sharp.

For completeness, a series of simulations were performed for regular polygons with similar rounded corners cross-sectional geometries. In **Figure 2.7 (b)**, values of h as a function of $\cos\theta$ are presented for rounded triangle, rectangle, pentagon, and hexagon, all with a rounding radius equal to 10 nm at each corner. As expected, the elevation decreases in all cases in comparison to the same polygon with sharp corners shown in **Figure 2.5** and **Table 2.3**. As seen with triangles, the sharp and rounded data are qualitatively the same, just shifted to smaller heights. It is worth noticing that the reduction of elevation for rounded polygons is not only the result of the reduction of confinement due to corner rounding, but also due to the fact that rounded polygons have slightly smaller cross sectional area than the sharp corner ones as a result of the way they were created, see **Figure 2.4**. If there were only the dimension effect contributing to elevation decrease, one would expect that the menisci resulting from different rounding radii should entirely overlap on top of each other up to the point that the meniscus contacts the rounded corner. To investigate this hypothesis, the position of the contact lines in a series of triangular capillaries with various degrees of corner rounding and the menisci formed in them are shown in **Figure 2.8**. As seen in **Figure 2.8**, the effect of the rounded corner propagates far from the corner itself and changes the shape and nature of the meniscus well away from the corner. Thus it is clearly not simply an area effect.

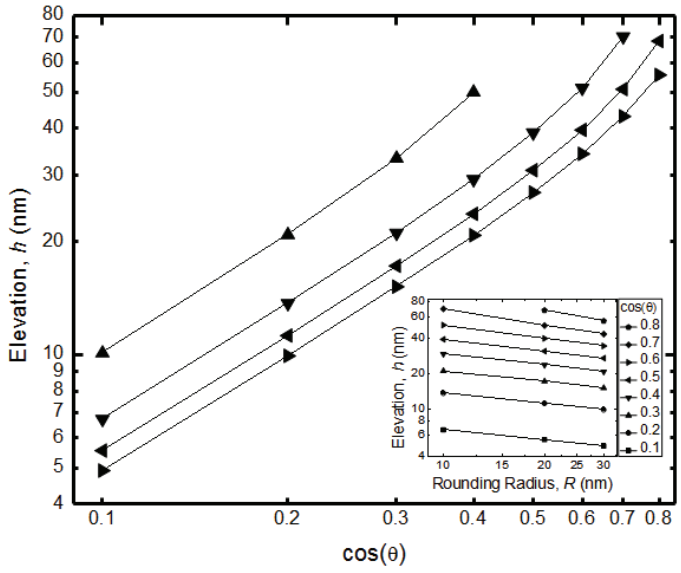

(a)

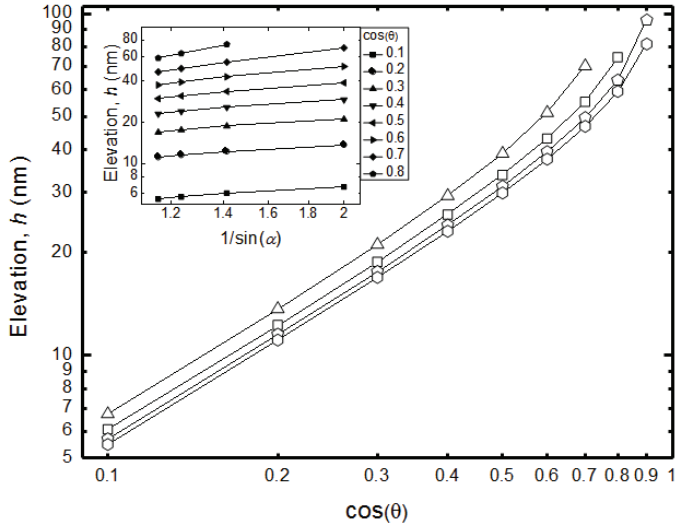

(b)

Figure 2.7. Elevation of meniscus, h, as a function of contact angle, θ. (a) For capillaries whose cross sections are triangles with sharp and rounded corners. Data include: (▲) sharp triangle, triangles with radii of (▼) $R = 0.1$, (◀) $R = 0.2$, (▶) $R = 0.3$. The inset at the bottom right shows elevation as a function of rounding radius, as $\cos\theta$ increases from 0.1 to 0.8 (from bottom to top), showing a linear dependency of the meniscus height on the rounding radius. (b) For capillaries whose cross sections are polygons with rounded corners (where $R = 0.1$ in all cases). Data include rounded: (△) triangles, (□) rectangle, (⬠) pentagon, and (⬡) hexagon. The inset at the top left shows elevation h as a function of $1/\sin\alpha$, as $\cos\theta$ increases from 0.1 at the bottom to 0.8 at the top.

Table 2.2. Comparison of elevations resulting from sharp and rounded polygonal cross sections with different material contact angles.

$\cos\theta$	Triangle		Rectangle		Pentagon		Hexagon	
	sharp	$R = 10$ nm	sharp	$R = 10$ nm	sharp	$R = 10$ nm	sharp	$R = 10$ nm
0.1	10.10	6.74	7.11	6.07	6.20	5.70	5.79	5.49
0.2	20.87	13.69	14.44	12.27	12.56	11.52	11.71	11.10
0.3	33.33	21.10	22.26	18.79	19.22	17.59	17.87	16.92
0.4	49.99	29.31	31.00	25.82	26.45	24.07	24.48	23.11
0.5		38.96	41.42	33.71	34.60	31.23	31.78	29.88
0.6		51.32	55.48	43.06	44.39	39.45	40.25	37.57
0.7		70.27	86.58	55.23	57.63	49.63	50.86	46.82
0.8				74.58	86.07	63.95	66.79	59.20
0.9						95.74		81.50

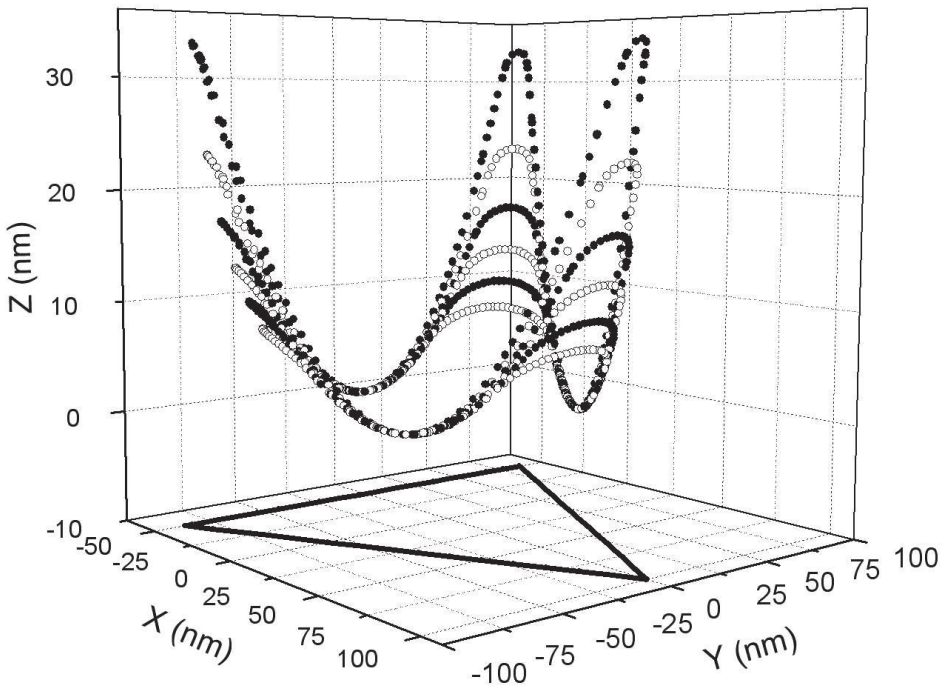

Figure 2.8. 3D scatter plot of equilibrium contact lines resulting from capillaries with rounded triangular cross sections, rounding radius, R, from 0.05 to 0.30 with 0.05 increments top to bottom. The triangular frame which shared by all cross-sectional rounded triangles is also shown at the bottom. Notice that the Z coordinate is stretched compared to X and Y coordinates to accentuate the deformation of the meniscus.

2.3.3 Simulation Results: sharp regular stars

Polygons, while interesting, are not the only shapes that are fabricated using CFL. If the goal is to maximize the height variation, an intriguing geometry is a regular star. In this section, we present a series of simulations to evaluate elevation of menisci formed inside capillaries with regular star cross sections. The arguments presented in section 2.3.1 can be applied to regular star-shaped cross-sectional capillaries, because all the sides of a regular star also have the same distance to its center. Consequentially, the menisci formed within a star can be described by a section of a sphere if gravity is neglected. The radius of the sphere on which the meniscus lies depends on r_i , r_o , n, and θ with the following relationship:

$$R_S = r_o \sin(\pi/n) / \left[\cos\theta \sqrt{(r_o/r_i)^2 + 1 - 2(r_o/r_i)\cos(\pi/n)}\right], \tag{2.3}$$

where r_o is the radius of the circumscribed circle of the cross-sectional star on which all the convex vertices lie and r_i is the radius of the inscribed circle of the cross-sectional star on which all the concave vertices lie, and n and θ are order of symmetry and material contact angle, respectively. The ratio r_o/r_i depicts the slenderness of the arms of the stars, and thus determines the internal angle of the concave vertices. Similar to polygon cases, smaller internal angle, or greater r_o/r_i ratio, gives smaller R_S. It is indicated by **Equation 2.3** that, at the critical contact angle $\cos\theta_c = \sin(\pi/n)/\sqrt{(r_o/r_i)^2 + 1 - 2(r_o/r_i)\cos(\pi/n)}$, the contact angle geometry combination results in $R_S = r_o$. Any contact angle, θ, smaller than this critical value θ_c will yield an elevation on the meniscus which can be calculated by the equation $h = R_S\left[1 - \sqrt{1 - (r_o/R_S)^2}\right]$, where r_i and r_o are the radii of circles on which the convex and concave vertices lie, respectively, and n is the order of symmetry. The effective contact angle, in this case, can be determined by $\cos\theta_{eff} = l\cos\theta/\left[r_i \sin(\pi/n)\right]$, where $l = \sqrt{{r_o}^2 + {r_i}^2 - 2r_o r_i \cos(\pi/n)}$, then similar to **Equation 2.1**, $h = r_o\left[1 - \sqrt{1 - \cos^2\theta_{eff}}\right]/\theta_{eff}$. Thus, as can be shown for polygons, changing the cross-sectional geometry of a capillary from a circle to a regular star effectively only changes the radius of the sphere on which the meniscus lies. In terms of elevation, it is equivalent to rescaling the cosine of contact angle, and the scaling factor is determined by the cross-sectional

Table 2.3. Cosine and angular values of critical contact angle for regular stars.

	10 nm	20 nm	30 nm	40 nm	50 nm	60 nm	70 nm
three-armed stars	0.091	0.189	0.292	0.397	0.500		
	85.0°	79.0°	73.0°	67.0°	60.0°		
four-armed stars	0.076	0.163	0.260	0.367	0.480	0.593	0.700
	86.0°	81.0°	75.0°	68.0°	61.0°	54.0°	46.0°

geometry. The critical contact angle $\theta_c = \cos^{-1}\left[r_i \sin(\pi/n)/\sqrt{{r_o}^2 + {r_i}^2 - 2r_o r_i \cos(\pi/n)}\right]$ is tabulated for various three-armed and four-armed stars in **Table 2.4**.

The simulation results of meniscus elevation, h, for a series of three-armed stars where the radius of the inscribed circle, r_i , was varied from 20 nm to 45 nm, while keeping the radius of the circumscribed circle $r_o = 100$ nm, are presented in **Figure 2.9 (a)** as a function of contact angle. For comparison, the predictions of theory are superimposed over the simulation data. The simulation results agree very well with the analytical solution. The error of any individual data point is found to be less than 1%. The same level of accuracy is observed with results of four-armed star cross sections as well. As seen in **Figure 2.9 (b)**, after rescaling the contact angles into effective contact angles, all data points of three-armed and four-armed star cross sections collapse on the theoretical curve of cylindrical capillary just as expected.

2.3.4 Simulation Results: rounded regular stars

As mentioned before, some degree of corner rounding is generally inevitable for the nano-scale features on the mold used in CFL experiments. On the other hand, star-shaped cross-sectional geometries provide appreciable capability of producing large elevations at relatively large contact angles. It is useful to find out whether the star-shaped geometry can offer significant elevation improvement in the cases where corners are rounded. Therefore, simulations were performed to study the effects of corner rounding to regular star cross-sectional geometry. Similar to what was observed in the polygon cases, when the convex corners of a star-shape are rounded, the elevation achieved at the point of each arm of the star decreases with increasing degrees of rounding. As mentioned before, this reduction in elevation is the combined result of two effects − slight decrease in length scale and reducing

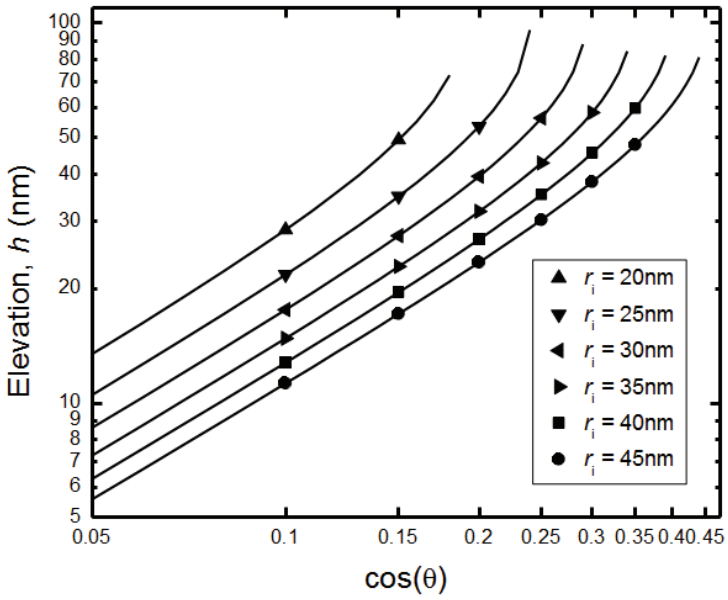

(a)

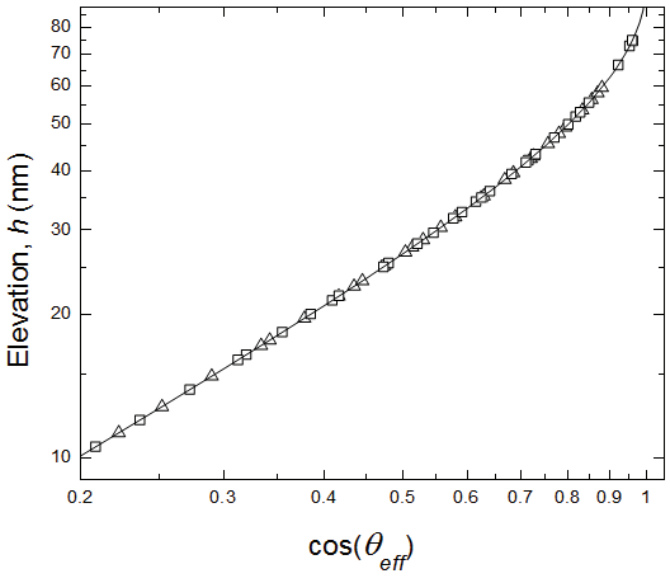

(b)

Figure 2.9. Elevation of the meniscus, h, as a function of the material contact angle θ, and the effective contact angle θ_{eff}. (a) h *v.s.* $\cos\theta$ for three-armed stars with sharp corners. Data points represented by different symbols correspond to simulation results with different r_i values, while keeping r_o to be 100 nm. Solid lines are based on analytical solutions for respective cases. (b) h *v.s.* $\cos\theta_{eff}$ for three-armed stars ($\triangle$) and four-armed stars ($\square$) with sharp corners on a log-log scale. All the data points collapse on the analytical solution for circular cross section (solid line) as expected.

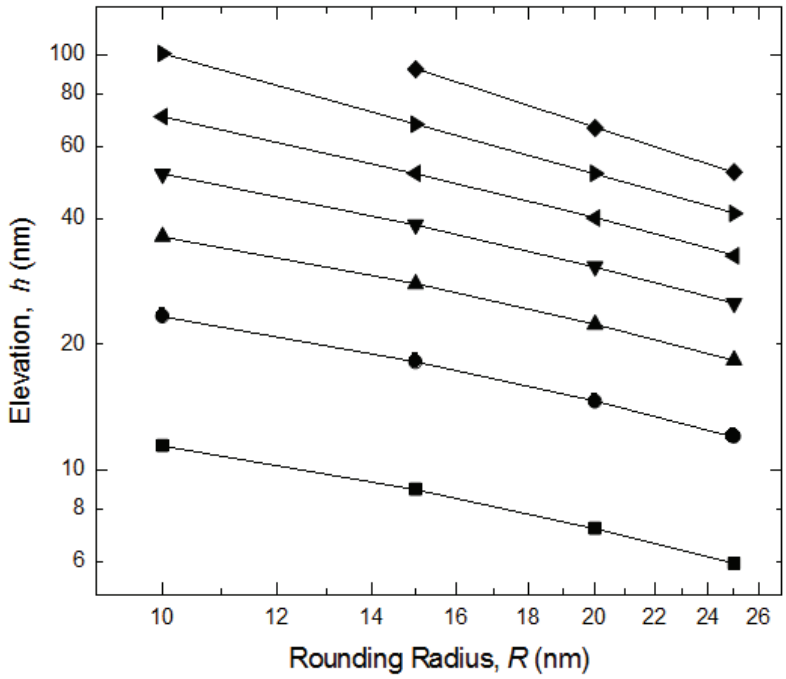

Figure 2.10. Elevation of the meniscus, h, as a function of rounding radius, R, for three-armed stars with the same outer frame ($r_o = 1.5$, $r_i = 0.5$). Each curve represents a different value of $\cos\theta$, including: (■) 0.1, (●) 0.2, (▲) 0.3, (▼) 0.4, (◄) 0.5, (►) 0.6, and (♦) 0.7, from bottom to top.

of confinement at the corners due to rounding. The overall response to corner rounding of a three-armed star is plotted in **Figure 2.10**. Similar results were achieved for the four-armed stars. For cases where rounding radius is moderate, the elevation has a power law dependence on rounding radius. The power law exponent is found to become more strongly negative with decreasing contact angle, ranging from -0.7 at $\cos\theta = 0.1$ to -1.1 at $\cos\theta = 0.7$. These slopes are tabulated in **Table 2.5**.

Considering the sum total of these simulations allows us to focus on some very interesting questions. For instance, what should one do if one wants to fabricate a novel and useful three-dimensional nano-structures that have tunable rotational symmetry and large height variation utilizing capillary effects in lithography? Both polygons and stars will work. However, the star is clearly the optimal geometry. Even when the corners are inevitably

Table 2.4. Slopes of the elevation (h) versus corner-rounding radius (R) log-log curves for rounded triangular and three-armed star-shaped cross sections.

$\cos\theta$	0.1	0.2	0.3	0.4	0.5	0.6	0.7
tiangles	-0.288	-0.293	-0.300	-0.312	-0.333	-0.369	-0.444
three-armed stars	-0.711	-0.722	-0.743	-0.779	-0.841	-0.965	-1.116

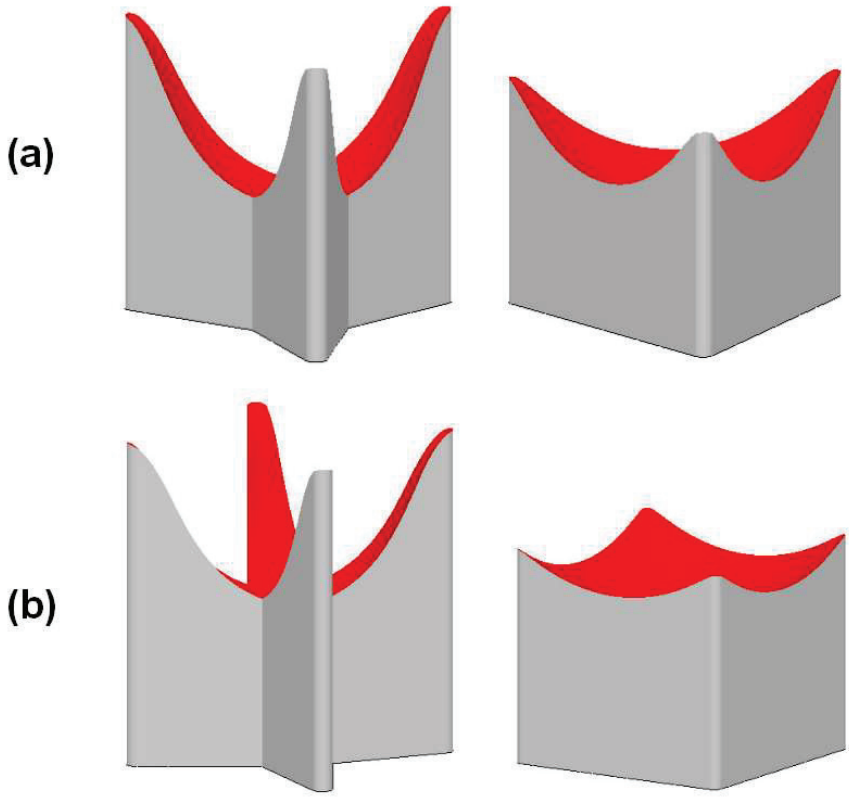

Figure 2.11. Comparison of the meniscus shapes for: (a) three-armed star cross section (r_o = 150 nm, r_i = 50 nm, R = 10 nm, $\cos\theta$ = 0.6) and triangular cross section (r = 150 nm, R = 10 nm, $\cos\theta$ = 0.6) with the same rounding of corners; and (b) four-armed star cross section (r_o = 200 nm, r_i = 50 nm, R = 10 nm, $\cos\theta$ = 0.55) compared with rectangular cross section (r = 200 nm, R = 10 nm, $\cos\theta$ = 0.55) with the same rounding of corners.

rounded due to the limitation of fabrication tools, high elevations can still be achieved owing to the large confinement effects. Let's take a close look at **Figure 2.10** and the elevations corresponding to different rounding radius for a certain set of three-armed stars with $r_o =$ 150 nm and $r_i = 50$ nm. Notice that for a fluid-solid pair with contact angle of about 53° and a corner rounding of 20 nm in diameter, an elevation of approximately $h = 116$ nm can be achieved along the meniscus. For comparison, a triangular cross-section with the same characteristic dimension and corner rounding and same contact angle would result in an elevation of only 77 nm. These two surfaces are presented in **Figure 2.11 (a)** for comparison. This represents just one example of nano-scale claw-like structure that can be formed. If one wants to push the limit to maximize elevation, one could simply choose geometries with higher r_o/r_i ratios, so that the internal corners of the convex vertex of the star shape gets sharper or minimize the corner rounding. Moreover, since confinement factor is independent of symmetry order, one can make nano-claws with arbitrary number of fingers (**Figure 2.11 (b)**) without having to sacrifice elevation. Specifically, for a regular polygon the internal angle is directly related to the number of sides, and the elevation on the meniscus, h, decreases significantly with the increase of number of sides, n, when n ranges from 3 to 6. For a regular star, on the other hand, the internal angle at the convex corners is mostly dependent on the r_o/r_i ratio and is rather insensitive to the order of symmetry. Clearly, the elevation difference between the four-armed star and the rectangle geometries shown in **Figure 2.11 (b)** is much more significant than the elevation difference between the three-armed star and the triangle geometries shown in **Figure 2.11 (a)**.

2.4 Experiments

As already pointed out, the main focus of this CFL project is to study the behavior of a fluid in the capillary-force driven, small-scaled, imprint lithographic procedure, and to explore novel approaches of adding on three-dimensional features by taking advantage of the physical properties, specifically the surface-tension effects. While simulations can serve as a guide and make useful predictions, it is experiments that directly interact with the physical world and produce actual products. Generally, a simulation gets more and more difficult and expensive when more and more different types of specific interactions need to

be included. Contrarily, in experiments effects of multiple interactions are usually coupled together unless special cares are carried out to separate them. As a result, it is difficult to have the exact same systems for simulation and experiment to compare. Main features and trends are usually used for matching.

As shown in **Figure 2.12**, A brief four-step procedure of the experimental portion of this project is as following: First, a patterned master is produced by electron-beam-lithography, sometimes followed by deposition and/or etching. Second, a special fluid mixture of PDMS and cross-linking agent is poured on the master, cross-linked by heating, then the resulting elastic mold is peeled off from the master. Third, the elastic mold with features that are negatively duplicated from the master is placed on top of a thin film of polymer coated on a solid substrate. Finally, the fluid is solidified and then is separated from the elastic mold. This concept of CFL is very similar to hot-embossing which has been performed for a long time, except that the resolution needed here is in the micro- or nano-scales, which means there are a few important factors required special attentions, including: (1) the three-dimensional shape, material composition, and structural and surface properties of the features on the master and more importantly those on the mold; (2) material composition and structural arrangement of the imprint substrate; (3) contact and interaction between the mold and the imprint substrate; and (4) material properties of the mold and the imprint substrate, for both (3) and (4), when the imprint substrate is at its fluid stage, during its solidifying process, and is at its final solid stage. As mentioned before, in practice, many different interactions all come into play, whether by design or by accident. Depending on the system and the conditions, it is possible that some undesired effects overshadow the interactions of interest, resulting in large uncertainty or even misleading trends. Therefore, it is necessary to understand all the details of every single step of a fabrication process in order to obtain repeatable results and to better control the quality of the products.

In step one − fabrication of the master − there are at least three possible ways to make the master: self assembly, photolithography and electron-beam lithography (EBL). One possible self-assembly method for making a master is to use a hexagonal close packed array of uniform micro- / nano-size spheres as mask for directional metal deposition [G. Zhang (2009)]. Most of the metal ions directionally deposited on the surface are stopped by the

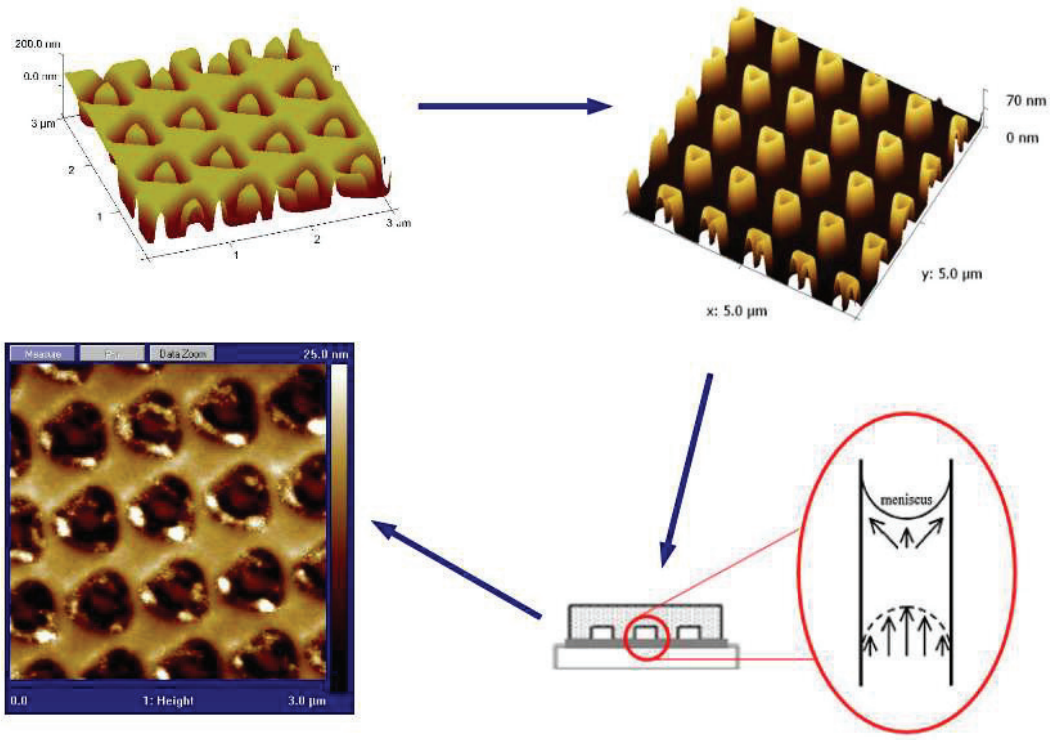

Figure 2.12. A representative four-step diagram for the CFL experiments.

spheres, the only ones that can land on the substrate underneath the assay are those that travel through the three-cornered voids in between every three spheres. After the spheres are lifted off from the substrate, only the near-triangular-shaped patches of metals remain. These regular metal patches can then be used as molding master directly or as an etching mask to make masters with higher aspect-ratios. As for photolithographic methods, one option is to make molding master or etching mask out of the photo-resist, and a second option is to use the structures made by photo-lithography as an etching mask or a deposition mask. EBL works in similar ways as photo-lithography in the sense that the two options mentioned previously are also available here with EBL. However, comparing to photo-lithography, EBL generally offers higher resolutions and is more adaptable. That is because, in principle, electron-beams have much shorter wavelengths than UV light, also, unlike photolithography which is essentially a pattern replication technique (although possible to reduce the feature size by using focusing optics), EBL is a mask-less fabrication technique which is capable of pattern generation. A photomask is required for photolithography. Photomasks with feature sizes larger than 20 μm can be printed by special ink-jet printers on transparencies. If the targeted resolution is smaller than 20 μm it usually requires a metal mask fabricated by EBL, e.g., a photomask with chromium patterns deposited on quartz glass. In research, the patterns or structures of interest need to be modified frequently, and EBL is better suitable for the prototyping tasks. In terms of wavelength, the mask-aligner we have access to uses 365 nm UV light source, and the EBL is usually performed at 20 $\sim$ 30 kV acceleration voltage, corresponding to 7 $\sim$ 9 pm wavelength. In this CFL project, EBL was chosen for master fabrication, where writing was performed on PMMA resist and followed by reactive ion etching (RIE).

EBL is one of the most flexible and powerful pattern generation techniques widely applied for nanoscale structure fabrication in research [Cumming (1996), Bilenberg (2006)]. Sub-10-nm feature resolution and sub-20-nm pitch have been demonstrated with EBL . The basic working principle of EBL is to use a very fine beam of electron as a "pen" to "write" on specially designed electron sensitive chemicals known as eBeam resists (**Figure 2.13 (a)**), and then transfer the patterns (via etching and/or deposition processes) onto materials with desirable structural, electrical, magnetic, chemical, biological, or material properties.

Because EBL is a serial process, the main limitation of EBL is its low throughput. An SEM can be modified to acquire eBeam writing capability by adding onto it an NPGS (Nanometer Pattern Generation System) module and (optionally) a beam-blinker. The NPGS can control the path of the electron beam precisely and produce the predefined exposure to every point within the writing area. Amongst the commercially available high resolution eBeam resists, PMMA and ZEP are two of the most popular positive resists (exposed regions are removed), and SU-8 and HSQ are two of the most popular negative resists (only exposed regions stay). Amongst the four options listed above, only PMMA and SU-8 are available in our CHM clean room. In EBL, the smallest feature size is much larger than the wavelength of the electron beam, and the resolution is mainly limited by the beam width (determined by the performance of the electron gun and the electron optics), the interaction between the electron beam and the resist and the electron beam and the substrate, and the response of the resist to electron exposure. Due to the aberrations (mainly chromatic and spherical, sometimes also astigmatism, the naming is analogous to light optics) of the electron optics, the electron beams used in SEM or EBL always have cross-sectional diameter larger than the wavelength of the electrons, known as the spot size, which is usually on the order of 1 nm. Moreover, even within the cross-section, the current density is not uniform − current density peaks at the center and continuously decreases towards the edge. The spot size of the electron beam determines the minimum spot size of EBL. As soon as the electrons enter the resist, they start interacting with the resist and being scattered. Scattering of electrons inside the resist layer results in the shape of the interaction volume deviating away from a cylinder and becoming a "tear drop", or effectively widening the electron beam. As the electrons get through the resist and enter the silicon substrate, they are scattered by the substrate and some of the resulting Auger electrons, secondary electrons, and photons can get to the resist layer and cause additional exposure. The feature widening due to electron scattering, both by the resist and the substrate, is known as the proximity effect. If the eBeam resist is chemically amplified, such as SU-8, where a low concentration of photoacid generator is mixed into the resist as catalyst for the crosslinking, the diffusion of the activated photoacid molecules can also cause widening of structures.

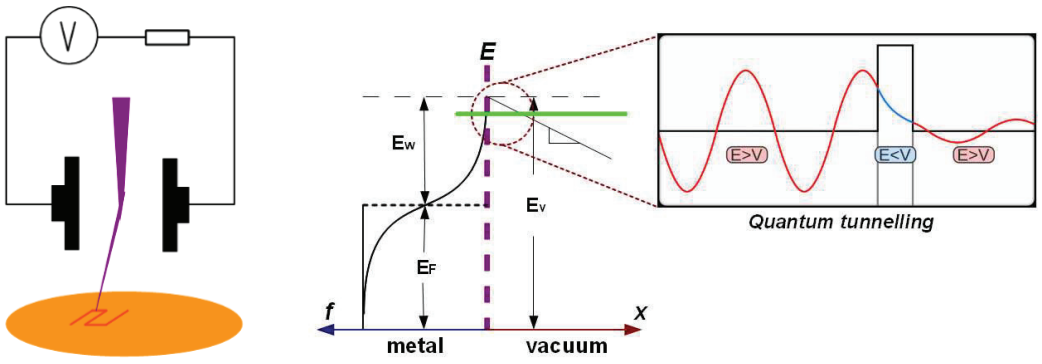

(a) (b)

Figure 2.13. Schematics of (a) the concept of using an electron beam to write on a eBeam resist, and (b) the working principle of a thermal field-emission electron source.

To get the highest resolution in EBL, it is helpful to understand some key factors in detail: (1) Substrate. The substrate for EBL usually needs to be a bulk semiconductor, such as a silicon wafer, or a thin film of conductor, such as a thin layer of gold deposited on a glass-slide. A bulk metallic substrate is seldom used in EBL, because the secondary-electron emission of a bulk metal is generally very high and thus would cause severe proximity effects under electron beam exposure. An insulator substrate is also not suitable for EBL because the local charging effect would deflect the incident beam and affect the quality of lithography, unless a thin conducting film is deposited on top of the substrate or the resist to drain the excessive charges to ground. In our experiments silicon wafer is the choice of substrate because they are widely available. Surface treatments can be done on silicon wafers, such as growing a thin layer of SiO_2 or Si_3N_4, if specific secondary-electron properties or RIE properties are needed. A thin layer of SiO_2 on the surface of the silicon wafer can reduce the generation of secondary electrons and thus reduce the proximity effect. A thin layer of SiO_2 or Si_3N_4 can also be used for a selective RIE procedure which stops relatively accurately at the depth of the SiO_2−Si interface. (2) Resist. In our experiments we used both PMMA (as positive resist, used in the CFL project) and SU-8 (as negative resist, used in the SHS project, **Chapter 3**). PMMA molecules that are exposed to a proper dosage of electron will be broken into lower molecular-weight sections which can

then be dissolved and removed by a weak solvent while the unexposed region stay intact. Since PMMA has poor etching resistance, it is generally not a good idea to use the eBeam writing product directly as etching mask, but instead to use it as mask for metal deposition. In this case, undercuts are helpful for ensuring that the metal film deposited on top of the resist is completely separated from the regions that are deposited through the openings in the resist film onto the substrate surface, because that can product better lift-off results. To increase undercuts, a bilayer resist consists of a PMMA layer on top of an MMA-MAA layer was used. The MMA-MAA layer is sensitive to the secondary-electrons generated by the interactions of the primary beam and the silicon substrate and to the developer, as a result it can product large undercuts. The way to achieve this bilayer resist structure is to do two spin-coatings, first coat an MMA layer and then coat a PMMA on top. Spin-coating is a thin film coating technique where a solution of the coating materials is deposited, spun, and dried on the substrate surface to produce a thin, uniform, and flat coating film. Thin films produced by spin-coating are usually with thickness range from tens of nanometers to tens of microns and surface roughness on the order of 1% the thickness. A soft bake procedure usually follows the spin-coating to reduce the solvent content down to the level where required adhesion and structural strength can be achieved. The temperature and duration of soft bake mainly depend on the material composition and thickness of the resist film. In this process, the spin speed is the most significant determining factor of the thickness of the product film. Nonetheless, reproducibility of the results also depends on the cleanness and wetting properties of the wafer surface, the initial spreading of the coating fluid when deposited on the wafer, and the consistency of the temperature and air convection conditions during the coating and baking process. The cleanness (whether there are particles or alien chemicals on the surface) and flatness of the substrate are also key in dictating the quality of the coating. For this reason, in the two-step coating procedure it is critical to completely dry and cooled before the application of the solution for the second layer. This can minimize the effect of the second solution partially dissolves the first coating. (3) eBeam writing. When PMMA is used, the structure on the resist is used as a deposition mask. In this case the structure should be reversed with respect to the desired structure on the master because the deposition step will reverse it back. For example, to

make capillaries with triangular cross-sections on the PDMS mold, a master with triangular cylinders is required, and thus triangular cavities with well-defined top opening and undercut should be made on the eBeam resist. To minimize the corner rounding and get the best resolution out of EBL on our SEM-NPGS system, a high acceleration voltage, a low beam current, and most importantly, a good beam alignment are beneficial. Our SEM is a thermal field-emission SEM (**Figure 2.13 (b)**) in which free electrons are generated by the combined effect of thermal excitation (which dictate the energy spread of the electrons near the Fermi level) and quantum tunneling (which is controlled by the voltage gradient or, equivalently, the electric field strength). A lower current corresponds to a narrower spreading of energy distribution of the electrons generated by the electron gun, which in turn reduces the chromatic aberration. A higher acceleration voltage gives a smaller beam diameter and produces smaller beam widening when going through the resist, both of which are due to the higher forward momentum. At the same time, increasing AV also increases the penetration depth of the electrons and stretches the entire interaction region down into the substrate. This reduces the secondary-electron production (because the secondary electrons have to escape from a greater depth), which would reduce the undercut of the EBL product. A higher dosage can offset this disadvantage, also the amount of undercut varies with the thicknesses of each of the bilayer resist. (4) Deposition and etching. In order to get the best resolution on this step, directional deposition techniques are preferable. For metals, e-Beam evaporation provides high level of directionality and control over thickness. Gold is often deposited and used as etching mask for the next step because it is one of the most chemically inert metals, and a 5 nm layer of titanium is usually used as an adhesion layer between the deposited gold and the silicon dioxide surface.

Shown in **Figure 2.14** and **Figure 2.15** are some representative SEM and AFM images, respectively, of the structures made on a master as products of step one. **Figure 2.14** can be divided into three pairs of images: (a) and (b), (c) and (d), (e) and (f), each pair represents one sample. **Figure 2.14** (a) and (b) are 300 nm triangles made with EBL on SU-8 without etching. They show well-defined shapes and sharp corners, but as a trade-off, the aspect-ratios are relatively low. **Figure 2.14** (c) and (d) are 100 nm and 200 nm triangles, four-stars, and posts made with EBL on bilayer PMMA, followed by gold deposition and

life-off, and then RIE etching. They also show well-defined shapes and sharp corners, and moderate aspect-ratios, but the three-dimensional profile was not uniform after etching, i.e., the sidewalls were not smooth. **Figure 2.14** (e) and (f) are four-stars made with EBL on PMMA and directly followed by RIE etching without deposition. They shown severely rounded corner. The depth of the structures were not determined. **Figure 2.15** are two samples made by EBL on PMMA, (a) is the master after RIE etching into Si_3N_4, (b) is on PMMA without etching. **Figure 2.14** (a), (b), (c), (d), and **Figure 2.15** (a), (b) were designed to be a molding master, so the EBL structures were the negative of what was expected to form on the PDMS mold. **Figure 2.14** (e) and (f) were designed to be the imprinting mold, so the EBL structures functioned as capillaries. In CFL or soft lithography in general, an important requirement is that one of the two components in contact needs to be flexible in order to enable separation after the imprinting. In this case the mold is silicon, so the imprinted substrate has to be soft material such as PDMS.

Step two is mounding of PDMS. It is a relatively simple and well-established technique to create replicas of micro- / nano-structures by crosslinking of PDMS. This procedure involves casting a liquid mixture of polymer PDMS and crosslinking agent onto a structured master and then carefully separate them after the liquid turns into a rubber-like elastic network. The important properties of a PDMS mold are the bulk elasticity and the fidelity of the micro-/nano-structures on the surface. On one hand, the PDMS mold needs to be "soft", which is one of the most important ideas of soft lithography. The bulk elastic modulus of the PDMS stamp should be relatively low so that bending, stretching, and compressing of the stamp are relatively easy. This can ensure conformal contact between the stamp and the substrate to start the imprinting, as well as enable the separation after the imprinting. If both the stamp and the substrate are rigid, it would be extremely difficult to separation them without damaging the imprinted structures, just because the entire contact interface has to be destroyed all at once which costs a large amount of energy. An elastic stamp also allows small amount of deformation so that even if there are dusts or other small particles (such as residuals from any previous processes) left on the surface, a reasonably well contact between the stamp and the imprinted layer can still be established. However, the mold should not be too soft, otherwise the micro-/nano-structures on the surface would

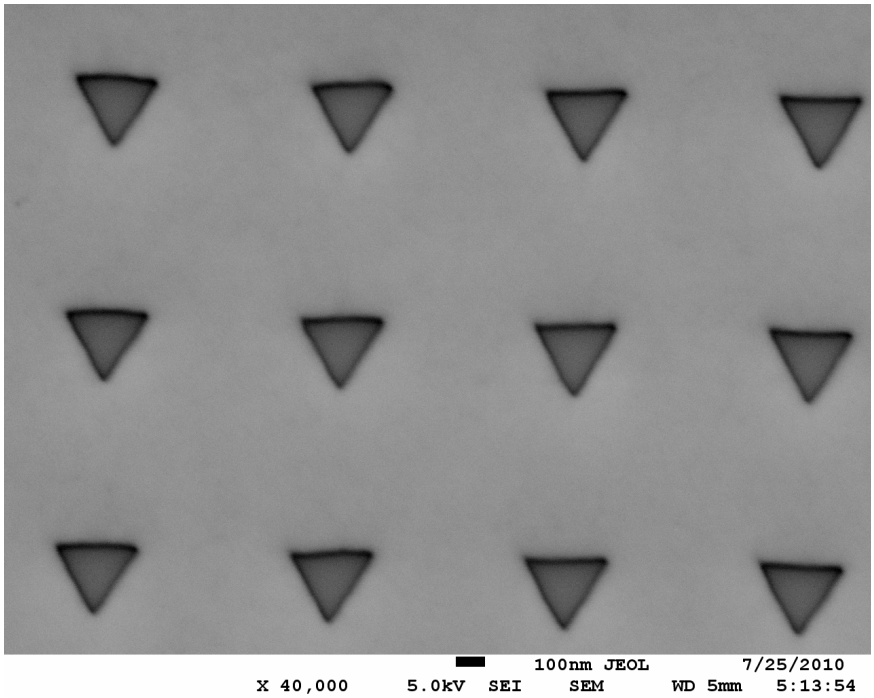
100nm JEOL 7/25/2010
X 40,000 5.0kV SEI SEM WD 5mm 5:13:54

(a)

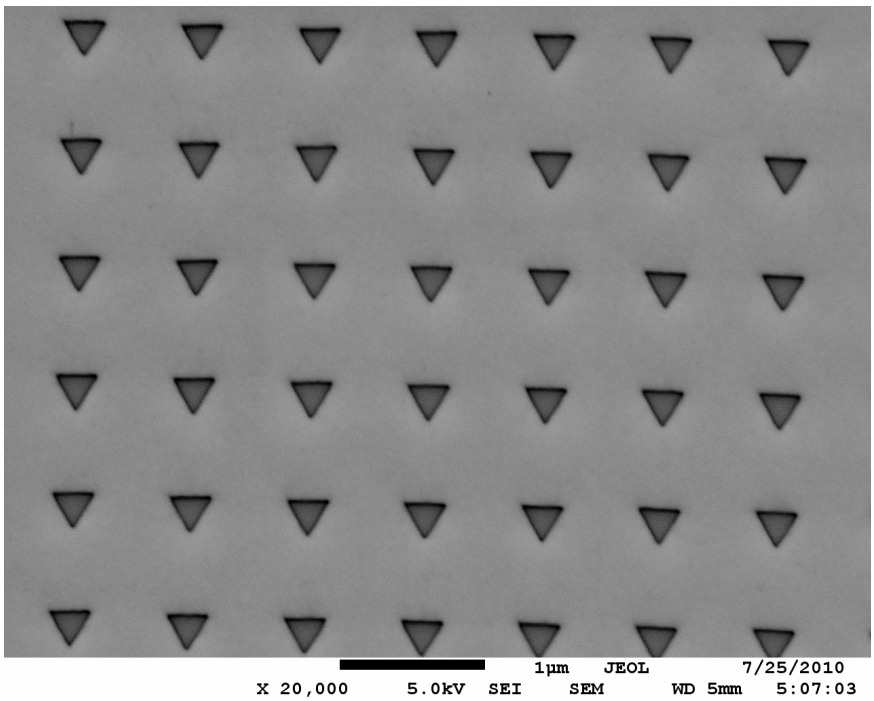
1µm JEOL 7/25/2010
X 20,000 5.0kV SEI SEM WD 5mm 5:07:03

(b)

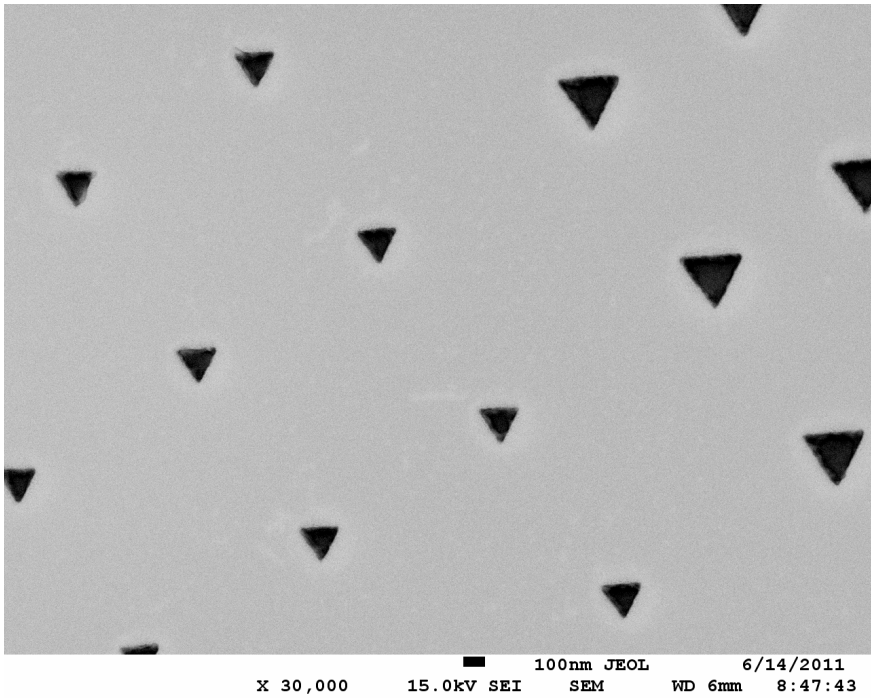
100nm JEOL 6/14/2011
X 30,000 15.0kV SEI SEM WD 6mm 8:47:43

(c)

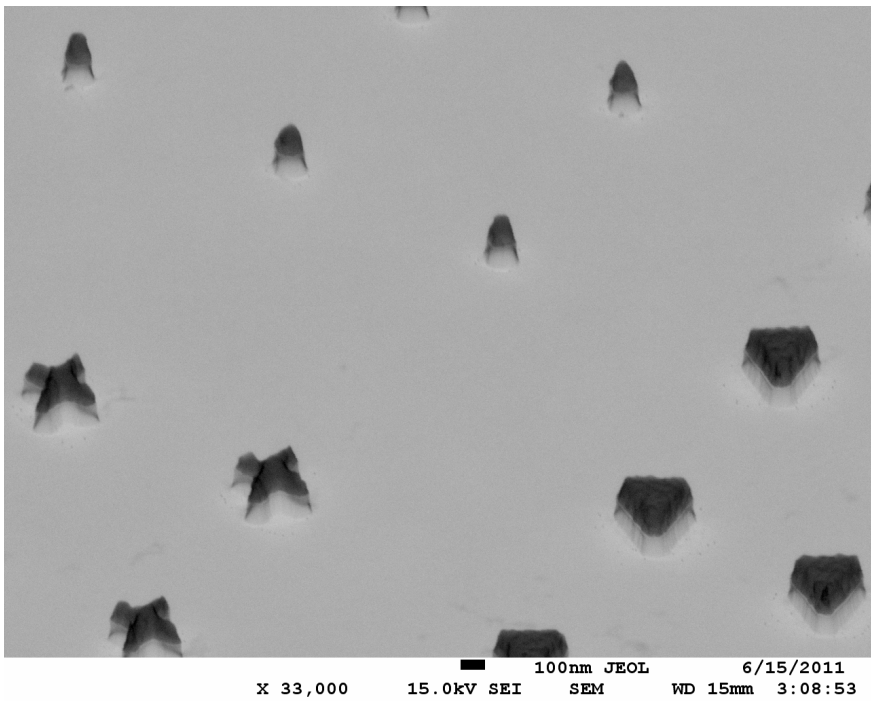
100nm JEOL 6/15/2011
X 33,000 15.0kV SEI SEM WD 15mm 3:08:53

(d)

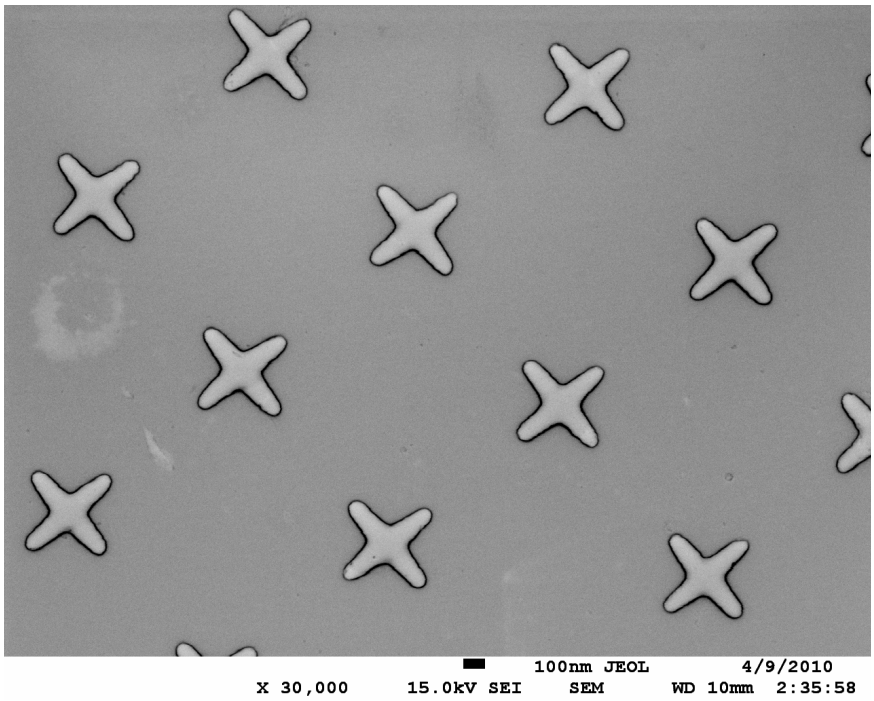

(e)

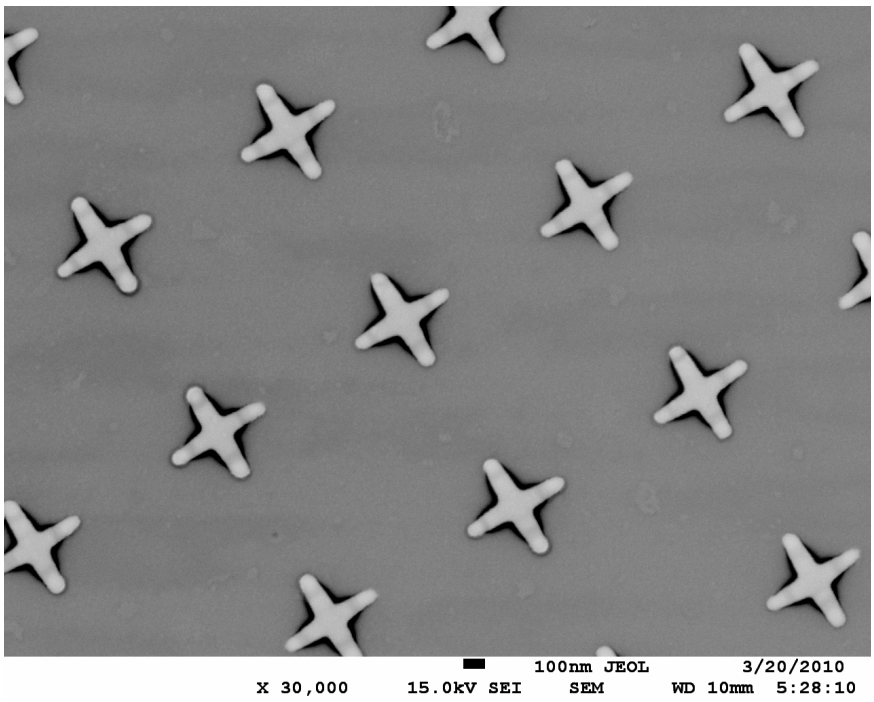

(f)

Figure 2.14. Representative SEM images of the structures fabricated on the master. All images except (d) are top view. (d) was taken at a 30° angle to show the three-dimensional structures.

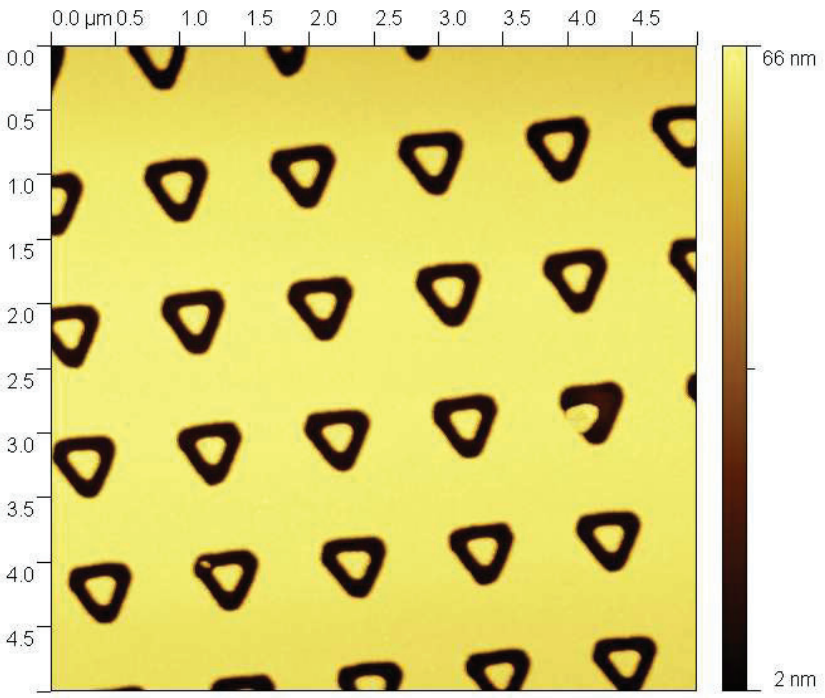

(a)

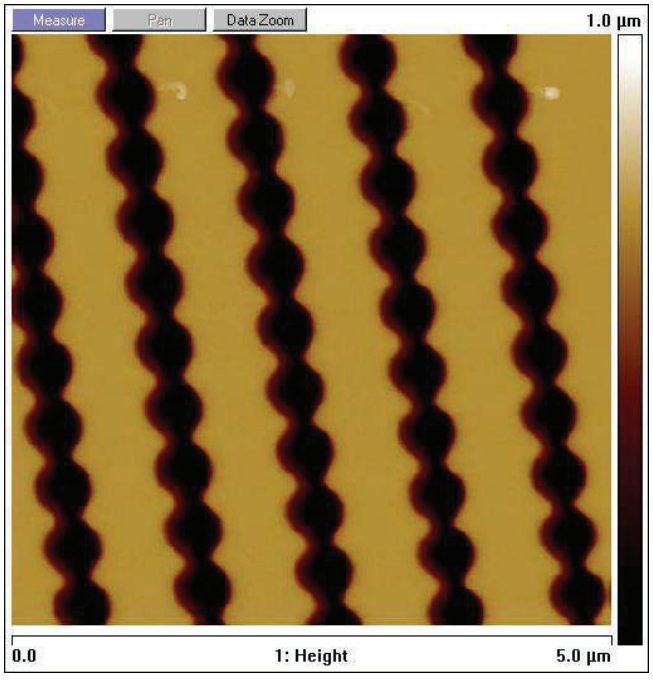

(b)

Figure 2.15. Representative AFM images of the structures fabricated on the master.

very likely be deformed due to surface tension effects. It has been shown that, by using a composite stamp, bulk elasticity and surface stiffness can be achieved at the same time. The idea is to make a PDMS mold which consists of two layers that are chemically bonded together: a thin stiff layer of modulated PDMS on the patterned surface, and a thick elastic layer of ordinary PDMS as bulk. Experimentally, a small amount of the formulation for the stiff PDMS will be first spin-coated on the pattern master. The master with the thin coating will then be heated up slightly for a short amount of time to have the stiff PDMS layer partially cross-linked. Then, while the thin PDMS layer is still wet, the mixture for ordinary PDMS will be poured on top of the thin layer, and the system will be heated up to completely cross-link both layers of PDMS. The stiff layer of modulated PDMS offers high local structural strength to maintain the fidelity of the micro-/nano-structures, but at the same time because it is very thin, its global bending modulus is low enough that separation of the stamp and the substrate is still possible. The thick elastic PDMS layer serves the purposes of providing structural support as well as absorbing and distributing externally applied stress. When using the composite stamp in thermal imprinting (where the imprinted substrate, usually a thermal plastic, needed to be heated up to above its glass-transition temperature when it is in contact with the mold), it is also important to consider the difference in thermal expansion behavior between the two layers, in order to avoid or counteract the internal stresses and spontaneous deformations built up at elevated temperatures. For example, a rigid planner back-plate might be used to keep the PDMS stamp from buckling. Besides the elastic properties, another key aspect of the PDMS stamp is its surface tension. There are well-established silanization methods for modifying the surface chemistry of PDMS to tune the surface energy and wettability of the PDMS. Some representative AFM images of the PDMS mold are shown in **Figure 2.16**.

Step three is imprinting. There are at least three options to do the imprinting using a PDMS stamp: (1) imprint into a thermoplastics when heated above the glass-transition temperature; (2) imprint into a solution and then dry out the solvent by evaporation; (3) imprint into a photo-sensitive fluid and then cross-link the resist with UV light. One of the most important goal of this project is to obtain hierarchical structures, which requires that the imprinted fluid wets the mold ($\theta < 90^\circ$) and the cavities on the PDMS mold

are partially filled. Those requirements, though seem to be simple, can lead to a number of complications. First, surface tension is, in most cases, a function of temperature and composition. Therefore, if a thermoplastic material is used, it is important to recognize the possibilities that the mold may deform at elevated temperatures or by absorbing solvent, and that the CA between the mold and the imprinted materials may change drastically during the cool down process especially if phase transitions are involved. Similarly, if a solution is used, the change of CA with the reduction of solvent concentration needs to be considered. Second, since gravity is negligible and Laplace pressure is generally very large at small scales (high curvatures), to achieve partial filling of a wetting fluid into cavities on the mold, a volume constraint is critical, which means an ultra-thin film of imprinted material is required. The maximum thickness of this film depends on the the depth and the density of the features. The deeper and denser the features are, the thicker the imprinted film can be. In reality, it can be very difficult to ensure the cross-section of the features on the mold stay the same on the depth direction, and the thin film do not dewet from the substrate surface during the imprinting process. Third, because the fluid is required to wet the mold, which means the fluid-solid interface has relatively low energy comparing to a solid-air interface, after imprinting it will be difficult to separate the mold from the imprinted material while keeping the imprinted structures intact. This problem can be fixed by using a sacrificial mode such as a soluble polymer, but this will be rather inefficient because mold fabrication is generally costly.

In **Figures 2.14**, **Figures 2.15**, **Figures 2.16**, we have demonstrated the quality and diversity of nano-structures can be produced by our method. Using these structures, some case-studies of CFL experiments were performed. The main goals of these cases studies were to qualitatively demonstrate the viability of adding on three-dimensional features with surface-tension effects.

Case study #1: triangular capillaries. A brief recap of the whole procedure: (1) Perform EBL to produce negative structures on PMMA. (2) Perform RIE to transfer the EBL pattern onto the Si_3N_4 layer. (3) Perform soft molding to make composite PDMS molds for imprinting. (4) Perform silanization to enhance the wettability of PDMS. (5) Perform CFL onto a thin film of polystyrene (Mw = 280,000, from Sigma Aldrich) coated on silicon

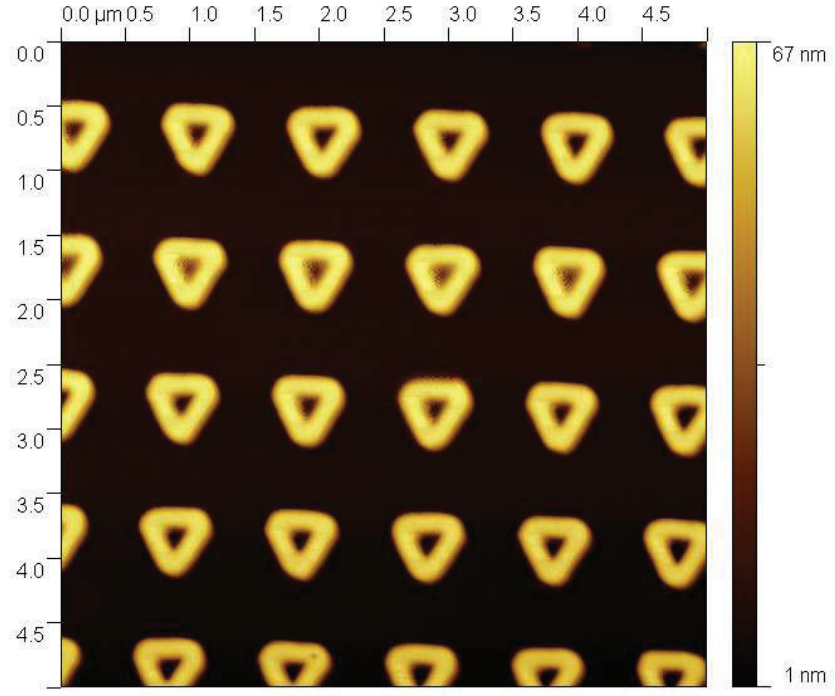

(a)

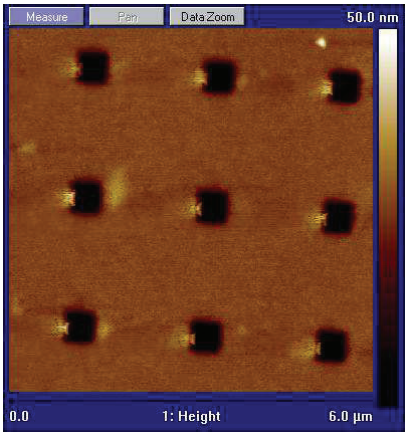

(b)

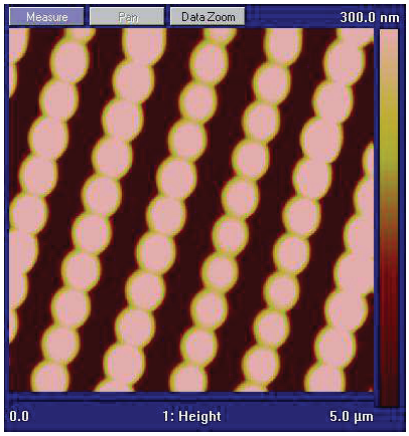

(c)

Figure 2.16. Representative AFM images of structures on the PDMS mold.

wafer prior to the CFL. This procedure is shown in **Figure 2.12**. Some relevant structures are also shown in **Figure 2.15 (a)** and **Figure 2.16 (a)**. Representative AFM images of the structures on the CFL products are shown in **Figure 2.17**. On these images, the triangular structures can be identified. The highest points are at the corners of the triangles − a location predicted by the simulation studies presented previously. These images provide direct evidence that additional features can be formed as a result of capillarity. The fact that not all the corners corresponded to high peaks was likely due to the damaging of structures during mold separation. As explained by the simulation results, to achieve large elevations, a high wettability, or a low contact angle, was desired, but that also led to substantial adhesion between the mold and the imprinted structures. During mold separation, nano-features with high aspect-ratios and insufficient structural strength could be teared off, leaving only a crater. Even for the remaining high points, it is uncertain whether the initial structures might have collapsed to the side or might have been partially cut off (so only the bottom portion is remaining). Based on the information displayed on the AFM image, the elevations of different peaks varies between 8 nm to 15 nm, which is relatively low comparing to the linear size of the triangle. The height contrasts between the highest and lowest point in a single structure are up to 25 nm. However, the shape of the meniscus is not bowl-like, because the center is not the lowest point of the structure. This case study shows that the underlining physical mechanism explained previously by the simulations is valid, but limitations of materials properties of the elastic mold and the imprinted polymer prevent exact matching between the experimental results and the predictions based on simulations.

Case study #2: four-armed star capillaries. A brief recap of the whole procedure: (1) Perform EBL to produce positive structures on PMMA. (2) Perform RIE to transfer the EBL. (3) Perform CFL onto a thin PMMA (Mw = 950,000, from MicroChem) film (coated on a PDMS stamp prior to the CFL). This was the case where the mold was "hard" and the imprinted substrate was "soft". Some relevant structures are also shown in **Figure 2.14** (e) and (f). Representative SEM images of the structures on the CFL products are shown in **Figure 2.18**. A thin layer of gold was sputtered on the surface before SEM imaging. **Figure 2.18** were taken from a 30° tilting angle to allow for direct observations of elevation. On these two images, it is clear that PMMA aggregated at the corners, which

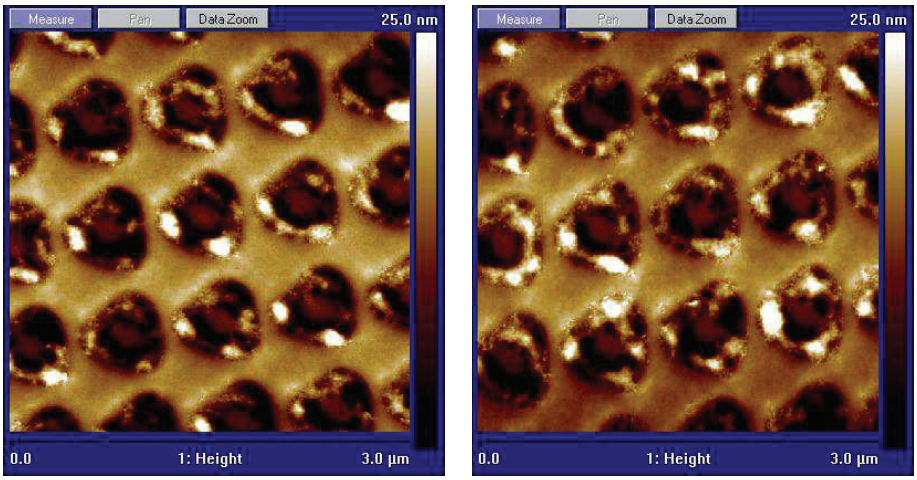

(a) (b)

Figure 2.17. Representative AFM images of structures formed by CFL performed with triangular capillaries.

agrees qualitatively with the predictions. The exact feature depths on the mold and the feature elevations of the imprinted products were not determined. However, the feature depth on the silicon mold was expected to be relatively small due to the very limited power of the reactive-ion etcher and the low etching resistance of PMMA Moreover, the contact angle between etched silicon and the imprinted material, PMMA, was close to 80°, which based on simulation results could not result in high values of elevations.

2.5 Conclusions of the CFL project

In this chapter, we have summarized our attempts, using both computational and experimental tools, to understand and utilize surface-tension effects to enhance the capability of CFL. First, simulation results were presented which demonstrated that high aspect ratio three-dimensional nano-structures can be achieved by CFL with proper choice of cross-section geometries. This conclusion was obtained after studying the menisci formed in a series of capillaries with different cross-sectional geometries, including regular polygons and star-shapes with both sharp and rounded corners. For sharp corner polygons and stars, the simulation results were shown to match the analytical solutions for elevation of the

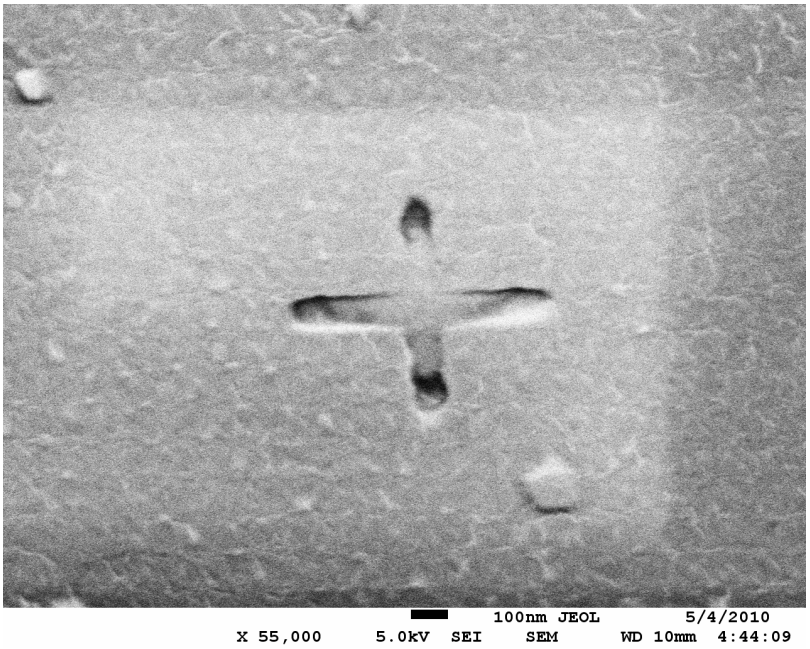

(a)

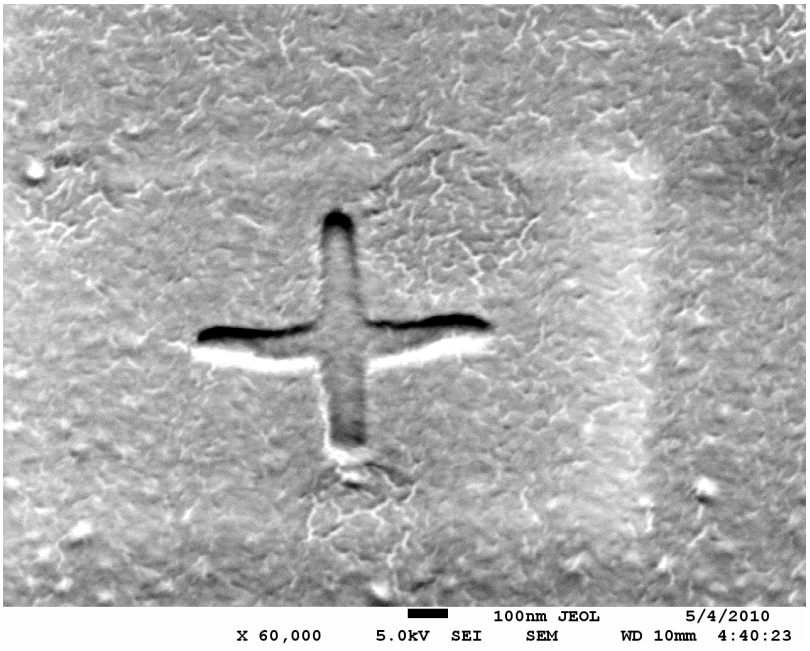

(b)

Figure 2.18. Representative SEM images of structures formed by CFL performed with four-armed star-shape capillaries (by design) with severely rounded corners. Structures were formed on PMMA. SEM images were taken at a 30° angle (from vertical).

meniscus, demonstrating the accuracy of the simulations. It was shown that, as far as the elevation and the shape of the meniscus are concerned, altering the cross-sectional geometry from a circle to a regular polygon or to a regular star is effectively equivalent to simply changing the contact angle between the fluid and the capillary wall. Numerical solutions for elevation of the meniscus formed in rounded corner polygons and stars cross sections were calculated based on simulation results. The rounding of corners was found to cause significant reduction in elevation by not only cutting off a portion of the peak but also modifying the shape of the meniscus near the corners. At a given contact angle, elevation decreased as rounding radius increased, following clear power laws within the regime of rounding radius between 10 nm and 30 nm. The specific power indices, ranged from -0.3 to -0.4 for triangular cross sections, and from -0.7 to -1.1 for three-armed star-shaped cross sections, varied with contact angle, and degree of corner rounding (outside the range of 10 nm and 30 nm of rounding radius). The sharp-corner cases are good starting point for understanding the effects of different parameters on the equilibrium meniscus, while the rounded-corner cases capture a rather important practical aspect in CFL experiments; namely the inability to fabricate perfectly sharp corners at the nanometer length scales. It is shown in this computational study that even with moderate corner rounding, large elevations on the meniscus can still be achieved especially when using star-shaped capillaries. Second, experimental results were presented to successfully demonstrate the underlining working principle that allows for additional structures to form based on surface tension effects. Hierarchical structures that exhibit finer features than the initial imprinting mold were obtained in two separate case studies. Although limited by material properties of the mold and the imprinted polymer, clear evidence of qualitative agreements between the results of simulation and of experiment were identified. The findings of this study can serve as guide to improve the design and understand of imprint-lithographic processes. In the future, if new materials are developed that has the desired properties (i.e., high structural strength down to the nano-scale, and high wetting abilities at liquid state but low adhesion at solid state), we are confident that this scheme can be applied to practical productions. For now, in order to produce high aspect-ratio hierarchical structures so that we can study

their wetting properties, we turn to other fabrication techniques such as Electron-Beam Lithography, which we will discuss in **Chapter 3**.

CHAPTER 3

HIERARCHICAL STRUCTURES ON SUPERHYDROPHOBIC SURFACES

Hierarchical structures observed in nature have inspired scientific and engineering advances in fields such as hydrodynamics, surface physics, and material science [Munch (2008), Koch (2009) (a) (b), W. Zhao (2010), Watson (2010), Barthlott (2010)]. In recent literature, a broad range of interesting properties have been attributed to hierarchical surfaces including reversible adhesion [Boesel (2010), Greiner (2009)], controllable wettability [X. J. Feng (2006), F. Zhang (2007), Y. Xiu (2008), J. Wu (2010)], and enhanced optoelectromagnetic activity [S. J. Choi (2010), Sauvage (2010), H. Wu (2010)]. One particular class of hierarchical surfaces, superhydrophobic surfaces (SHS), have drawn significant attentions due to their self-cleaning and drag-reducing capabilities [Bhushan(2011), L. Lin (2010), X. Yao (2010) (a), Bhushan (2009)]. SHSs are surfaces with very high water contact angles (CAs), typically greater than 150°. Previous studies based on artificial hierarchical SHSs have revealed the importance of the secondary structures on the overall wetting properties of the surfaces. These secondary structures have been shown to enhance the contact-angle (CA), reduce the CA-hysteresis, and improve the stability and robustness of superhydrophobic states [Gao (2006) (c), Y. Xiu (2006), X. Yao (2010) (b), A. H. F. Wu (2010), Shieh (2010)].

A number of methods have been reported for producing artificial hierarchical structures on a surface, including molding and imprinting [W. Zhao (2010), F. Zhang (2007), S. J. Choi (2010)], chemical etching [X. Yao (2010) (a), Y. Xiu (2008), Y. Xiu (2010)], reactive-ion etching [Y. Kwon (2009), R. Xiao (2009)], self-assembly [Y. Xiu (2006), Byun (2009), W. Han (2011), H. Yang (2010)], deposition [K. Koch (2009) (b)], hydrothermal synthesis [J. Wu (2010)], template guided gelation [L. Lin (2010)], photolithography [Greiner (2009), Boesel (2010)], growth of nanowires [Ko (2010)], electric-field-assisted soft lithography [Morariu

(2003)], laser-assisted etching [Baldacchini (2006)] and ultrasonically assisted synthesis [H. Chen (2009)]. However, the majority of these hierarchical surfaces are decorated with random secondary structures, and thus only statistical conclusions can be drawn. These random secondary structures can sometimes vary significantly in size, orientation, and distribution, making it difficult to fully characterize the secondary structures and to correlate the details of these structures and the overall properties of hierarchical surfaces. In order to better understand the role of the secondary features, here we introduce a novel technique for fabricating hierarchical surfaces with both well-defined primary structures and regular secondary structures by electron-beam-lithography (EBL or e-Beam). Using this technique, multiple geometric parameters including size, spacing, and shape of both the primary and the secondary structures can be designed precisely and relatively independently. Moreover, we believe that the ability to fabricate macroscopic devices with well-defined hierarchical structures and at the same time maintain a very high level of control over the finest details of the structures will also be quite useful in many other important fields.

3.1 Introductions to Superhydrophobic Surfaces

Superhydrophobicity generally requires the combination of material hydrophobicity and surface roughness. Material hydrophobicity refers to a water contact angle (CA) greater than 90°, which indicates that the energy cost to form a unit area of water-solid interface is larger than that to form a unit area of solid-air interface, or simply put, the solid surface likes to be in contact with air more than it does to be in contact with water. Surface roughness generally augments the material hydrophobicity by increasing the area of the solid surface as a result of adding on local curvatures. The amount of additional surface area depends on the surface profile, most importantly the aspect-ratio of the surface structures. As long as the two-dimensional profiles are similar (same geometric shape scales up or down), the amount of added area on a rough surface is completely insensitive to the characteristic length scale. However, surface area is not the only factor. On a rough hydrophobic surface, it costs a substantial amount of interfacial energy for water to make conformal contact with the surface, so a lot of times, the liquid-solid contact is actually not conformal. In those cases, wetting dynamics is of great importance. When a droplet of water rests on a homogeneous

SHS with single-level roughness, there are two basic wetting states: the Wenzel state and the Cassie state. In the Wenzel state, the droplet is in intimate contact with the surface, so the actual contact area is larger than the projected area, and the ratio between these two areas is determined by the roughness of the surface. In the Cassie state, the droplet is suspended at the tops of the microscopic surface structures but does not touch the base of those structures, so the actual contact area can be smaller than the projected area, and the ratio between these two areas is determined by the shape and distribution of the structures on the surface.

A simplified model can be used to investigate the energy landscape of a single-roughness SHS. As shown in **Figure 3.1**, water is in contact with an array of cylindrical pillars (only one is shown) with either vertical sidewalls (left) or sloped sidewalls (right). As the water level (blue line) moves downward from the top of a pillar, a portion (light gray) of the sidewall is covered by water. For this to spontaneously happen in the vertical sidewall case, the contact-angle θ_1 has to be less than 90° This is equivalent to requiring $\gamma_{SV} > \gamma_{SL}$ from the energy point of view, because a portion of the solid-air interface is replaced by the same area of solid-liquid interface as the water level moves down. By definition, if the material is hydrophobic, then this condition can not be satisfied. In the sloped sidewall case, assuming the slope angle (measured from the bottom) is α, the range of contact angle for spontaneous wetting, based on contact angle dynamics, is $\theta_2 < \pi - \alpha$, which can be larger than 90°. The exact same result can also be obtained by energy calculation based on a three-dimensional structure (cylindrical symmetry). The reason why it is easier for water to wet a conical pillar is that as the water level goes down, the liquid-air interface shrinks which reduces surface energy.

A number of natural SHSs exhibit structural hierarchy. For example, close examinations by SEM reveals a landscape covered with complex two-tiered hierarchical structures on the surface of a lotus leaf, as shown in **Figure 3.2 (a)**. Recent studies have revealed that the structural hierarchy on an SHS plays a significant role in determining their wetting properties. To enhance hydrophobicity, the advantages for having hierarchical structures over single-length-scale structures is not only that the surface area has increased, but also the wetting dynamics has changed. First, the increase in surface area is easy to see because the

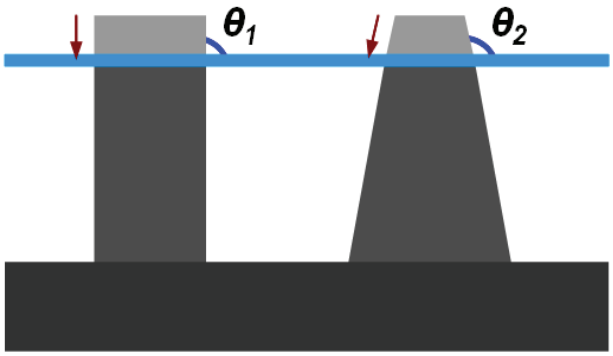

Figure 3.1. Schematics of a cylindrical (left) and a conical (right) pillar wet by water from above.

structures are more fractal-like. More importantly, the existence of the secondary features (assuming the wetting of the secondary features is at Cassie state) can result in only partial coverage of the tops of the primary features (**Figure 3.2 (b)**). This is especially important for the release process, because, as long as the material CA is less than 180°, it always takes energy to separate a liquid and a solid in contact. The energy for separation of a unit area is W_{SL}, so the total energy for separation is proportional to contact area.

In some cases of hierarchical SHS, it is possible to have a system to be at a partial Wenzel state. There are two possibilities as shown in **Figure 3.3**: (a) The liquid-solid interface extends to the bottom of the primary structure, but remains only at the tops of the secondary structure. We refer to this as the type-I partial Wenzel state (tI-PWS). (b) The liquid-solid interface covers the entire top of the primary structure, but does not reach the bottom. We refer to this as the type-II partial Wenzel state (tII-PWS). In the scope of this thesis, liquid penetration into the cavities of micro- or nano-structures can be due to any one of or any combinations of the following three factors: (a) hydrostatic pressure due to gravity, (b) hydrodynamic pressure due to impact, and (C) slope of the sidewall. Because bigger dimensions generally correspond to lower curvatures, it is straightforward to see how tI-PWS can be caused by hydrostatic or hydrodynamic pressure. For example, based on the estimations presented in section 1.4 of **Chapter 1**, a raindrop could potentially end up at tI-PWS due to its high impact velocity. A tII-PWS can happen when the sidewall

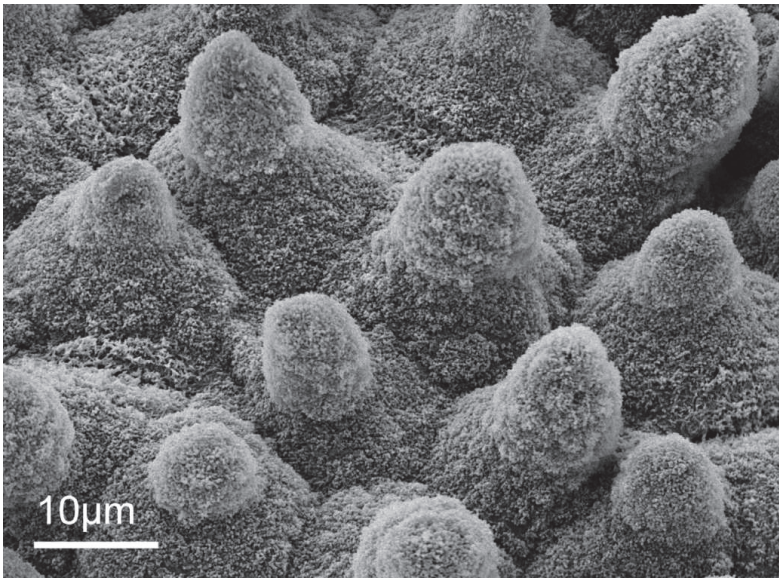

(a)

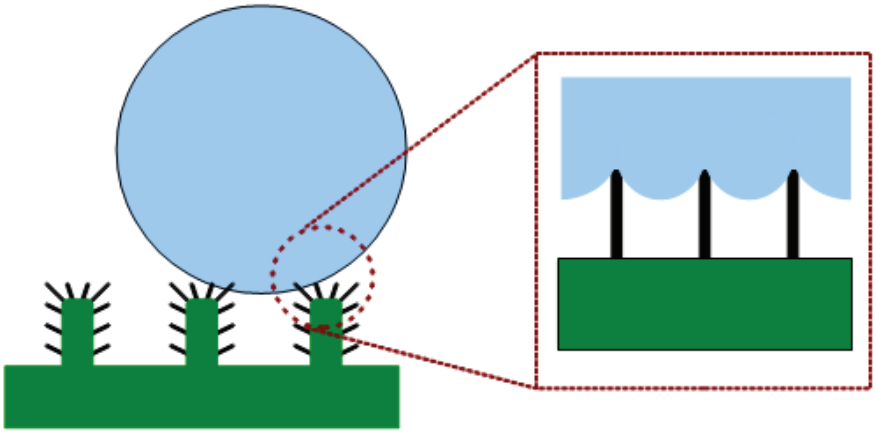

(b)

Figure 3.2. Structural hierarchy and the Lotus effect. (a) An SEM image of a lotus leaf surface reveals hierarchical structures. (b) Schematics of the lotus effect enabled by the hierarchical structure.

(a) (b)

Figure 3.3. Schematics of two different scenarios of partial Wenzel state: (a) type-I: only primary features are penetrated, and (b) type-II: only secondary features are penetrated.

slope of the $\theta_2 < \pi - \alpha$ secondary features is lower than that of the primary feature, such that condition is satisfied by the secondary features but not by the primary features. Both types of partial Wenzel states are likely to exhibit a high advancing contact angle and a low receding contact angle, or, in other words, high hysteresis, due to the pinning of contact line.

3.2 Fabrications of Hierarchical Superhydrophobic Surfaces

We are most interested in exploring the functionality of the secondary features of a hierarchical SHS, and one of our goals in the fabrication step was to produce well-defined secondary features, so we used EBL to produce both the primary and the secondary structures. We call this method the dual-scale EBL. Among current lithographic techniques, EBL offers one of the best combination of precision and versatility [Bilenberg (2006), Q. Xiao (2008), Koller (2009)], yet the utilization of EBL in fabricating macroscopic devices is often largely hindered by its limited throughput. Theoretically, EBL has a fundamental advantage over photolithography due to the lower diffraction limit characterized by the Abbe's equation: $d = 0.612\lambda/NA$, where d is the resolution, λ is the wavelength, NA is the numerical aperture. Ultraviolet (UV) light usually has a wavelength range of 100 nm $\sim$ 400 nm (although the wavelength of extreme-UV, or EUV, can go down to 10 nm), while for a high energy electron, the de Broglie wavelength (taken into account the relativistic effects)

is $\lambda = h_{Pk}/p = h_{Pk}/\left(m_o c\sqrt{\xi^2 - 1}\right)$, where h_{Pk} is the Planck constant, mo is the electron mass at rest, c is the speed of light, and ξ is the Lorentz factor. For a 30.0 keV electron, the de Broglie wavelength is about 8.59 pm (picometer). In practice, the resolution (or smallest feature size) achievable by EBL is mainly depend on the beam width (aberrations of the electron optics) and responses of the resist. For our FE-SEM system, the smallest features I have been able to obtain are shown in **Figure 3.4**.

As mentioned previously, the basic idea of EBL is generating patterns by scanning an extremely narrow beam of electron on a photoresist in a carefully controlled fashion, and it usually takes a long time for a nanometer-wide beam to write enough pattern that covers an area of a few millimeter-squared. This limitation can be significantly reduced, if EBL is done on a more sensitive resist, such as SU-8, due to the drastic reduction of exposure dosage required [Salerno (2007)]. SU-8 is well known as a high-performance photoresist for UV lithography, and is also very sensitive to electron beam exposure [del Campo (2007), Lpez-Romero (2010)]. Each SU-8 molecule has eight epoxy groups that can serve as potential cross-linking sites. Moreover, commercial SU-8 is chemically amplified to improve sensitivity by mixing in a small amount of photoacid generator, which will turn into acid catalyst upon exposure to UV light or secondary electrons. These acid molecules will catalysis the cross-linking reactions of the epoxy groups at elevated temperatures. From experiments we have found out that, when SU-8 is used in EBL, the fabrication time per device is rather reasonable. For a typical 2 mm $\times$ 2 mm hierarchical surface, the total e-Beam time which includes both time for electron beam exposure and stage movement is between 20 and 35 minutes.

Two types of hierarchical structures consisting of macroscopic arrays of well-defined micron-sized blocks and well-ordered nano-scale posts or ridges were fabricated on SU-8. The first type consisted of nano-scale posts covering only the top surfaces of the micron-sized blocks. The second type consisted of nano-scale posts or ridges covering both the top and the side surfaces of the micron-sized blocks, as well as the valleys between adjacent blocks. Correspondingly, two different fabrication techniques were investigated for imparting dual-scale structures to the desired surfaces: single and double EBL-exposure.

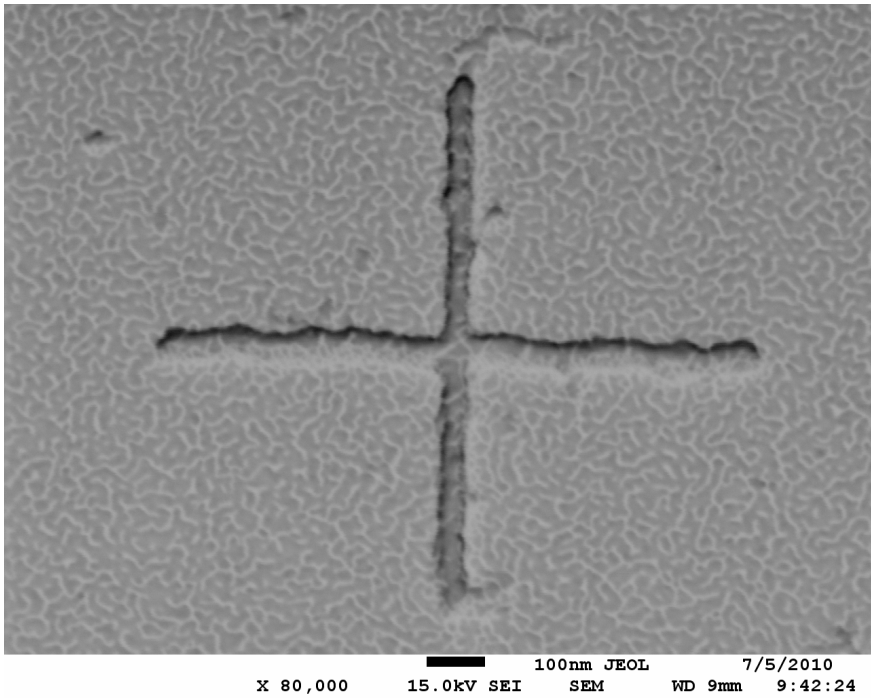
100nm JEOL 7/5/2010
X 80,000 15.0kV SEI SEM WD 9mm 9:42:24

(a)

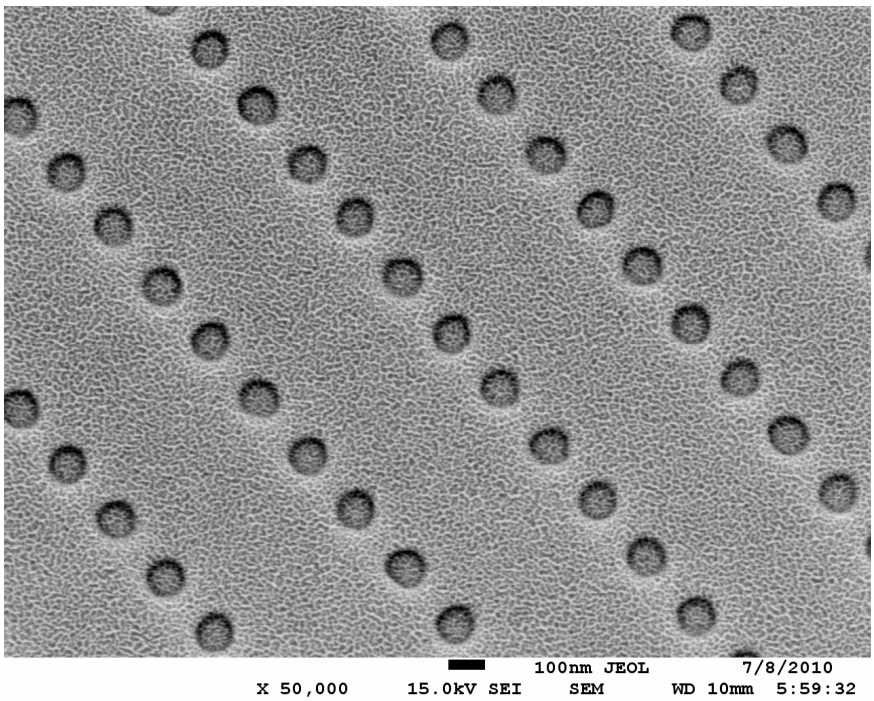
100nm JEOL 7/8/2010
X 50,000 15.0kV SEI SEM WD 10mm 5:59:32

(b)

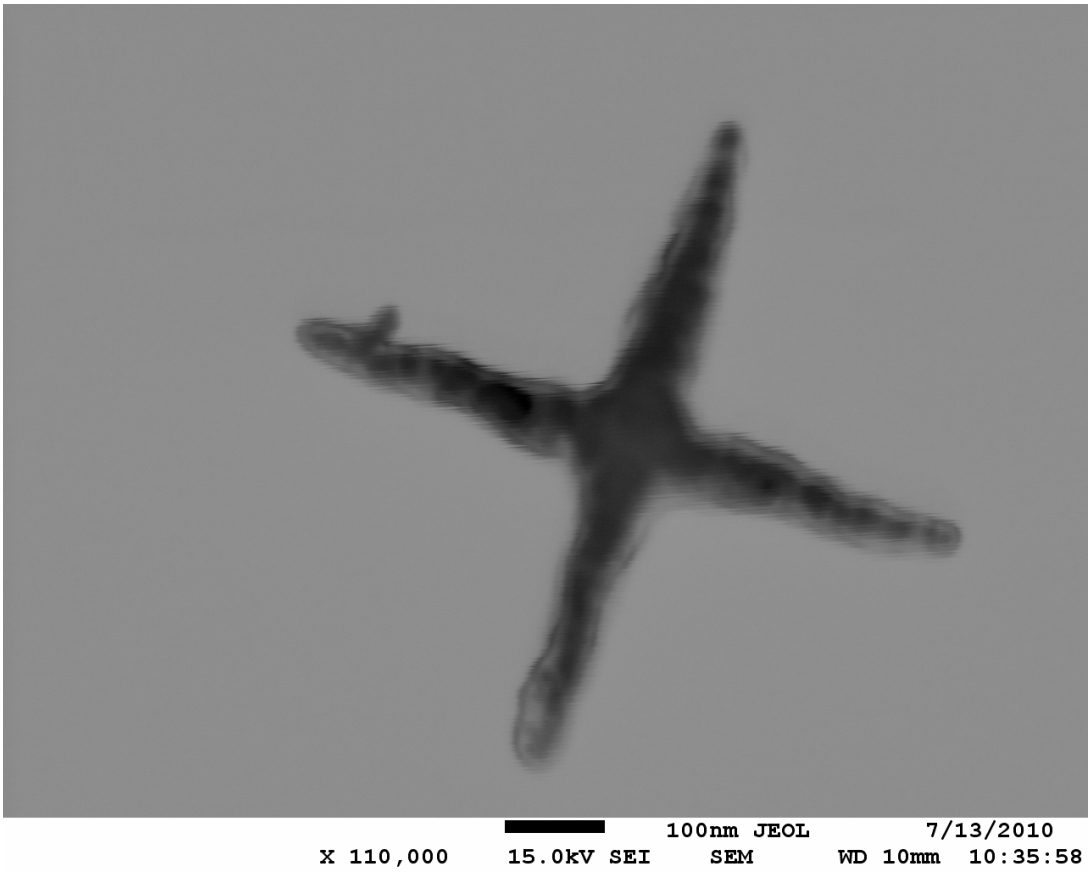

(c)

Figure 3.4. Representative SEM images of structures produced by EBL. (a) 40-nm-wide perpendicular lines, (b) 100-nm-diameter dots, (c) four-armed star made by EBL followed by gold deposition and lift-off.

3.2.1 Single-exposure EBL

In a single EBL-exposure process, a layer of SU-8 was first spin-coated on a silicon wafer with a thickness between 10 μm and 15 μm using the MicroChem SU-8 2010 or 2015 solutions. The initial spreading of the photoresist solution when being applied onto the wafer is important. A circular circumference of spread solution is highly preferred, any eccentricity could by severely amplified and cause the incomplete coverage of the wafer. Bubbles should be avoid or be extracted from the deposited photoresist solution, because the spin process push them towards the center of the wafer. The spin-coating was performed via a three-step process: 1) 100 rpm/sec accelerate to 500 rpm and stay at 500 rpm for 5 s; 2) 500 rpm/sec to 2000 rpm and stay for 7 s; 3) 1000 rpm/sec to 4000 rpm and stay for 28 s. The first two steps were implemented to help spreading of the coating solution, the final step speed determined the film thickness. The coated wafers were then baked at 95 °C (soft bake) for 5 minutes and carefully diced into 1 cm × 1 cm pieces after slowly cooled down to room temperature. The photoresist then underwent a specially-designed electron beam scan routine to write a dot pattern of sub-micron features. The center-to-center distance between nearby e-Beam exposure locations was specified based on the desired spacing of the secondary-features while the post radius was controlled by the dosage of the e-Beam, as shown in **Figure 3.5**. Specifically, a two-dimensional 50 × 50 array (total area 1 mm × 1 mm) of 10 μm or 8 μm squares with 20 μm period was generated in the DesignCAD Express. The center-to-center distance (CCD) and line spacing (LS) were both set to 500 nm in the NPGS. Parameters of the EBL are as the following: 30 kV acceleration voltage, 6 mm working distance, 130× magnification, 80 pA ∼ 220 pA beam current, 0.05 nC/cm ∼ 0.15 nC/cm line dosage (smaller dose produced thinner bridges between the blocks). A post exposure bake (PEB) of 5 minutes at 95 °C was perform after the e-Beam exposure, followed by a development in PGMEA for 30 s ∼ 60 s. Properly controlling the PEB is very important. Two thermally excited, temperature-dependent processes occur simultaneously on acid-catalyst molecules activated during the exposure: (a) diffuse through the SU-8 layer and (b) assist cross-linking of nearby SU-8 molecules. As temperature increases, the rate of chemical reaction (cross-linking) increases faster than the rate of diffusion. Therefore, high temperature (∼ 95 °C) PEB is preferable for maximizing contrast. Short periods of low

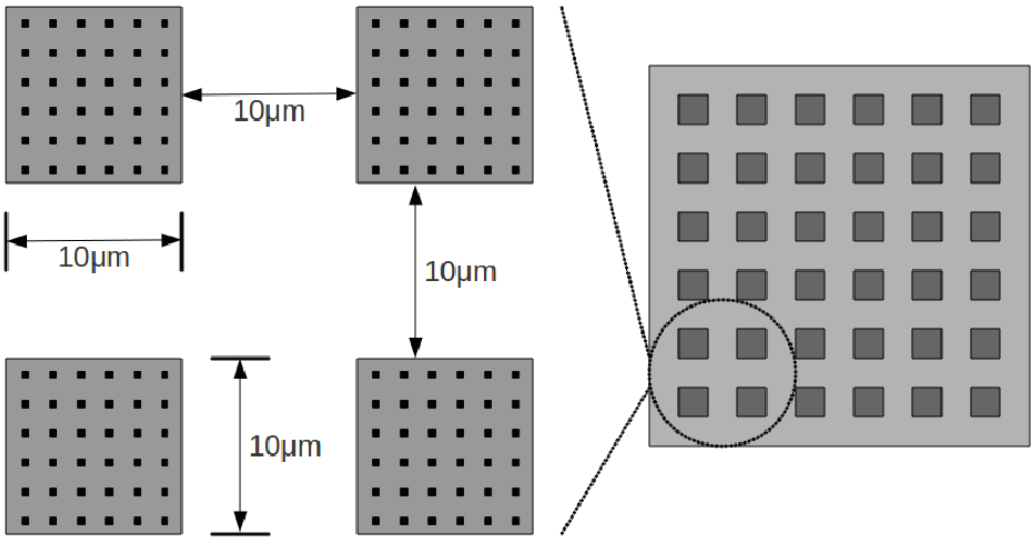

Figure 3.5. Schematic diagram of the hierarchical surfaces produced by a single EBL-exposure process. The secondary nanometer-features are directly written by e-beam lithography and the primary micro-structures are generated by a proximity effect. This way, both the primary and the secondary structures are generated within a single step and the secondary features are only on the tops of the primary structures.

temperature ($\sim$ 65 °C) pre-bakes are sometimes for the purpose of stress reduction, which can help improve adhesion and reduce crack generation. There was also an optional final hardening bake at 100 °C for 15 minutes performed on some of the samples. In the case of making the alternating structures, two CAD files were drawn with each corresponding to one type (either smooth or rough) of blocks, and the CCD and LS for the smooth ones were set to be 100 nm in the NPGS. Everything else was same as above. Hardening bake can help enhance the mechanical strength of the cross-linked SU-8 structures, reduce the number of cracks on the surface of these structures, and improve their adhesion to the surface of the wafer.

During the single EBL-exposure process, as the secondary features are being produced by electron exposure, the proximity effect helped to simultaneously implement the primary features, specifically, elevated bases with a significantly larger length-scale (i.e., about 10 μm) were generated where the exposure density is high. To explain the proximity effect, it is necessary to take a close look at how the incident electrons interact with the photoresist

layer. There are generally two categories of interactions between the incident electrons and the sample: elastic scattering and inelastic scattering. Elastic scattering is characterized by the negligible energy loss of the incident electron. In this case, the incident electrons interact with the much heavier nuclei (via Coulombic force) and change their trajectories, but their kinetic energy and velocity remain essentially constant. The majority of elastic scattering events produce back-scattered electrons (BSE). Inelastic scattering, on the other hand, involves substantial energy transfer from the incident electrons to the inner shield electrons in the sample. These inelastic collisions can produce various types of signals including secondary electrons, Auger electrons, X-rays, and UV and visible light. In the case where a high energy incident electron beam is applied, it is also possible to have second- and third-generation scattering events. For example, a high energy incident electrons can produce a high energy BSE at the first scattering event, then the BSE can go through a second scattering event and generate medium energy X-ray, then the X-ray can go through a third scattering event and generated a low energy secondary electron. That is just one possible pathway, and there are many other routes. In general, via this type of cascading multiple-scattering process, a small-diameter high-energy incident electron beam can trigger scattering events across a much larger volume than its projected volume. As shown in **Figure 3.6 (a)**, the shapes of the interaction volumes in many solids often resemble a tear drop (three-dimensional, axially symmetric). Amongst the various particles and radiations that can be generated by interactions of a high energy (20 kV $\sim$ 30 kV) electron beam and a thick (10 μm $\sim$ 20 μm) photoresist film, the secondary electrons are most important for EBL. Secondary electrons are low energy electrons (usually defined by kinetic energy $\leq$ 50 eV) generated by the ionization of specimen atoms. 90% of the secondary electrons have energy less then 10 eV, and mostly between 3 eV and 5 eV. Secondary-electron signals are what most SEM imaging system based on, and they are crucial to EBL processes as well, mostly due to their energy range. Some approximate bonding energies of common chemical bonds are listed in **Table 3.1**. It is clear that energies many chemical bonds are within the range of the energy of secondary electrons. Therefore, in EBL, secondary electrons are largely responsible for chemical reactions such as cross-linking of the photoresist molecules. In the case of SU-8, UV radiations also have effects on cross-linking. Due to their low level of

Table 3.1. Approximate bonding energies of various chemical bonds.

Bond	H−H	O−H	C−H	C−C	C=C	C−O	C=O	O=O
Energy $[eV]$	4.52	3.79	4.28	3.61	6.36	3.73	7.97	5.16

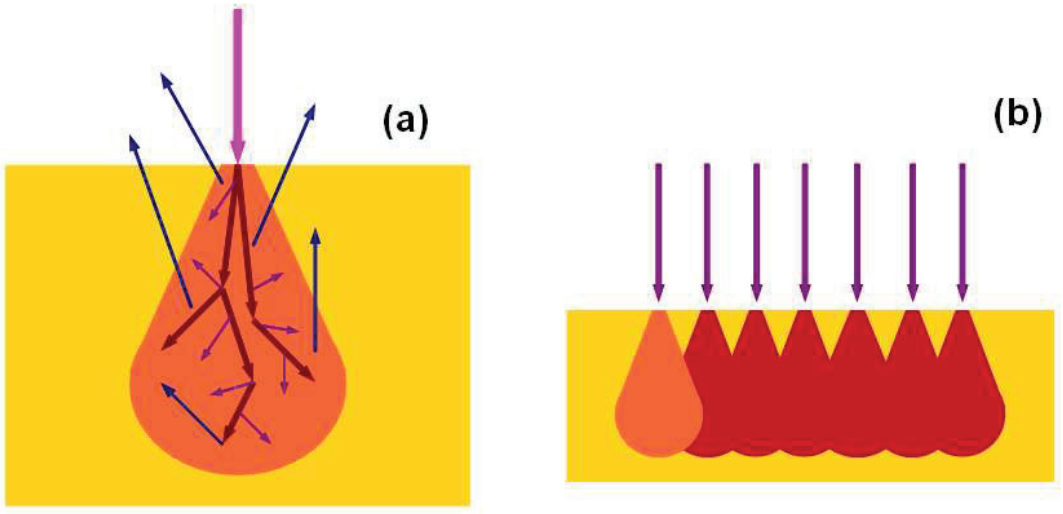

Figure 3.6. Schematics of the proximity effect: (a) the tear-drop shape interaction volume of a single high-energy incident electron beam, and (b) a bulk structure generation by high exposure density due to the proximity effect.

kinetic energies, secondary electrons can only travel a short distance inside the photoresist (the statistical distribution of the distance of travel is material dependent, but usually on the order of a few nanometers), this attributes to the high resolutions achievable by EBL with thin resist layers. In the case of a thick resist layer, since secondary electrons can be generated by particles and radiations with higher energies, their effects can cover most of the interaction volume, e.g., cause cross-linking of the entire tear-drop region. The mechanism behind the formation of primary structures in a single EBL-exposure process is illustrated in **Figure 3.6 (b)**, when the incident electron beams are programmed to be spaced densely enough, the individual interaction volumes can overlap one another and collectively form the large size base. Direct evidence of proximity effect can be observed in **Figure 3.7** (d) and (e), where the three-dimensional profiles of the interaction volumes are displayed.

Using this technique, the entire hierarchical structured surface was fabricated in one EBL step, and the secondary features only covered the tops of the micro-scale primary structures as seen in **Figure 3.7** (a) $\sim$ (e). As a result, a very high level of control over the distributions of the secondary-features was possible. For example, as demonstrated in **Figure 3.7 (c)**, it is possible to fabricate an array of primary blocks with alternating rough and smooth tops (i.e., with or without secondary-features on top). Moreover, asymmetric structures can also be fabricated, as shown in **Figure 3.7** (f) $\sim$ (k). More specially, directional asymmetry in hierarchical structures can include: (1) asymmetry in each individual primary structure; (2) asymmetry in the arrangement (lattice) of primary structures; (3) symmetry in the distributions of secondary structures; (4) combinations of any the above. Formation of structures shown in **Figure 3.8** (f), (h), and (i) are speculated to be caused by the combination of under-dosed electron exposure and capillarity during development (more specifically the dewetting processes of the developer solvent). Further studies are required before any conclusive statements can be made.

On our SEM-EBL system, the maximum field size an e-Beam writing can cover without moving the stage is dictated by the magnification. This in turn affects the resolution of the lithography. To balance resolution and efficiency, a magnification of 130×, which corresponds to a maximum writing field of 1 mm × 1 mm, was chosen and was found to provide acceptable writing resolution of both the micro and nano-scale features. The total EBL time of a single-exposure sample (consists of four 2 mm × 2 mm surfaces) was between 15 and 45 minutes depending on the electron beam current used.

3.2.2 Double-exposure EBL

In order to fabricate hierarchical structures where nano-features cover not only the tops of the micro-features but also their sidewalls and the valleys between them, as seen in **Figure 3.8**, we also experimented with double-exposure procedure. The schematic of this procedure is shown in **Figure 3.9**. In a double-exposure process, a large scale exposure which can be done by either EBL or UV photo-lithography was first performed on a thick layer (10 μm $\sim$ 15 μm) of SU-8 to induce cross-linking of the micro-scale primary features. In our experiments, we typically created an array of 10 μm square blocks spaced 10 μm

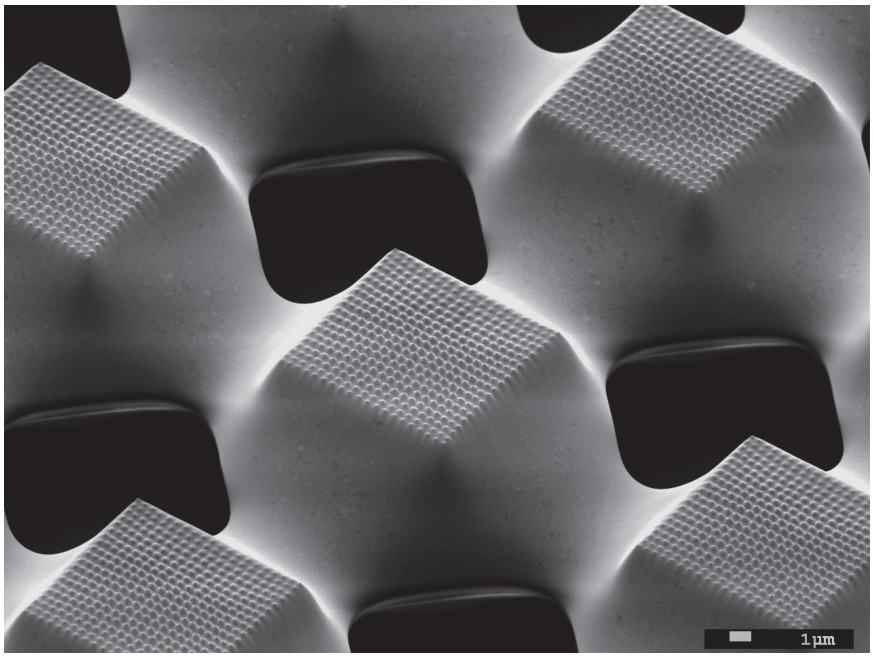

(a)

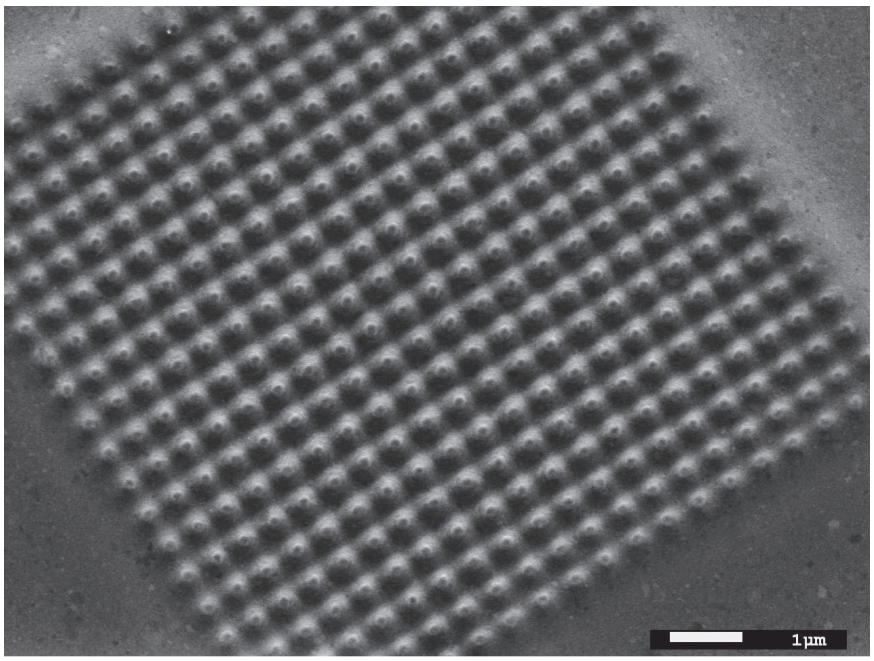

(b)

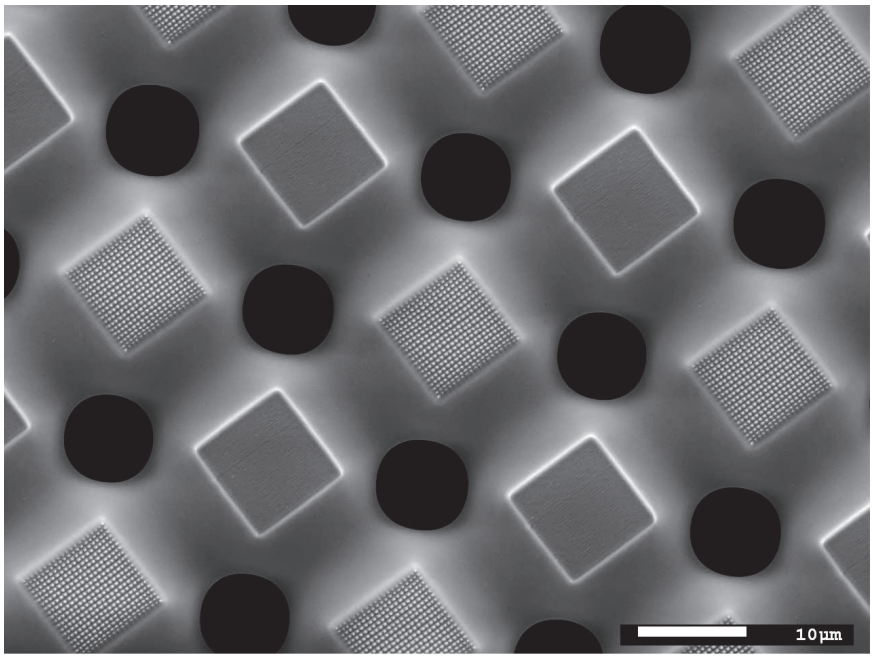

(c)

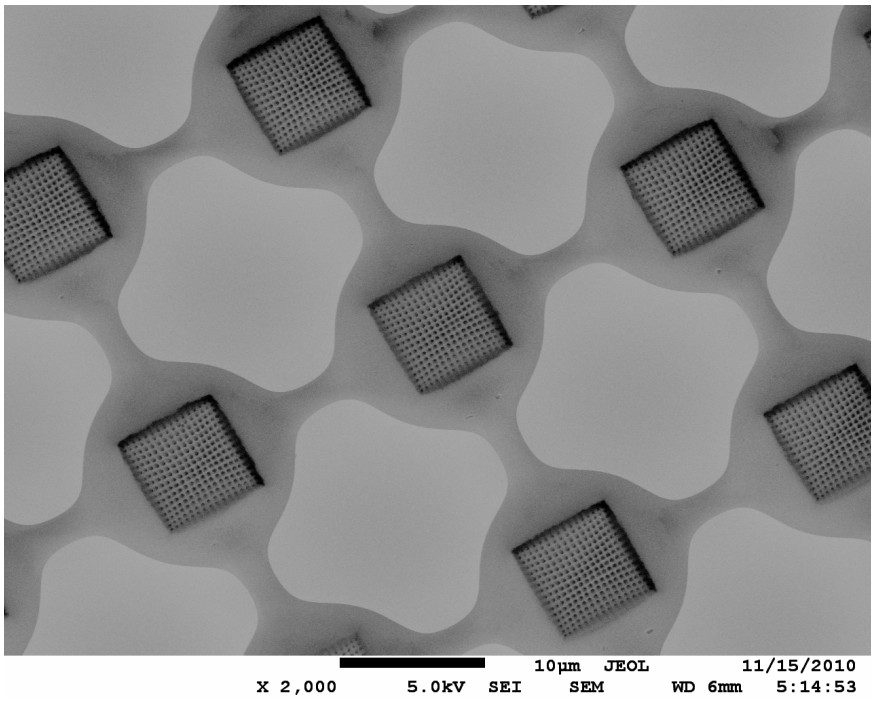

(d)

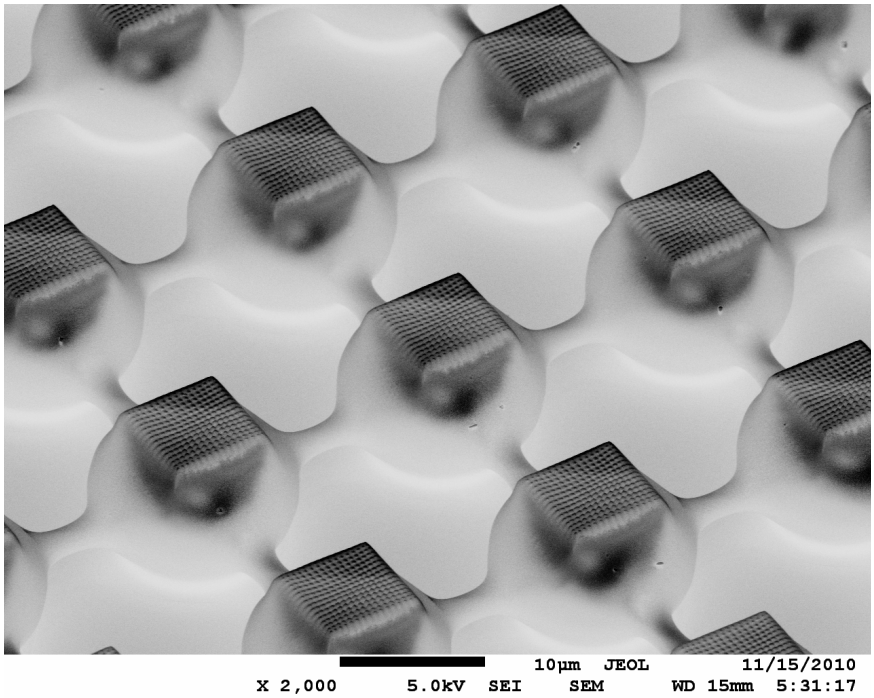
10µm JEOL 11/15/2010
X 2,000 5.0kV SEI SEM WD 15mm 5:31:17

(e)

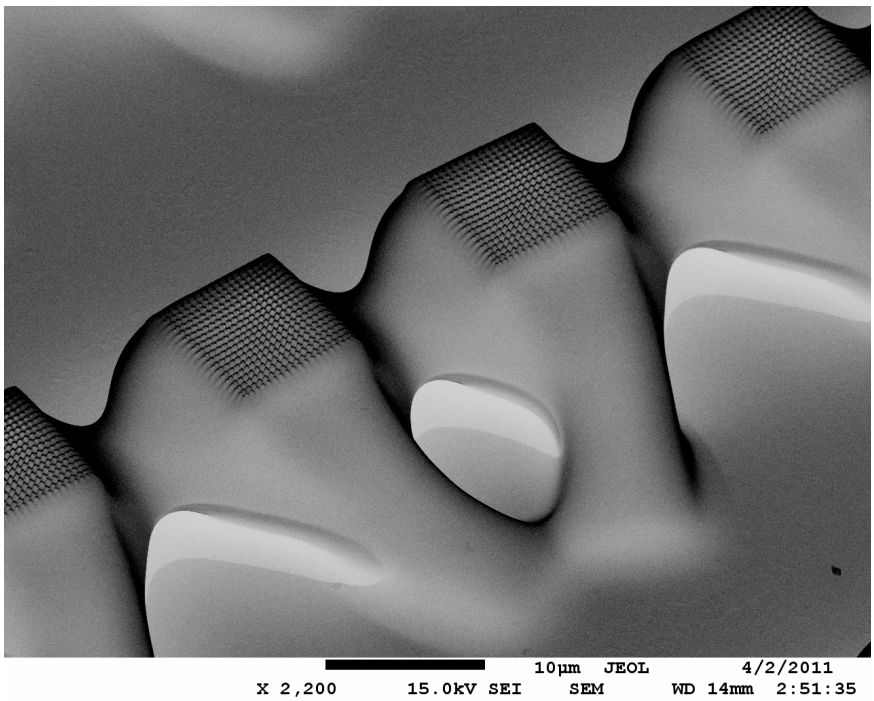
10µm JEOL 4/2/2011
X 2,200 15.0kV SEI SEM WD 14mm 2:51:35

(f)

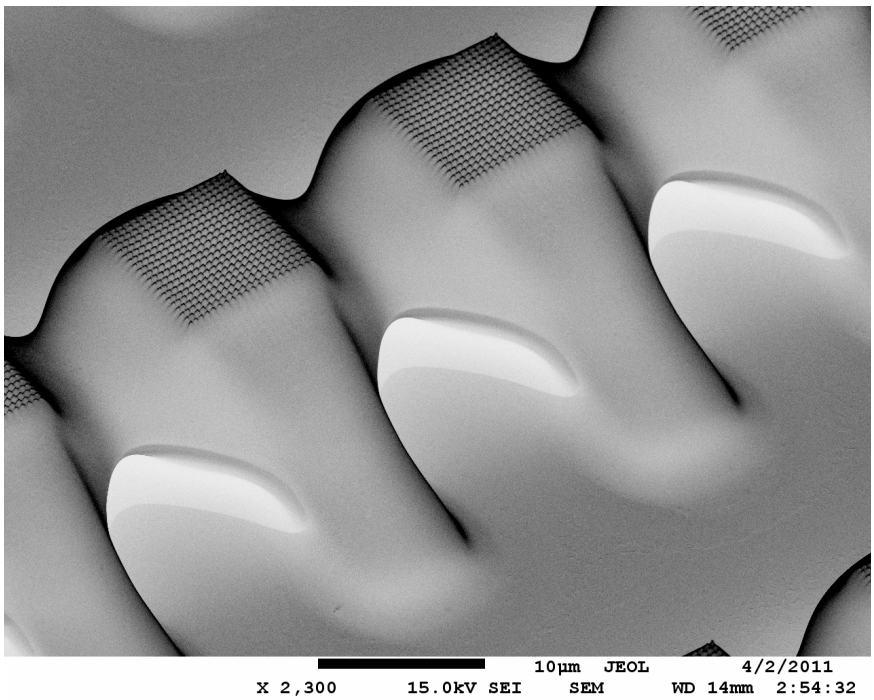
10µm JEOL 4/2/2011
X 2,300 15.0kV SEI SEM WD 14mm 2:54:32

(g)

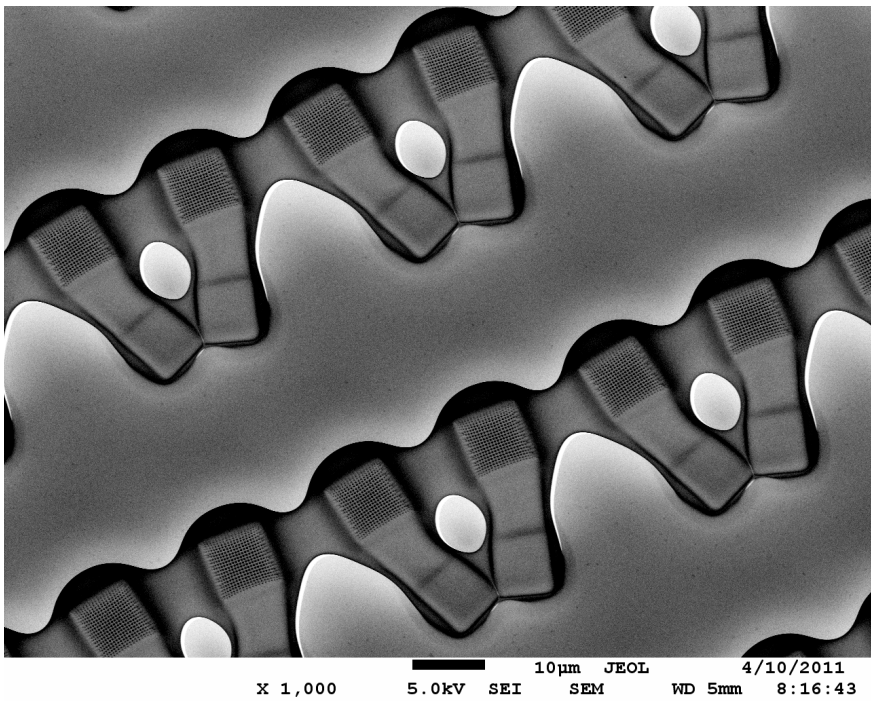
10µm JEOL 4/10/2011
X 1,000 5.0kV SEI SEM WD 5mm 8:16:43

(h)

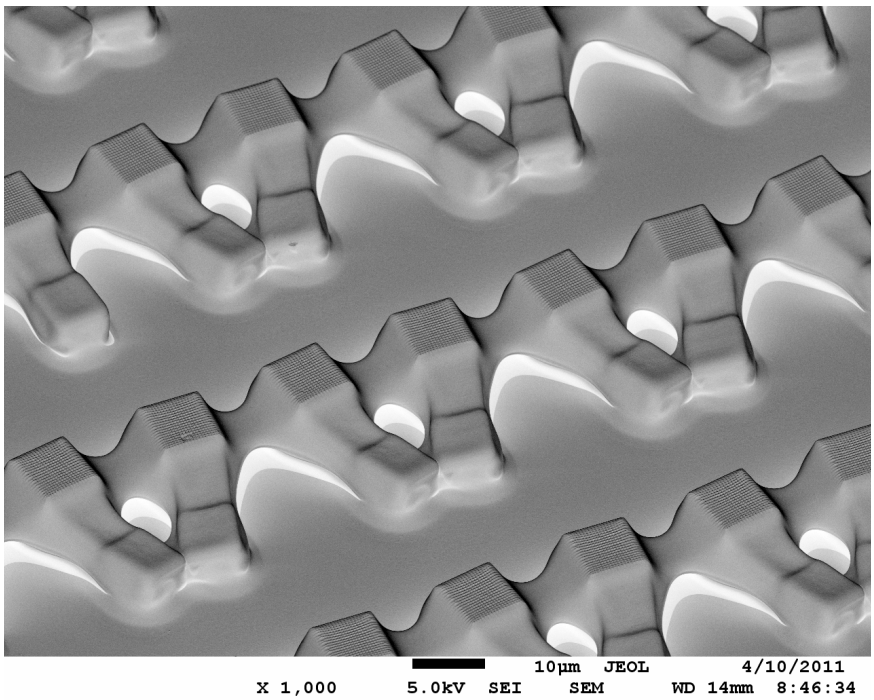
10µm JEOL 4/10/2011
X 1,000 5.0kV SEI SEM WD 14mm 8:46:34

(i)

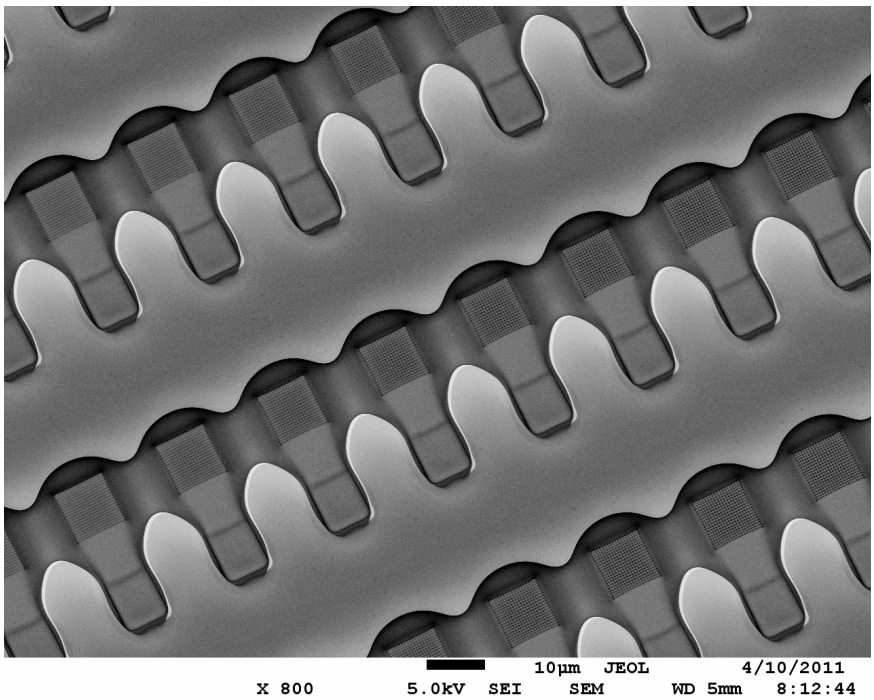
10µm JEOL 4/10/2011
X 800 5.0kV SEI SEM WD 5mm 8:12:44

(j)

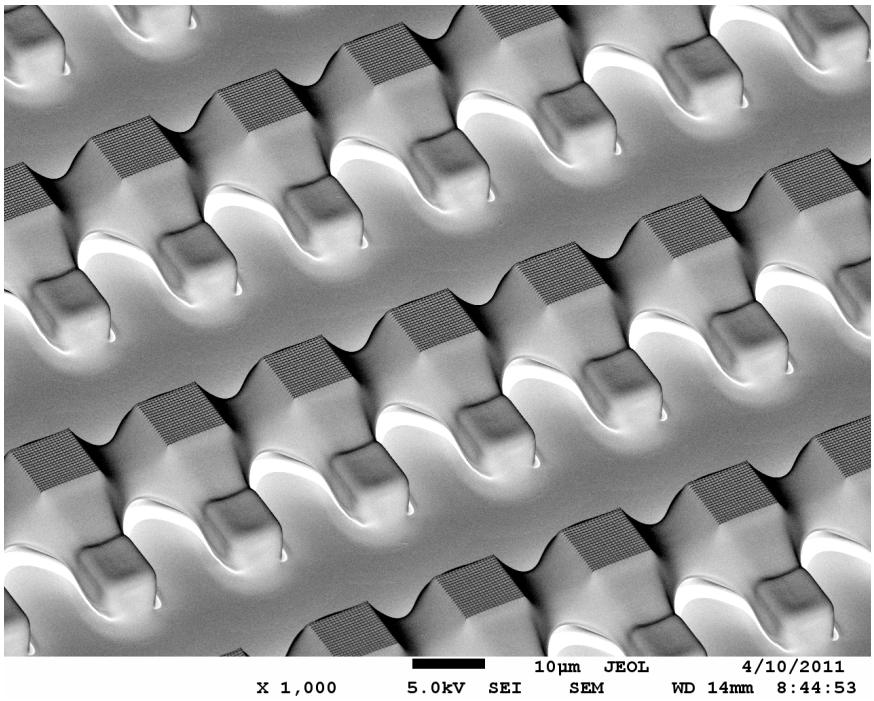

(k)

Figure 3.7. Representative SEM images of hierarchical structures with secondary posts fabricated by single EBL exposure process. Images (a), (e), (f), (g), (i), (k) were taken at 45°-tilt. Images (b), (c), (d), (h), and (j) were top view. The secondary features displayed in (a) $\sim$ (e) show a 500 nm period and aspect-ratio close to one. Images (a) and (b) were taken on the same surface with different magnifications. In (c), a hierarchical surface with alternating smooth and rough tops (top view) were demonstrated. Image pairs (d) and (e), (h) and (i), (j) and (k) each display a same surface at different viewing angles.

apart. After a post exposure bake (PEB-1), a thin layer of SU-8 on the order of 500 nm in thickness was spin-coated on top of the undeveloped layer. A second exposure with EBL was then applied to construct the secondary-features over the entire surface. The best secondary structures were found to be written at a magnification of 650×, which corresponds to a field size of 200 μm × 200 μm. In this case, each 2 mm × 2 mm surface is covered by a 10 × 10 array of EBL patches. Lower magnifications can be used for lower resolution requirements and would require fewer patches. The surface was then put through a second post exposure bake (PEB-2) and finally it was developed, resulting in hierarchical structures seen in **Figure 3.8 (c)**. For a double-exposure sample (consists of four 2 mm × 2 mm surfaces), the first exposure took between 5 and 15 minutes and the second exposure took between 30 minutes to 2 hours depending on the magnification and beam current used.

More details on the double-exposure process: the first exposure was done similar to a single-exposure e-Beam. The only changes were: CAD design was a 100 × 100 array (covering a total area of 2 mm × 2 mm), magnification was 60×, CCD and LS were both 100 nm, PC was 10 ∼ 11 (600 pA ∼ 700 pA), area dosage was 1.4 $\mu C/cm^2$, and the development was omitted. After the PEB of the first exposure, the sample was slowly cooled down to room temperature, then a second spin-coating was done on top of the first layer with SU-8 2000.5 at 3500 rpm for 30 seconds. CAD design for the second exposure was a 200 μm × 200 μm square and CCD and LS were both 200 nm, 300 nm, 400 nm, or 500 nm. The small-scale e-Beam was completed with 10 × 10 writings (mechanical stage movement in between writings), magnification of each writing was 650×, beam current was 80 pA ∼ 250 pA, and line dosage was 0.03 nC/cm ∼ 0.15 nC/cm. Following the second exposure was another PEB at 95 °C for 3 minutes and finally a 1 minute development in PGMEA.

SEM images of the hierarchical structures in **Figure 3.7** (a) ∼ (e) and **Figure 3.8** illustrate the similarities and differences between the two prototypes of dual-scale EBL. The primary structures were designed in both cases to be 10 μm square blocks spaced 10 μm apart. 5 μm and 8 μm square blocks were also experimented as primary features and the resulted structures were similar. Swelling towards the base of the primary features and consequently the forming of bridges between nearby blocks is beneficial for enhancing

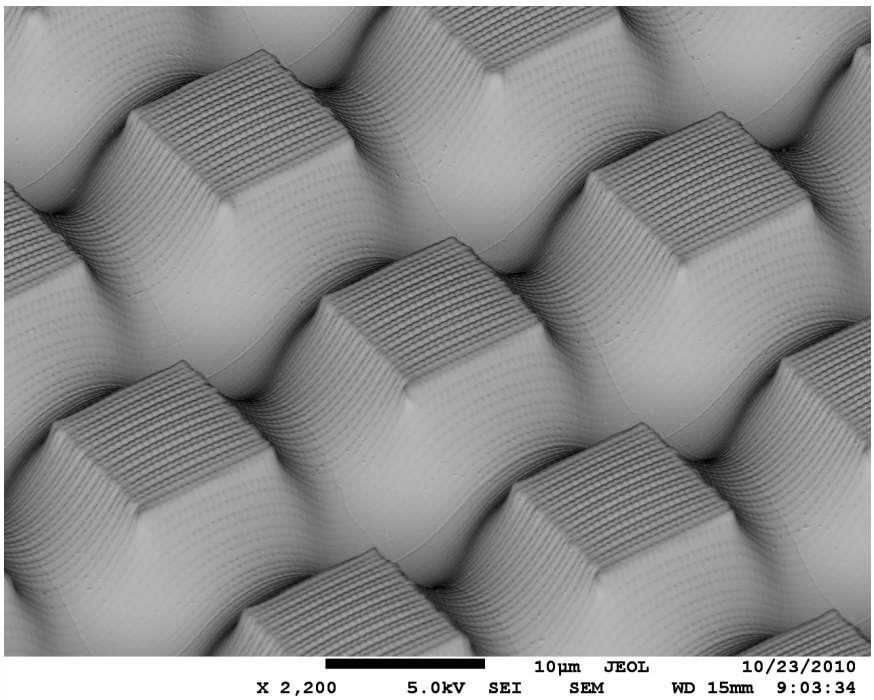
10µm JEOL 10/23/2010
X 2,200 5.0kV SEI SEM WD 15mm 9:03:34

(a)

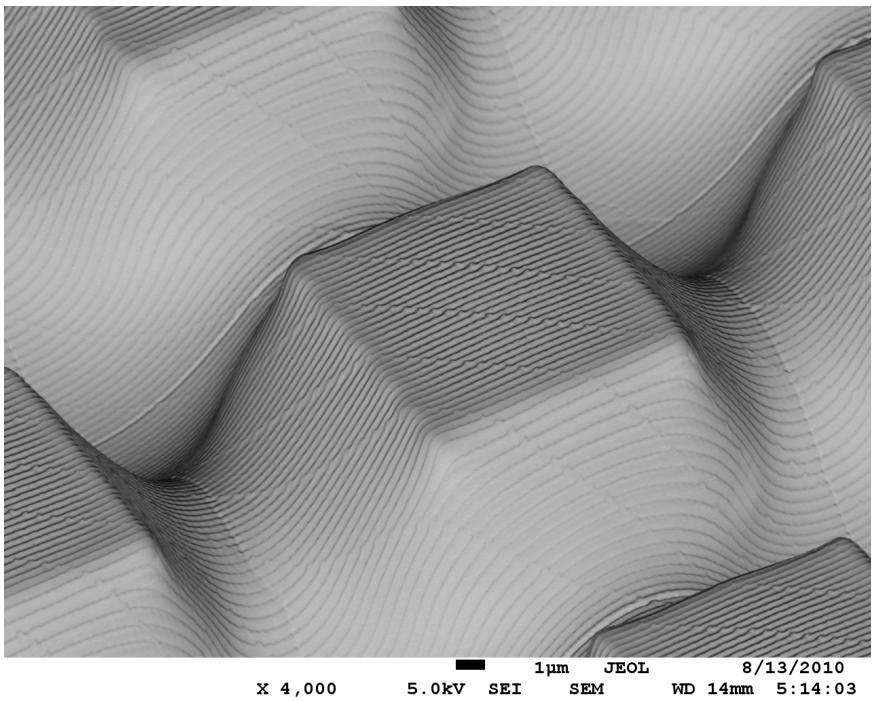
1µm JEOL 8/13/2010
X 4,000 5.0kV SEI SEM WD 14mm 5:14:03

(b)

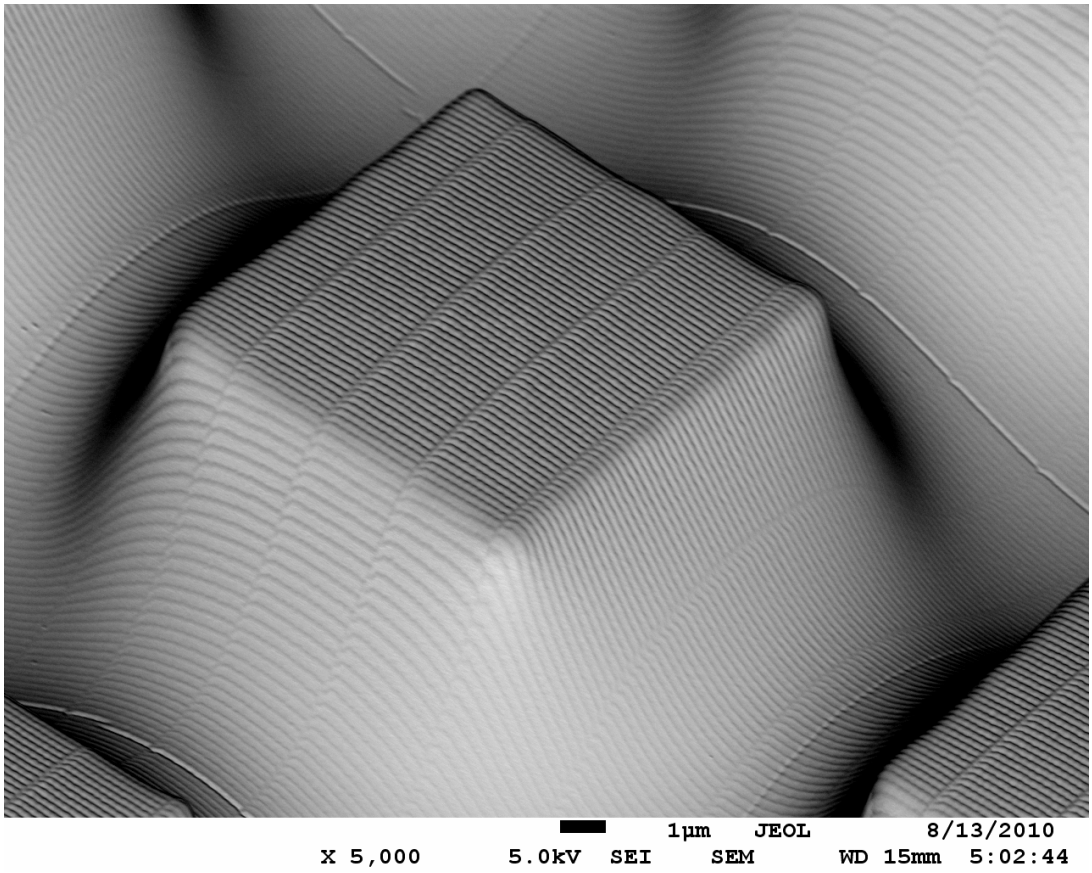

(c)

Figure 3.8. Double EBL-exposure sample with secondary ridges. All three images were taken at a 45° tilt. The primary blocks are of the dimension of about 10 µm × 10 µm × 8 µm. The periods of secondary ridges are (a) 400 nm, (b) 300 nm, and (c) 200 nm.

adhesion between the structures and the substrate. Both ridges and posts have been implemented as the secondary-features with periods ranging from 200 nm to 500 nm. The secondary features shown in **Figure 3.8 (c)** are ridges with a width of 70 nm on average (at half height) and a height of 70 nm. These ridges cover the entire surface including the bottom of the valleys between the large posts. The spacing of the secondary ridges on some side-surfaces (whose normal is roughly perpendicular to the direction of the ridges) have been increased due to the slope of the sidewall. These features were made possible by the large penetration depth and large depth of focus of the high energy electron beam. In comparison, nano-posts shown in **Figure 3.7** (a) $\sim$ (e) cover only the top of the primary features. The average diameter of these posts is around 200 nm with a designed period of 500 nm and average height of about 150 nm. Whether ridges or posts were produced in the second exposure was found to mainly depend on the beam current used with increasing current favoring ridges. In our SEM/EBL system, exposure done at 30 kV with Probe Current (PC) 7 (corresponding to about 120 pA) or lower produced posts; exposure done with PC 8 (corresponding to about 220 pA) or higher produced ridges. Additionally, for both secondary ridges and posts, the feature size and height mainly depended on the exposure dosage and were found to be relatively insensitive to the thickness of the SU-8 layer. Among all our samples, the highest secondary-feature aspect-ratio was about 0.85 for ridges and 0.75 for posts. As always, the proficiency of the operator in beam alignment and aberration minimization, and the capability to align the position of the second writing with the first one is critical to getting high-quality reproducible lithography results.

3.3 Wetting Properties of the Hierarchical Surfaces

A series of double-exposure hierarchical surfaces with identical primary (10 μm quare posts spaced 10 μm apart) but variable secondary-features were fabricated for a comparative wettability study. After EBL, a 10 nm layer of silicon monoxide was thermally deposited on each sample surfaces and subsequently modified with a fluoro-alkyl-silane via a vapor phase reaction (for more detail refer to experimental section). An oxygen plasma treatment were needed to turn the SiO into SiO_2. The treatment was performed for 60 seconds with the following settings: power at 200 W, pressure at 250 mTorr, O_2 flow rate at 50 sccm.

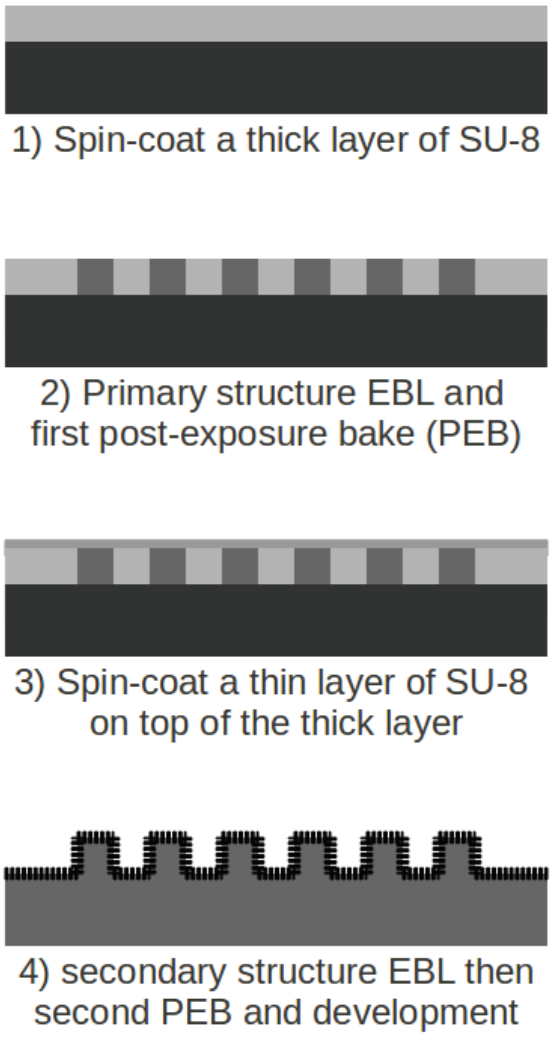

Figure 3.9. Schematic diagram of the fabrication of hierarchical SU-8 surfaces via a double EBL-exposure process.

The samples were then transferred into a closed reaction chamber where the silanization was carried out at 80 °C for 4 days. Solution of (Tridecafluoro-1,1,2,2-tetrahydrooctyl)-dimethylchlorosilane (> 95%) from Gelest was used for silanization. The initial silane (liquid) volume ratio was 1% with respect to the chamber volume. After the silanization, all samples were washed with, in this order, acetone, IPA, and DI wafer, and finally dried with nitrogen.

The surface properties were characterized with quasi-static measurements of the advancing and receding CAs. When measuring the CAs, care was taken to ensure the measurements represent the thermodynamic equilibrium states. A droplet of water with a diameter of approximately 1 mm was deposited on the hierarchical surfaces from a needle mounted approximately 0.5 mm above the surface. A syringe was then used to expand and contract the drop in order to measure the advancing and receding angles respectively. The measurements were taken from images captured with a video camera employing a long distance microscope objective. These images were processed in ImageJ to determine CAs. Several cycles of the water droplet expansion and contraction were performed before each measurement to ensure thermally stable CA values were measured. When conducting CA measurements on samples with secondary ridges, no attention was paid to the direction of the ridges with respect to the camera angle. Two distinctive behaviors were observed as the result of varying the secondary structures. First, a number of surfaces demonstrated high advancing CA with low hysteresis. These low-adhesion surfaces are examples of what is known as the lotus effect where the water remains in the Cassie state over both the micro-scale and nano-scale features on the surface. Second, high advancing CA with high hysteresis were observed in some cases. These high-adhesion surfaces are examples of the rose-petal effect where the water remains in the Cassie state over the large scale features, but fully wets and therefore exists in the Wenzel state on the nano-scale features superimposed on the tops of the micro-scale posts, i.e., type-II partial Wenzel state. In some cases, with the secondary structures being either posts or ridges, pinning of contact line were clearly observed in the videos taken for CA measurements. In those cases, the CA were determined based on the macroscopic profiles instead of the microscopic pined edges. Both high-adhesion and low-adhesion behavior were observed on double-exposure

samples with secondary-posts having periods 200 nm, 300 nm, 500 nm. Conversely, all of the double-exposure samples with secondary-ridges and all of the single-exposure samples showed high-adhesion behavior regardless of the period of the secondary-features.

An advancing and a receding water CA measured on each of our silanized double-exposure surfaces, together with their average values, are plotted on **Figure 3.10 (a)** with error-bars to show the uncertainty. The advancing CAs for all the surfaces independent of secondary-feature spacings or geometries were found to remain fixed at 160° with variations of less than 5°. Therefore, all these hierarchical surfaces are superhydrophobic. This observation also suggests that the advancing CA is mainly set by the micro-scale features which, for these experiments, were fixed and not varied. The effect of varying secondary features on advancing CA is minimal. The receding CA values, on the other hand, appear to divide the data into the two regimes we have discussed earlier. In the low-adhesion cases, the receding CAs were found to reside above 120°. In the high-adhesion cases, the receding CAs were consistently below 90°, resulting in very large CA-hysteresis values. Unlike the advancing CA, the receding CA is found to depend on both the period and geometry of the secondary features. This can be quantified by performing linear regressions through the experimental data. As shown in **Figure 3.10 (a)**, the advancing CAs appear to be statistically independent of secondary-feature period, varying by less than 1° for every 100 nm change in the period of the secondary feature. A statistically significant correlation was found between the secondary-feature period and the receding CA. This is most apparent for the high-adhesion cases where the receding CA was found to increase by more than 3° for every 100 nm increase in secondary-feature spacing. In the low-adhesion cases, the dependence was found to be significantly weaker.

Figure 3.10 (b) compares the advancing and receding CAs measured on various structured surfaces. With the same surface-chemistry treatment, the average advancing CAs of all hierarchical surfaces in our experiments were the same as that of a surface with only 10 μm blocks but about 30° higher than that of a surface with only nano-ridges (300 nm period). This is additional evidence that the advancing CA is dictated primarily by the primary features. The average receding CAs of the hierarchical surfaces in the high-adhesion zone were close to that of the nano-ridges decorated surface and about 50° lower than that

of the surface with only micron blocks. These observations indicates that, for a hierarchical surface, the advancing CA is mainly determined by the primary structures and the receding CA by the secondary structures, which is consistent with previous literature [Gao (2006) (b)]. Moreover, the coverage of the secondary structures does not appear to affect the receding CAs when only the high-adhesion regime is considered. This can be explained by the contact line dynamics model proposed by Gao and McCarthy as the following: on a hierarchically structured surface, advancing of a liquid droplet is achieved by sections of the front liquid-vapor interface descend onto the next micro-blocks to be wet, thus the roughness of the tops of the micro-structures do not affect this process; on the other hand, in a receding event, the edge of the contact region must disjoin from entire post tops in concerted events, and the energy required for this process depends heavily on the details of the liquid-solid interfaces.

Furthermore, there did not seem to be a direct correlation between the average-dosage of the second exposure and the receding CA. In fact, in some cases the same normalized dosage gave two distinctive behaviors with receding CAs differing for as much as 43°. To understand the main factors that account for the large variation of surface adhesion among samples where the EBL parameters and fabrication protocol were only slightly different, a closer examination, Atomic Force Microscopy (AFM) measurements, on the surface topology of the secondary structures was necessary. It should be mentioned that the RTESP probe from Veeco was used in all AFM scanning. AFM measurements were only performed on the plateau of the primary features with tapping mode (scan rate 1.0 Hz, driving amplitude at 1.05 $\sim$ 1.20 V, integral gain 0.3, and proportional gain 0.5). Data was then analyzed with Gwyddion, where background flattening of zeroth, first, and second order (also in that sequential order) was preformed.

Representative images of both high and low adhesion surfaces are presented in **Figure 3.11**. Our measurements indicate that secondary-feature aspect-ratio by itself does not directly correlate with CA hysteresis. It was found that low hysteresis surfaces can be produced with either high or low aspect-ratio secondary-structures. Among the low-adhesion surfaces, it is the one with a moderate aspect-ratio that gives the highest receding CA (**Figure 3.11 (a)**). By comparing the secondary-features of low-adhesion (**Figure 3.11**

(a)) and high-adhesion (**Figure 3.11 (b)**) surfaces, it can be concluded that the decisive factor that leads to low or high adhesion is the profile of the nano-features. For low adhesion surfaces, the tops of the secondary-structures are flat with sharp edges transitioning to their side walls, which indicates a relatively steep sidewall slope. The high adhesion surfaces all contained secondary nano-features with rounded or even pointed tops as seen in **Figure 3.11 (b)**, which indicates a relatively shallow sidewall slope. The flat tops and steep sidewalls of the low adhesion nano-features contributes to contact line pinning and therefore stabilization of the Cassie state on the secondary structures. This, in turn, lowers the total contact area and increases the receding CA. The variation in surface properties under similar fabrication protocols highlights the sensitivity of the fabrication technique to small changes in resist thickness, substrate properties, and e-Beam exposure parameters. Some work is still needed to increase the consistency and yield of low adhesion superhydrophobic surfaces beyond the level achieved here.

3.4 Conclusions of the Hierarchical Surface Project

To conclude this chapter, our most important contribution in this project is developing a novel, versatile, and efficient EBL technique for fabricating macroscopic hierarchical superhydrophobic surfaces. This technique allows for precise control over both the primary and the secondary structures, so we believe it can serve as a useful tool with which the effect of hierarchical surface structures on wetting and adhesion can be studied systematically with unprecedented versatility and precision. There are two varieties of this dual-scale EBL technique: single- and double-exposure. The single-exposure method is good for controlling the distributions of the secondary features only on specific sets of primary structures or only on specific parts of the primary structures. The double-exposure method is good for implementing complete coverage of secondary features on and between the primary structures. We have explained in detail how to manipulate the feature-spacing (from 200 nm to 500 nm), shape (either ridges or posts), and distribution (either over the entire surface or only on the tops of the primary structures) of the secondary-structures, as well as the underlining mechanism (the proximity effect) which enabled the formation of the base in a single-exposure process.

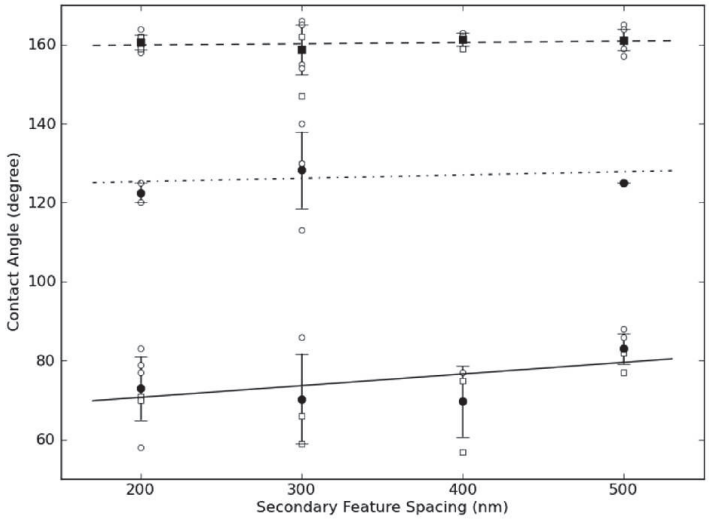

(a)

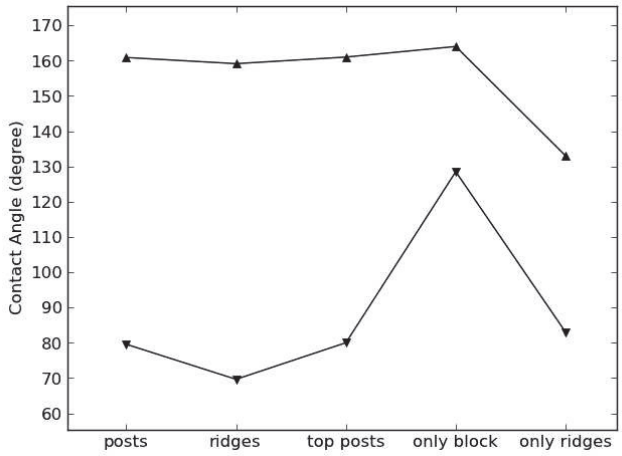

(b)

Figure 3.10. Advancing and receding CAs of water droplets on silanized hierarchical surfaces. (a) Samples with secondary-features covering the entire surface. Raw data-points are represented by open symbols. Open circles correspond to samples with secondary-posts and open squares correspond to samples with secondary-ridges. Notice some raw-data point overlap. Average values are represented by closed symbols (with error bars). Solid squares correspond to average advancing CAs, and solid circles correspond to average receding CAs. Also shown are linear fits for advancing CAs (dashed line), receding CA of low-adhesion cases (dash-dotted line), and receding CA of high-adhesion cases (solid line). (b) Average advancing (▲) and receding (▼) contact angles of various structured surfaces: (1) hierarchical surface with secondary post all over; (2) hierarchical surface with secondary ridges all over; (3) hierarchical surface with secondary posts on the tops only; (4) surface with only 10 μm blocks; (5) surface with nano-ridges only.

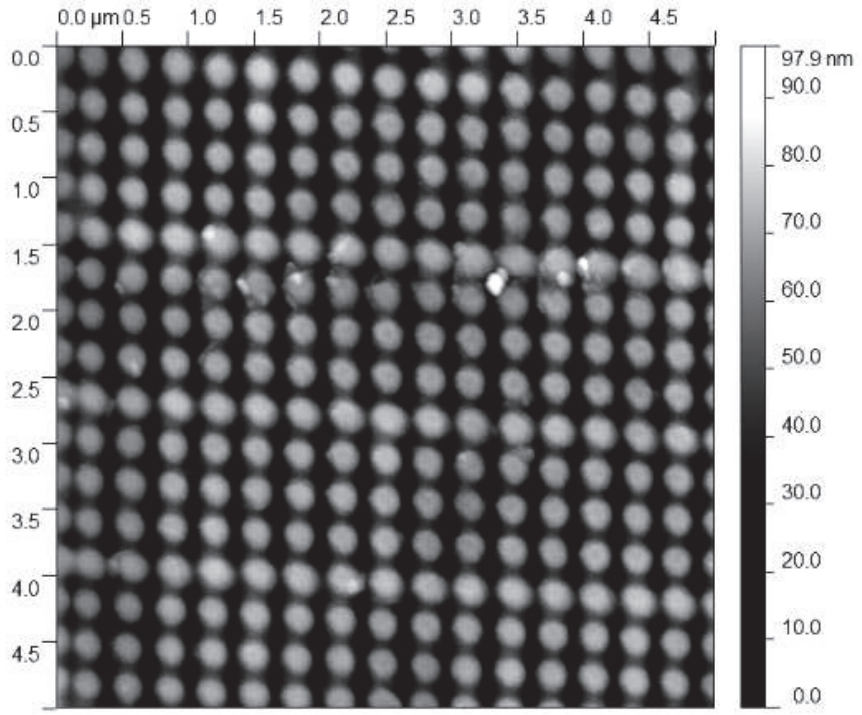
0.0 µm 0.5 1.0 1.5 2.0 2.5 3.0 3.5 4.0 4.5
0.0 0.5 1.0 1.5 2.0 2.5 3.0 3.5 4.0 4.5
97.9 nm
90.0
80.0
70.0
60.0
50.0
40.0
30.0
20.0
10.0
0.0

(a)

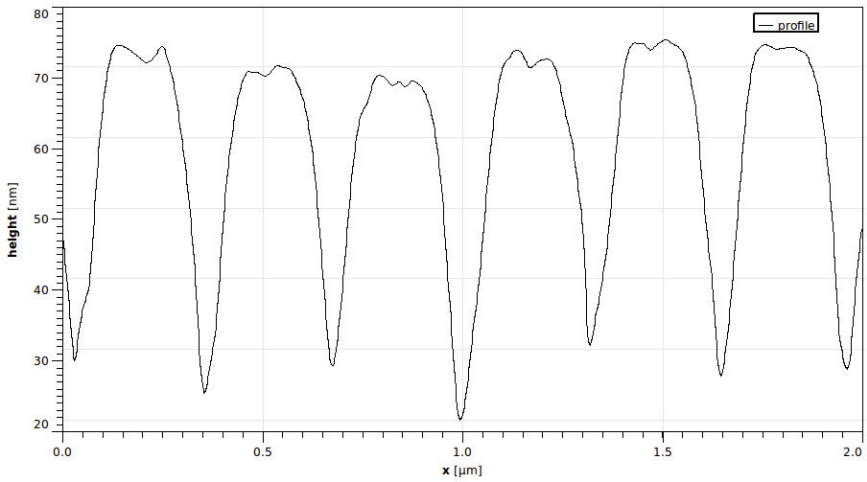
profile
height [nm]
80 70 60 50 40 30 20
0.0 0.5 1.0 1.5 2.0
x [µm]

(b)

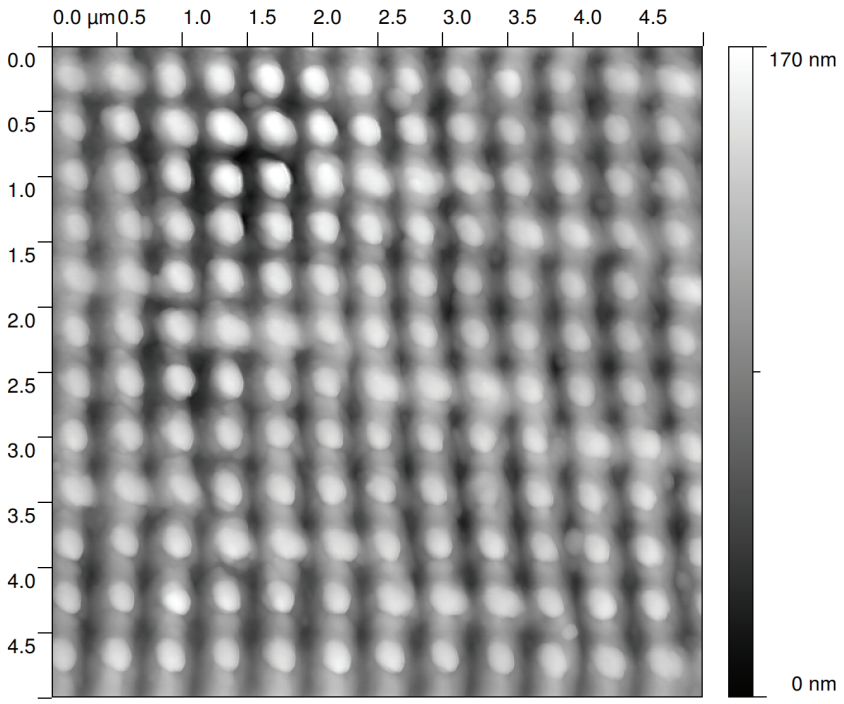

(c)

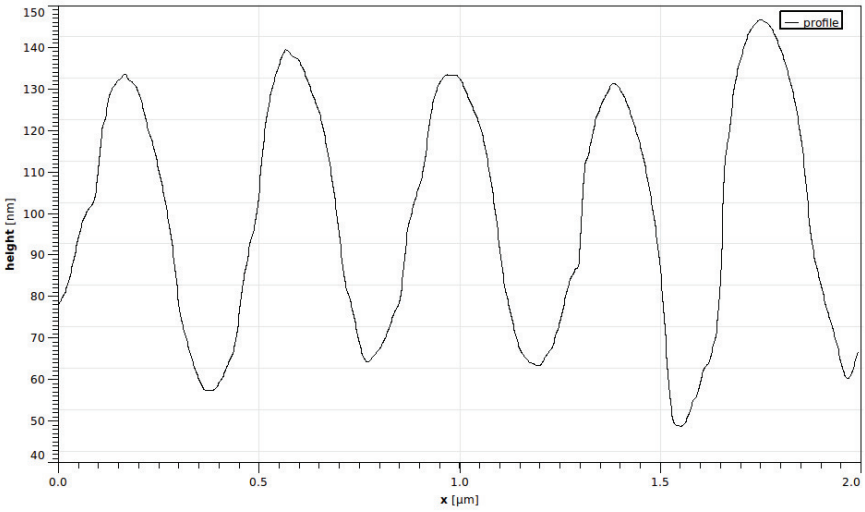

(d)

Figure 3.11. Representative AFM images and height profiles of the secondary structures on a low-adhesion surface ((a) and (b)), and a high-adhesion surface ((c) and (d)).

Surfaces produced by this technique were used to quantitatively study the structure−property relations of superhydrophobicity. The main results were: the advancing CA is mainly determined by the primary structures while the receding CA is significantly affected by the details of the secondary features. This is due to the difference between the advancing and receding dynamics. More specific results including: First, we confirm that the advancing CA is insensitive to the spacing, shape, or distribution of the secondary-features. Second, we found that two distinct regimes can be reached by similar hierarchical structures, and that the determining factor is not the aspect-ratio but rather the sharpness of the transition from the top to the sidewall of the secondary structures. This transition indicates the slope of the sidewall and whether a type-II partial Wenzel state (high-adhesion state) or a Cassie state (low-adhesion state) is more favorable. Third, the receding CA of low-adhesion surfaces does not exhibit clear dependency on the secondary-feature spacing. Fourth, the receding CA of high-adhesion surfaces increases by approximately 3° per 100 nm increase in secondary-feature spacing.

Some successful attempts of utilizing the single-exposure EBL technique to produce asymmetric structures have also been presented, but these asymmetric structures did not lead to useful asymmetric spreading behavior. In order to achieve directional wicking behavior, a new design is required. One such design will be introduced in **Chapter 4**.

CHAPTER 4

STRUCTURE-INDUCED ASYMMETRIC WICKING IN MICROFLUIDIC CHANNELS

Structures influence properties in various ways. Understanding the mechanism behind specific phenomena is of immense value to scientists and engineers in helping them build models, make predictions, and optimize designs. A subgroup of such relations is asymmetric structures leading to directional behaviors. Here we have performed an experimental study on direction-dependent wicking behavior induced by structural asymmetry in microfluidic channels. The objective of this study was to develop geometry-based techniques for imposing a high level of control over the wicking of fluids within a microfluidic device. Specifically, we explored the use of structured micro-channels to modify the direction and strength of Laplace pressure so that the extent and speed of wicking of fluids can be varied. In this study, we experimentally demonstrate one-way microfluidic channels by decorating both side-walls of a linear micro-channel with an array of tilted fins (**Figure 4.1**). The direction-dependent Laplace pressure induced in these channels allows a wetting fluid to wick in a predefined direction while prohibiting spreading of the fluid film in the opposite direction. A series of fluids were tested to systematically study the effects of changing contact angle. Moreover, because these experiments used open microfluidic devices, we show that evaporation can have a large impact on the degree and speed of wetting. Numerical simulations were performed to investigate the three-dimensional (3D) interface profile developed by the liquid front as it wicked through the channels. These simulations showed that 3D effects were important in determining the wicking behavior of fluids in these micro-channels. The findings of this study are expected to provide a better understanding of how fluids interact with micro-scaled structures and to offer a new way of manipulating fluids at the micron and nanometer scale.

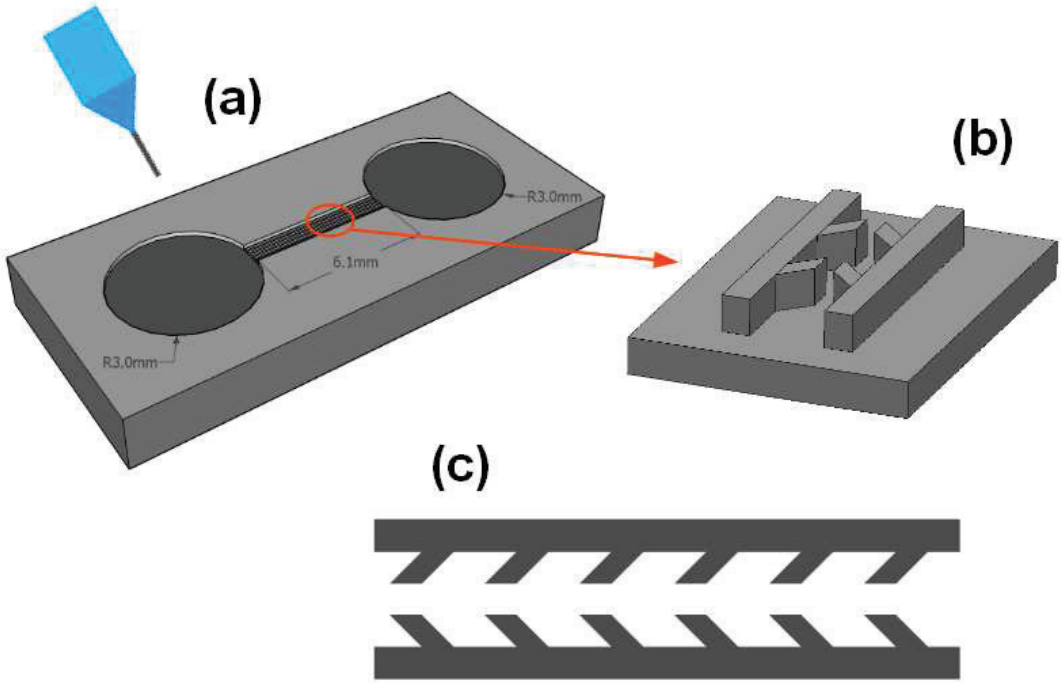

Figure 4.1. Schematics of asymmetric microfluidic channels. (a) A microfluidic device consists of ten parallel channels connecting two reservoirs. A syringe is used to deposit test fluids. (b) Zoom in on a small section of one of the tilted-fin decorated micro-channels. (c) Top view of an asymmetric micro-channel.

4.1 Introductions to Wicking in Microfluidic Channels

Dating as far back as ancient Egyptian and Mesopotamian times, the first irrigation canals marked the beginning of man's long-lasting endeavor to understand and control the flow of fluid. Years of experience, scientific study and engineering have taught us how to use gravity (constructing trenches, dams, and water towers) and mechanical forces (using pumps and pipes) to drive or, in some cases, to stop fluid flows. While these traditional schemes works very well within the gravity-dominated regime, the rapid growth of microfluidics in recent decades has triggered the need for new strategies of effectively control fluid flow at small scales, where surface forces dominate over gravity [Squires (2005)].

The basic idea behind microfluidics is to shrink the fluidics elements to micron size so that only very small quantities of samples or reagents are needed. Advantages that come with making the device small include: (a) the device can be relatively easily designed and made portable, versatile, and be massively produced; (b) there are existing printing and molding methods that provides simple and low-cost fabrication techniques for making such devices; (c) since many sensitive analysis apparatus are designed to take small quantities of samples, they are easier to be integrated into or combined with microfluidic devices than ordinary experimental fluidics setups; (d) widely-available, cheap, easy-to-use low-power small electronic and robotic micro-controllers, sensors, and actuators make it easy to automatize microfluidic devices. Holding promising prospects for efficient and economic automation and parallelization of fluid-based experiments, microfluidics has emerged as an important experimental platform in fields of chemistry, biology, medicine research, and material science [Burns (1998), Beebe (2002), Erickson (2004), Whitesides (2006)] − one that has the potential to revolutionize the experimentation practice of these fields. Research efforts are in high demand for microfluidics developments. The aim is to understand, utilize, and manipulate the behaviors of small quantities of fluids (typically on the order of nanoliter in volume) that are geometrically confined in micron-scaled channels, mixers, sorters, and reactors. The micrometer size-scale is the most important characteristics of microfluidics from the application standpoint as well as from the physics standpoint. In order to perform any basic operations within a microfluidic device, one must first be able to move the test fluid. This can be done actively with syringe pumps, or passively using capillary action [Laser

(2004), W. Gu (2004), Martinez (2008), Osborn (2010)]. At the size-scales of microfluidic channels, viscous and surface-tension effects dominate the behavior of the fluid. As a result, pressure-driven pumping of a fluid through a microfluidic or nanofluidic device can often be difficult. Surface tension, through capillary action or wicking, can be a powerful tool for transporting liquid within microfluidic devices. Moreover, the flow fields developed in microfluidic channels are almost always laminar (Stokes flow) mainly due to the their remarkably small characteristic length-scale (channel width). The ramifications of this type of low Reynolds number flows are (a) minimal inertial effects comparing to viscous effects − the moving fluids would appear to have little momentum, and their can be started and stopped rapidly. (b) form drags are very small due to the lack of recirculation. A number of interesting studies have appeared in the recent literature utilizing wicking to develop low-cost microfluidics platform suitable for chemical and biological sensing and diagnostics [Martinez (2008), Osborn (2010), Khan (2010), Martinez (2010), Ballerini (2011)]. These paper-based or thread-based microfluidics devices allow simple transporting and mixing functionality, but are unable to provide a high level of fluidic control

Chu *et al.* have demonstrated that uni-directional liquid spreading can be achieved on asymmetric structured surfaces [K. H. Chu (2010)]. Surfaces used in their study were decorated with an array of high-aspect-ratio hydrophilic micro-pillars all of which were bent in the same direction and at the same angle. Chu *et al.* also developed a theory to explain the uni-directional spreading behavior along the direction of the deflected pillars. This theory enabled them to make quantitative predictions of spreading asymmetry based on the combination of water contact angle and deflection angle of the pillars. Their findings opened up a new area of research targeted at discovering and understanding the links between structure and property via surface tension effects. Blow *et al.* have reported lattice Boltzmann simulation results that showed anisotropic imbibition of a fluid interacting with an array of hydrophilic polygonal prism structures [Blow (2009), Blow (2011)]. They found that the pinning of fluid front had direction dependency affected by the shape and orientation of the polygonal prisms and the array arrangement. Here in this study, we experimentally demonstrate one-way microfluidic channels whose working mechanism is based on a similar direction-dependent Laplace pressures but implemented with a different

set of structural geometries. A series of open microfluidic channels with specifically designed asymmetric internal structures were fabricated using standard photo-lithography and soft molding techniques. These micro-channels were shown to produce an asymmetric wicking behavior for a series of IPA-water mixtures. In some cases, the test liquids were found to completely wick in one direction while not wicking at all in the opposite direction. The wicking speed and degree of asymmetry was affected by the contact angle of the wicking fluid and the specific geometry of the angled fin-like structures added to the sides of the micro-channels. Surface-tension effects induced by the presence of the channels' internal structures were found to be the dominating physical mechanism responsible for the observed wicking behavior.

4.2 Fabrication of Microfluidic Channels

The experimental portion of this project consists of three major components: fabrication, characterization of structures, and characterization of properties. First, to fabricate the microfluidic devices, two main processes were involved: photolithography and soft molding [Duffy (1998), McDonald (2002)]. After the microfluidic channels were produced, their properties were characterized by wicking behaviors of a range of wetting fluids. Structural characterizations were performed both before and after wicking measurements.

Photolithography is a well-developed patterned replication technique widely applied in research and industry for micro- and nano-fabrications. For example, it is used in the fabrication process of most commercially available microprocessors nowadays. Intel and IBM have separately demonstrated the capability of achieving a resolution of 22-nm-node with using 193-nm-wavelength argon-fluorine (ArF) laser immersion photolithography. Photolithography uses light to transfer the predefined patterns on a photomask to a thin film of light-sensitive chemical known as photoresist. The basic mechanism which enables this technique is the photo-activated chemical reactions occur in the photoresist. There are in general two categories of photoresists: positive resists and negative resists. For positive resists, the same pattern as printed on the photomask will be formed on the resist layer after the lithographic process (hence "positive"). To do so, the regions of the resist layer that are exposed will become soluble in a weak solvent known as the developer, while the unexposed

portion remains insoluble in the developer. This can be due to, for example, the bond breaking excited by electromagnetic radiation which leads to reduction of molecular-weight and increase of solubility. For negative resists, the negative pattern of the photomask will be formed on the resist layer after the lithographic process (hence "negative"). To do so, the regions of the resist layer that are exposed will cross-link and become insoluble in the developer (which is usually a strong solvent for the uncrosslinked resist). Photolithography is usually performed inside a clean room facility to minimize the contamination due to dust particles in the atmosphere.

In this project, a standard SU-8 photolithography procedure was performed to generated molding masters with negative structures of the channels. SU-8 is a commonly used epoxy-based negative photoresist most sensitive to 365nm-wavelength ultraviolet (UV) light (commonly known as the i-line of the mercury emission spectrum). Materials and apparatus used in this process included: SU-8 2015 and SU-8 2050 resists from MicroChem, CEE 100CB spin-coater from Brewer Science, silicon wafers from WRS Materials, MA6 mask-aligner from SUSS MicroTec, HOYA U-350 filter from Newport Glass, plastic film photo-mask from CAD/Art Services, PGMEA ($\geq$ 99.5%) from Sigma-Aldrich. A typical photolithography process includes the following steps. First, a computer-aid–designed photomask was printed out by a high-precision ink-jet printer on a transparent plastic film. The mask-printing service was provided by CAD/Art. This plastic photomask will then be taped onto a piece of four-inch-square quartz glass with the patterned side facing out. Second, SU-8 2015 resist and SU-8 2050 resist were spin-coated onto clean silicon wafers to produce 22-μm-thick and 60-μm-thick SU-8 films, respectively. The spin-coated product then went through a soft-bake procedure at 95 °C , for 4 minutes (22 μm) and 6 minutes (60 μm). The third step was UV exposure. This is the most crucial step. Before each exposure, the light intensity of the UV lamp, which slowly drift in time, needs to be calibrated. Then the photomask (with the quartz backplate) and the SU-8 coated wafer were mounted onto their respective holders inside the mask-aligner. After the necessary alignments were performed, the patterns on the mask were projected onto the photoresist by UV light for a proper amount of exposure time calculated based on required dosages (thickness dependent). In the exposure step, a special light filter (HOYA U-350) designed to cut down the

unwanted portion of the mercury spectrum and select only a very narrow passband centered at 365 nm was applied so that more vertical sidewall profile can be achieved. Following the exposure step was the post-exposure-bake (PEB), where the acid-catalyzed crosslinking of SU-8 molecules took place, and then development, where the uncrosslinked portion of the resist was dissolved by the developer, PGMEA, leaving only the designed structures on the wafer. The PEB was performed at 95 °C, and the PEB duration and development duration was each 4 minutes (22 μm) and 6 minutes (60 μm). Finally, a hardening bake was carried out at 180 °C for 10 minutes. The spin-coating speed, soft-bake time, exposure dosage, post-exposure-bake time, development time, and the hardening-bake time all followed the corresponding instructions provided in the SU-8 processing guidelines sheet.

The second process of fabrication of microfluidic channels is silicone molding. Material used this process included Sylgard-184 silicone elastomer kit from Dow Corning and HMS-301 PDMS crosslinker from Gelest. In this process, part A (base) of Sylgard-184 was first thoroughly mixed with HMS-301 at an approximately 16:1 volume ratio. The mixture was then degassed in a vacuum chamber and slowly cast onto the masters that were individually seated in polystyrene Petri-dishes. The mixtures filled up to approximately 2 mm above the top surface of the masters. These Petri-dishes were then covered and left on a level platform for a slow curing at room temperature overnight (more than twelve hours) followed by a completion of curing at 80 °C for two hours. Finally, the samples were slowly cooled down and the silicone devices were carefully cut along the edge and separated from the SU-8 masters. A schematics for the complete fabrication procedure is shown in **Figure 4.2**.

4.3 Wicking Experiments and Discussions

In order to investigate how geometries of added structures can affect wicking, as well as to optimize the design for asymmetry of wicking, a series of microfluidic devices consisting of ten parallel micro-channels (length $\sim$ 6 mm) side-by-side with each end connected to a reservoir (diameter $\sim$ 6 mm) were fabricated. A schematic diagram of the microfluidic device is shown in **Figure 4.1**. A schematic diagram denoting the geometric parameters used for the photomask design is shown in **Figure 4.3**. **Table 4.1** lists the range of structural parameters used in the photo-mask design, as well as the optimized value for the

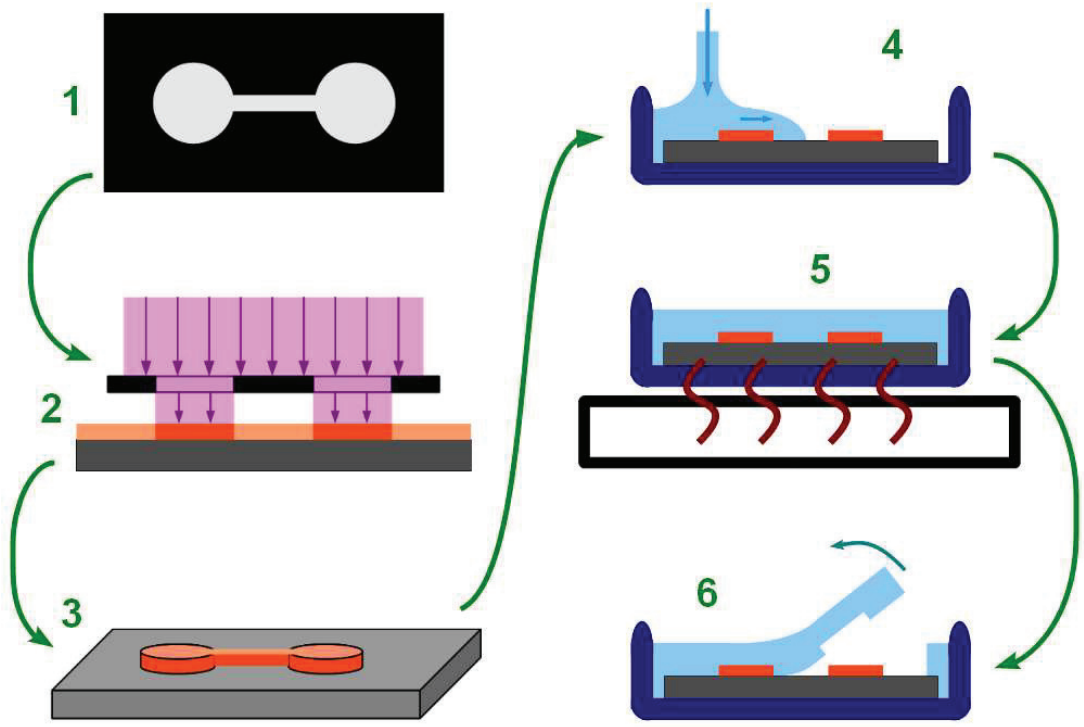

Figure 4.2. Fabrication of microfluidic devices via photolithography (left) and PDMS molding (right) processes. Steps including: (1) photomask designing and printing, (2) UV-photolithography, (3) formation of negative SU-8 structures, (4) applying the PDMS mixture, (5) heat-assisted cross-linking of PDMS, (6) peel-off.

Table 4.1. Values of the structural parameters of wicking devices studied. These parameters are defined in **Figure 4.3**.

Parameter	w [μm]	a [μm]	b [μm]	d [μm]	g [μm]	h [μm]	ϕ [°]
Range of Values	80 ∼ 90	20 ∼ 30	20 ∼ 40	100 ∼ 120	20	22 ∼ 56	27 ∼ 45
Optimized Device	80	20	40	120	20	56	27

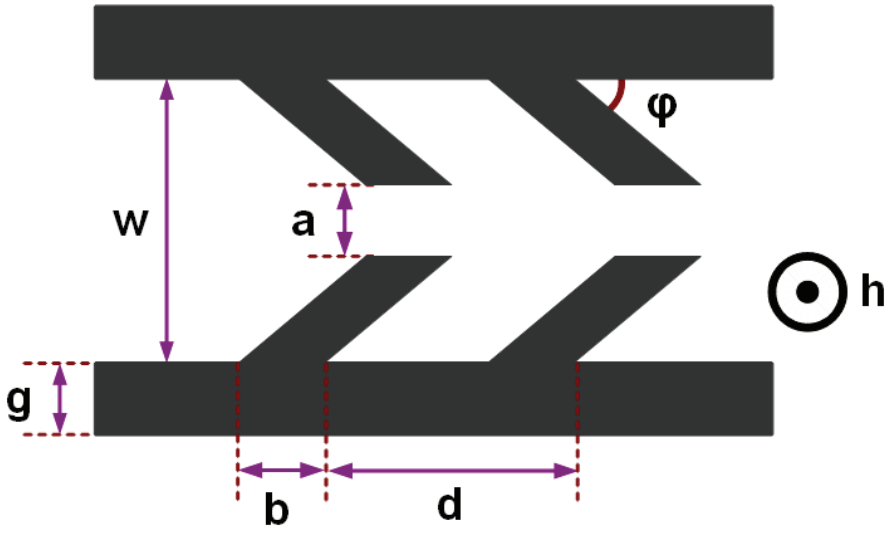

Figure 4.3. Schematic diagram of the geometric parameters for the photomask design. In this figure, only a top view of a small representative section of a single channel is shown with all relevant geometric parameters labeled.

device shown in **Figure 4.4** (SEM images) and **Figure 4.5** (optical microscope images). Although experimental data exist for all the designs outlined in **Table 4.1**, for brevity and clarity, only the results of the optimized channel are presented and discussed in detail here.

As seen in the representative images of the micro-structures shown in **Figure 4.4** and **Figure 4.5**, only small deviations of the fabricated structures were observed from the original photomask's design patterns. The height of the micro-structures on the device, as measured with optical profilometry and SEM imaging, was determined to be 56 ± 1 μm. For structural characterization before the wicking tests, ZYGO NewView^{TM} 7300 optical profilometer and Olympus BH2 Microscope with Infinity2 digital camera were used for optical profilometry and microscopy measurements, respectively. For structural character-

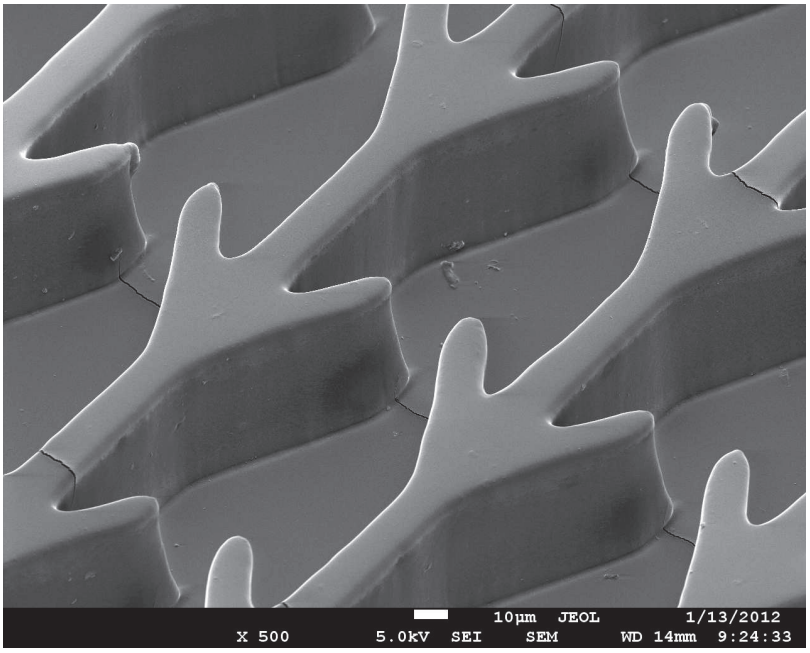

(a)

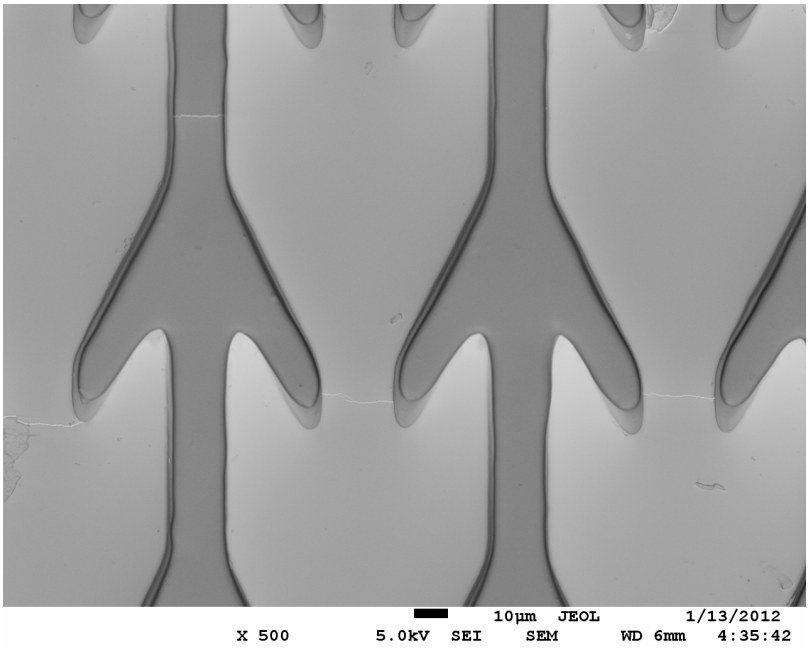

(b)

Figure 4.4. A 45°-view (a) and a top-view (b) SEM image of a small section of the microchannels on the actual PDMS device. The PDMS sample was first sputtered with a thin layer of gold before imaging.

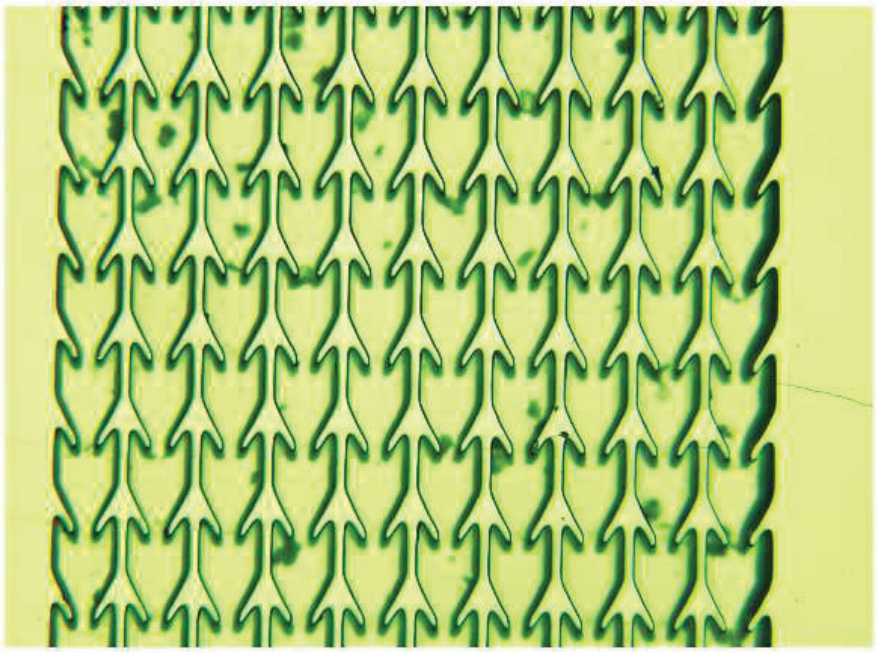

(a)

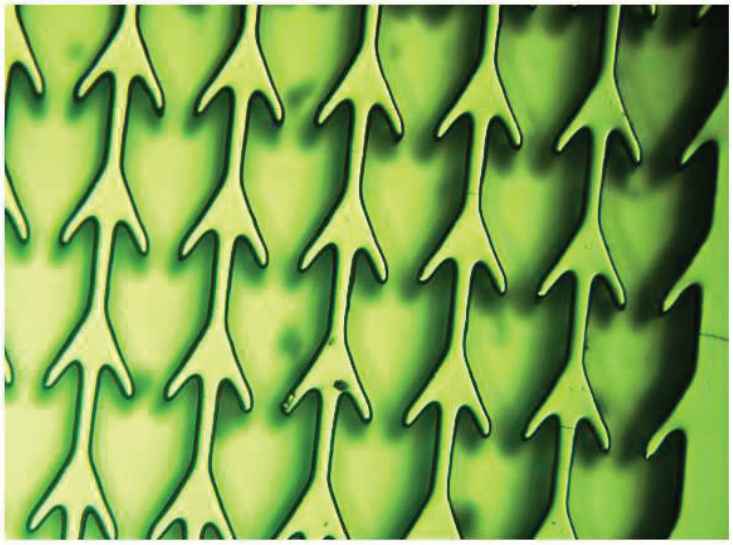

(b)

Figure 4.5. Optical microscope images of the PDMS micro-channels at (a) 100× and (b) 200× magnifications, both are top view.

ization after the wicking tests, the PDMS devices were first sputtered with a layer of gold ($\sim$ 50 nm) on the surface, using a Cressington 108 sputter coater from Ted Pella, then SEM imaging were performed using an JSM-7001F Thermal FE-SEM from JEOL at 5.0 kV acceleration voltage and approximately 160 pA current. Optical microscope images were also taken for comparison after SEM imaging.

Wicking tests were carried out directly on these open microfluidic devices. No additional surface treatment or sealing of the top of the device were performed prior to the tests. In a wicking test, a PDMS device was first cut and carefully placed on a piece of clean glass slide. After the device surface were cleaned with RO-water and dried with compressed air, the glass slide (with device on top) was then placed on top of a leveled diffused light source. EO-1312C CMOS Color USB camera from Edmund Optics with a 50mm spacer and a V5018 video lens (50 mm, F/1.8) from Computar was setup above the device at a $35^\circ \sim 45^\circ$ angle from horizontal and in the vertical plane perpendicular to the micro-channels. A precise amount of test fluid was slowly deposited onto the reservoirs and allowed to spontaneously spread into the microchannels. The deposition of test fluid was performed at a constant speed with a syringe pump setup based on a KDS100 syringe pump from KD Scientific. Total duration of the fluid deposition was between 1.5 s $\sim$ 3.0 s depending on the target volume. All experiments were done under room temperature of 21.0 $\pm$ 2.0 °C. PDMS is mildly hydrophobic with an advancing contact angle of $\theta_{water} \approx 102^\circ$, but PDMS is wet by IPA which has a contact angle of $\theta_{IPA} \approx 33^\circ$. Mixtures of IPA and RO-water were made with advancing contact angles between those two limits to systematically probe the effect of contact angle on wicking rates and degrees of asymmetry. Materials and consumables used in the wicking test include: Isopropyl alcohol ($\geq$ 99.9%) from Fisher Scientific, Ro-water from a Millipore Milli-Q system, 1-mL Norm-Ject disposable syringes from Henke-Sass Wolf, Intramedic polyethylene tubing from Clay Adams.

The initial experimental demonstration of asymmetric wicking in our "microfluidic diodes" was performed with a mixture of 80% by volume IPA and 20% RO-water as the test fluid. In **Figure 4.6**, two time-lapse images are presented side-by-side to show the test fluid wicking through the micro-channels in opposite directions. These images represent two separate experiments. In each case, the volume of deposited fluid was set to be 15.0 μL.

As seen in **Figure 4.6**, the wetting behavior of an identical fluid can be quite different depending on which direction it wicks. On the left-hand-side, the wetting fluid spread rapidly along the channels, and within ten seconds, the fluid covered the entire length of the micro-channels. We denote this as the easy wetting direction because a wetting fluid can spread easily. On the right-hand-side, the same wetting fluid hardly penetrated into the channels because its spreading front was strongly pinned at the corners of the tilted fins added near the entrance of the micro-channels. We denote this as the hard wetting direction. Experiments with 20.0 μL, 25.0 μL, 30.0 μL test fluid were also performed to determine whether varying the amount of test fluid deposited onto the reservoir had an effect on the one-way wicking behavior. It was found that, as long as the overflow was subtracted as background, the speed and distance a given fluid front wicked into the channel was independent of drop size in the reservoir. During the entire study, care was taken to ensure that the wicking experiments in opposite directions of the same set of micro-channels were performed under consistent conditions, so that valid comparisons could be drawn. Specifically, the PDMS devices were cleaned and dried with the same procedure before each tests, the same amount of test fluids were deposited with the same manner, and the temperature, lighting, and air flow conditions were kept as consistent as possible. To examine repeatability of the wicking behavior, multiple experiments with identical experimental parameters were performed and compared. Moreover, multiple devices duplicated (negatively) from a single SU-8 master wafer were also tested and compared. No difference of statistical significance was observed in either set of comparisons.

The effect of surface tension in a fluid system is exhibited in the form of the Laplace pressure. Mathematically, the magnitude and direction Laplace pressure can be calculated by knowing the local curvature of a given point on a surface. This indicates that balancing of surface forces or minimization of surface energy is intrinsically a geometry problem. As a result, because the fluid dynamics is dictated by forces, it is possible to use the geometric design of the micro-channels to control the wicking behavior of our test fluid. The key concept in this physical model is the recognition that, at small characteristic length-scale (i.e., the width of the micro-channels), the interfacial forces are large comparing to inertial forces and gravitational forces. The Reynolds number for our systems was small,

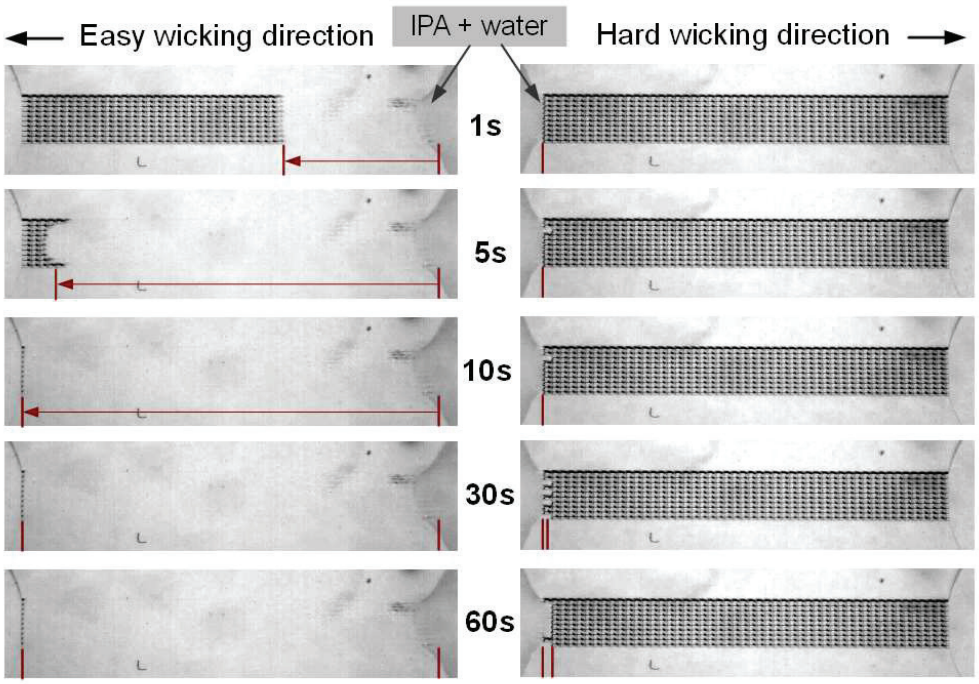

Figure 4.6. Time-lapse images of wicking of the same fluid, 80% IPA + 20% H_2O solution, on opposite directions along the same set of micro-channels demonstrate one-way wicking behavior of the system. In both cases, the fluid front wicked from the center outward.

$Re_{max} = \rho V w/\mu \approx 0.4$. The capillary length, which is ${\kappa^{-1}}_{min} \approx 1.5$ mm for the IPA water mixtures, is large compared to the dimensions of the features in the micro-channels. For these calculations, $\rho = 1.0 \times 10^3$ kg/m^3 and $\mu = 1.0 \times 10^{-3}$ Pa·s are the mass density and dynamic viscosity of water, $\gamma = 22 \times 10^{-3}$ N/m is the surface tension of isopropanol, $w =$ 80 μm is the width of the micro-channels and $V_{max} = 1.0$ cm/s is the estimated maximum velocity of the fluid.

The one-way wicking phenomenon explored in this study resulted from the ability of the micro-structured channels to locally impose different boundary conditions on the fluid front (or meniscus) in opposite spreading directions. In **Figure 4.7**, a simplified two-dimensional (2D) model is presented which can be used to qualitatively explain this mechanism. In this figure, the strength and direction of the Laplace pressure at each stage is represented by the length and direction of the arrow placed at the corresponding moving contact line. Here we assume that a wetting fluid meets the device surface at a constant advancing contact angle, which is less than 90°. The spreading of this fluid can easily continue in either direction when the front is in the straight section connecting the tilted fins (**Figure 4.7** (a) and (d)) or when it is at the narrow opening (**Figure 4.7 (b)**) between the tilted fins on opposite walls because the curvature of the meniscus in these cases is negative. This results in a Laplace pressure aligned in the flow direction. This is also true as the meniscus moves along the upstream side of the tilted fins as shown in **Figure 4.7 (e)**. However, when the fluid front gets to the downstream side of the tilted fins in **Figure 4.7 (f)**, it must form a convex meniscus in the hard wicking direction. This results in a Laplace pressure that resist further spreading and pins the contact line. In the easy wicking direction, the shape of the meniscus downstream of the tilted fins shown in **Figure 4.7 (c)** can be either concave or convex depending on whether the sum of the tilting angle, ϕ, and the contact anle, θ, is less than or greater than 90°. Consequently, with simple addition of a tilted-fin geometry to an open micro-channel, this 2D model demonstrates how asymmetric wicking can be achieved. As we will see later, this simple 2D model cannot quantitatively explain all our observations. In some cases, 3D effects must be considered.

In order to investigate the effects of wettability on asymmetric wicking of fluid through our micro-channels, the contact angle between the test fluid and the PDMS surface was

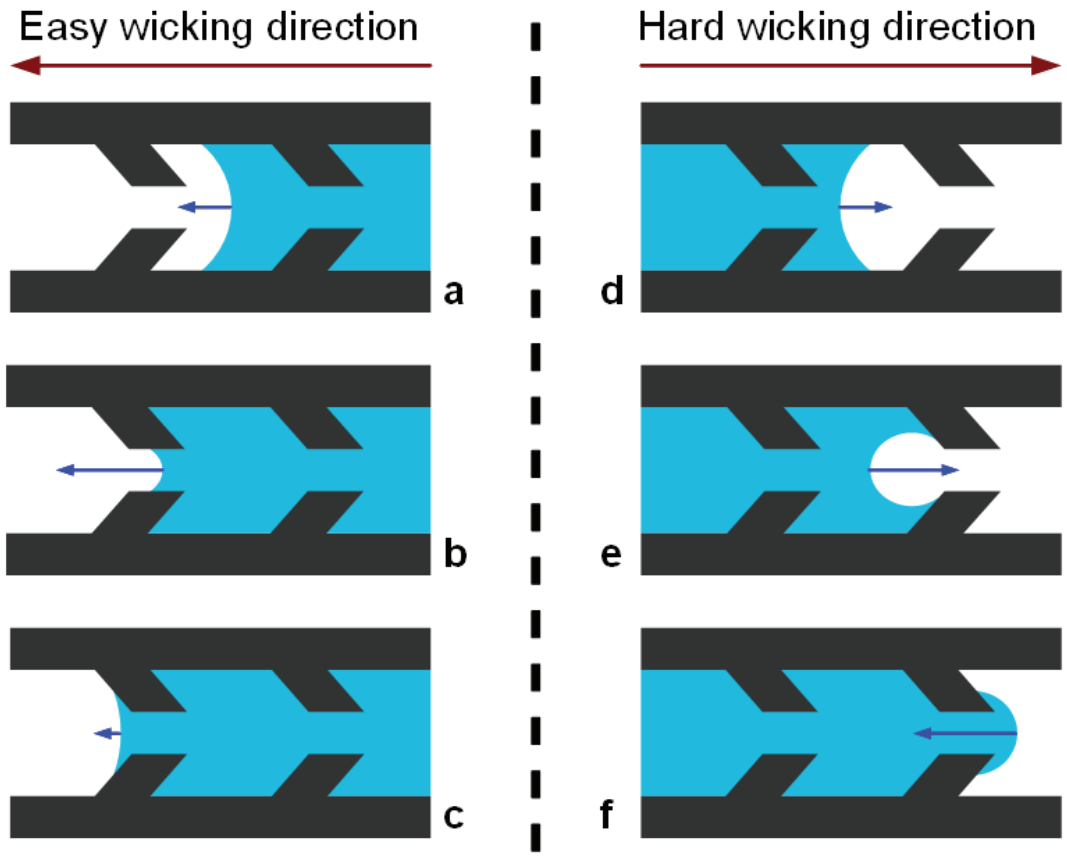

Figure 4.7. Schematic diagrams of the asymmetric wicking mechanism based on a simplified 2D model. The arrows represent the strength and direction of the Laplace pressure at each stage. The easy direction (a, b, c) and the hard direction (d, e, f) of wicking are compared side-by-side.

tuned by varying the mixing ratio of IPA and water. At IPA volume ratio $\Phi_{IPA} > 50\%$ range, the surface energy of the mixture is dominated by Van der Waals interaction, and the contact angle of the IPA-water mixture on PDMS can be roughly estimated by:

$$\cos\theta = 2\sqrt{\gamma_{PDMS}/\gamma_{mixture}} - 1. \tag{4.1}$$

The dependence of the surface tension of IPA-water mixture on IPA volume ratio is highly non-linear [Vazquez (1995)], the power index can be estimated to be roughly -2. If that is the case, it is anticipated that $\cos\theta \approx C_1\Phi_{IPA} + C_2$, where C_1 and C_2 are coefficients independent of Φ_{IPA}. The specific values of contact angles were experimentally measured and are presented in **Figure 4.8**. As shown in this figure, the cosine of the contact angle, $\cos\theta$, was found to increase linearly with increasing IPA concentration in the mixture. Based on our simplified 2-D model, it is expected that the fluid will not spread in the hard wicking direction due to the positive-definite curvature of the meniscus, but the spreading of the fluid in the easy wicking direction can be controlled by the amount of IPA in the mixture. For a more detailed understanding of the wicking dynamics, plotted in **Figure 4.9** are the spread distances as functions of time for three IPA-water mixtures – 60%, 80%, 90% IPA volume ratio, respectively – on the microfluidic device described in **Table 4.1**. Notice in the easy wicking direction, both the 80% IPA and the 90% IPA solutions wicked through but the wicking of the 60% IPA solution stopped midway in the micro-channels; in the hard wicking direction, only the 90% IPA solution wicked through, both the 60% IPA and the 80% IPA solution did not wick. It was found that, on this device, under open atmosphere, at least partial wicking was allowed on the easy direction for IPA percentage above 40%. Spreading was stopped on the hard direction unless IPA ratio was above 85%. Generally, the wicking speed on the easy direction decreases with decreasing IPA ratio of the mixture, because a lower IPA ratio corresponds to a higher contact angle and consequentially a smaller driving force that comes from a lower Laplace pressure. With a total channel length of approximately 6 mm, it took between 5 seconds and 20 seconds for a test fluid with IPA ratio higher than 70% to wick through.

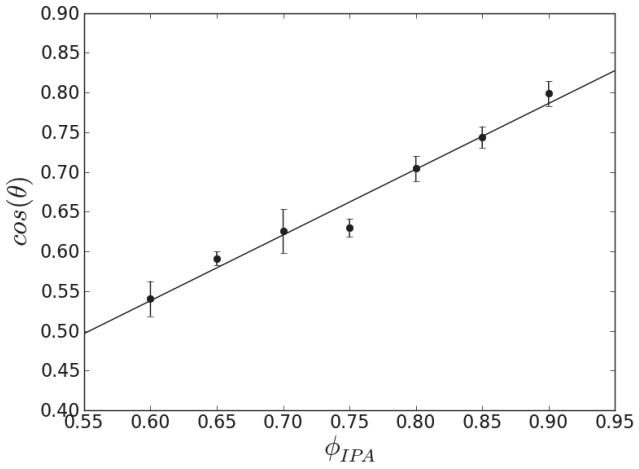

Figure 4.8. Contact angle between test fluid and PDMS surface varies as a function of IPA volume ratio.

Based on the data presented in **Figure 4.9**, it is clearly that the speed of wicking in the easy direction decreased as the fluid front advanced. A log-log plot of the data presented in **Figure 4.10** shows a power-law dependence of the wicked distance with time. At long times, the characteristic power index for all the fluids converge to within the range of 0.55 $\sim$ 0.60. This can be explained by a simple model of capillary action under the absence of gravity. Here a laminar channel flow is driven by a constant Laplace pressure, so the pressure drop across the length of the fluid column inside the capillary should be inversely proportional to the length of the column, L. Based on the Poiseuille equation, this pressure drop is proportional to the volumetric flow rate, or front velocity, V. Therefore,

$$V = \frac{dL}{dt} \propto \frac{1}{L}, \tag{4.2}$$

which gives $L \propto \sqrt{t}$. This means that the length of the wicking fluid column should grow as the square root of time, which is close to the scaling observed in the experiments. The small discrepancy in the characteristic power indexes between experimental extraction and theoretical prediction is likely due to measurement errors.

One question that needs to be addressed is why the 60% IPA solution only spread halfway down the micro-channels in the easy wicking direction before stopping. The simplified 2D

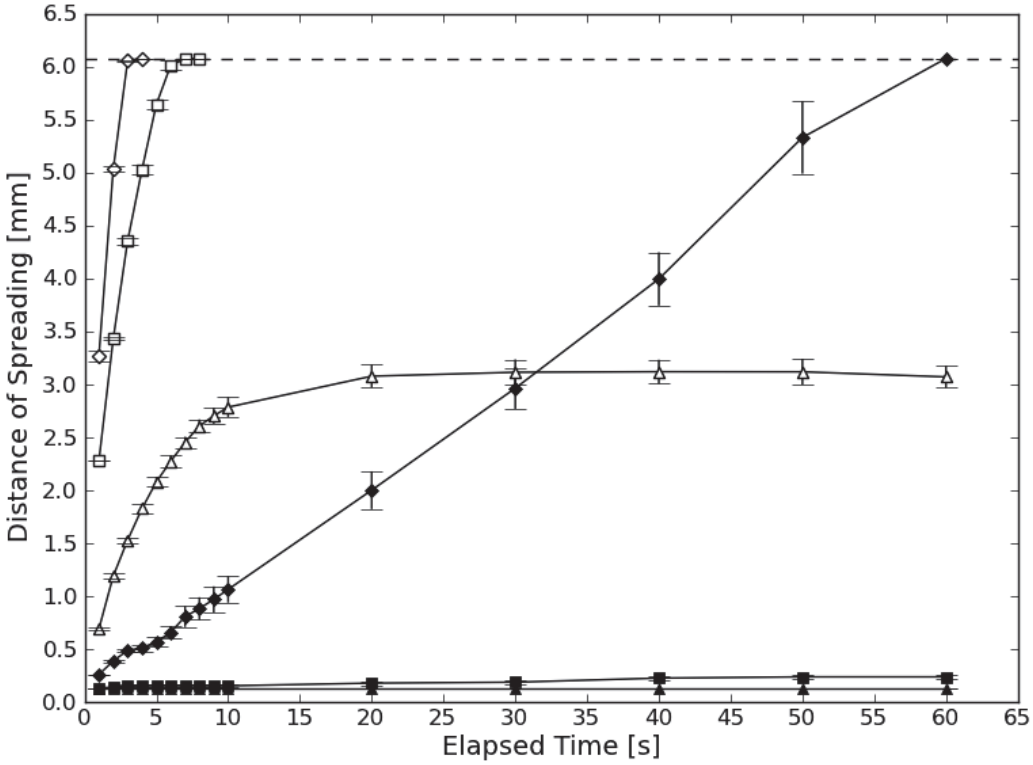

Figure 4.9. Distance of spreading as a function of time for a series of different IPA-water mixtures. The data include: 60% IPA (triangle, △), 80% IPA (square, □), 90% IPA (diamond, ◇) test fluids on the device described in **Table 4.1**. All experiments were performed open to atmosphere. The open symbols represent wicking in the easy direction and the closed symbols represent wicking in the hard direction. The dashed-line indicates the total length of the channels.

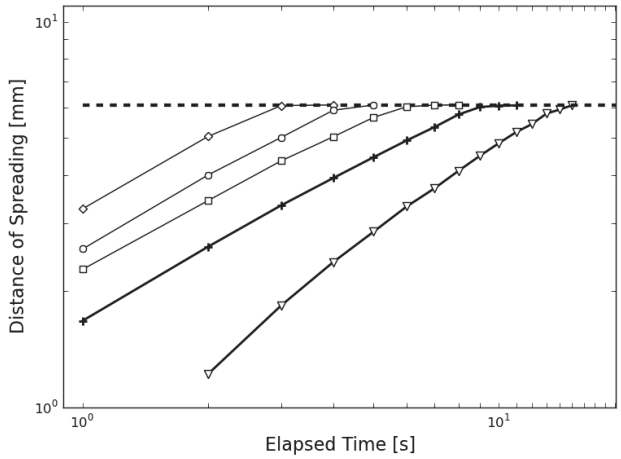

Figure 4.10. Wicking on the easy direction shown at a log-log scale. The dashed-line indicates the total length of the channels. Slopes of the fit-lines varied between 0.55 and 0.60 for the 80% IPA (□), 85% IPA (◯), and 90% IPA (◇) test fluids under open atmosphere, and at long times for the 70% IPA (+) and 60% IPA (▽) test fluids under vapor saturated environment.

model would suggest that if a fluid could initially wick into a structured micro-channel, it should be able to wick all the way through the channel. Assuming the volume of fluid removed from the reservoir is small, which it is. This discrepancy between 2D theoretical prediction and experimental observation clearly indicates one or more important components are missing in the model. The two primary physical components that our 2D model ignores are the effect of evaporation, specifically the evaporation of the IPA, and the 3D effects at the leading edge of the spreading meniscus. The effects due to evaporation of the test fluid were examined by comparing open experiments to those performed in a solvent rich environment. For experiments in closed atmosphere, the whole glass slide on which the PDMS microfluidic device was placed was covered with a transparent Polystyrene Petri-dish with drilled holes for needle access. As shown in **Figure 4.11**, the environmental conditions can have a large impact on spreading. In experiments where the 60% IPA test fluid was allowed to spread in the easy wicking direction, under an open atmosphere, the test fluid was observed to wick only half-way through the channels. If, however, the PDMS device was covered with a Petri-dish inside which the environment was saturated with equilibrium vapor of the same IPA and water mixture, the same 60% IPA test fluid was found to wick

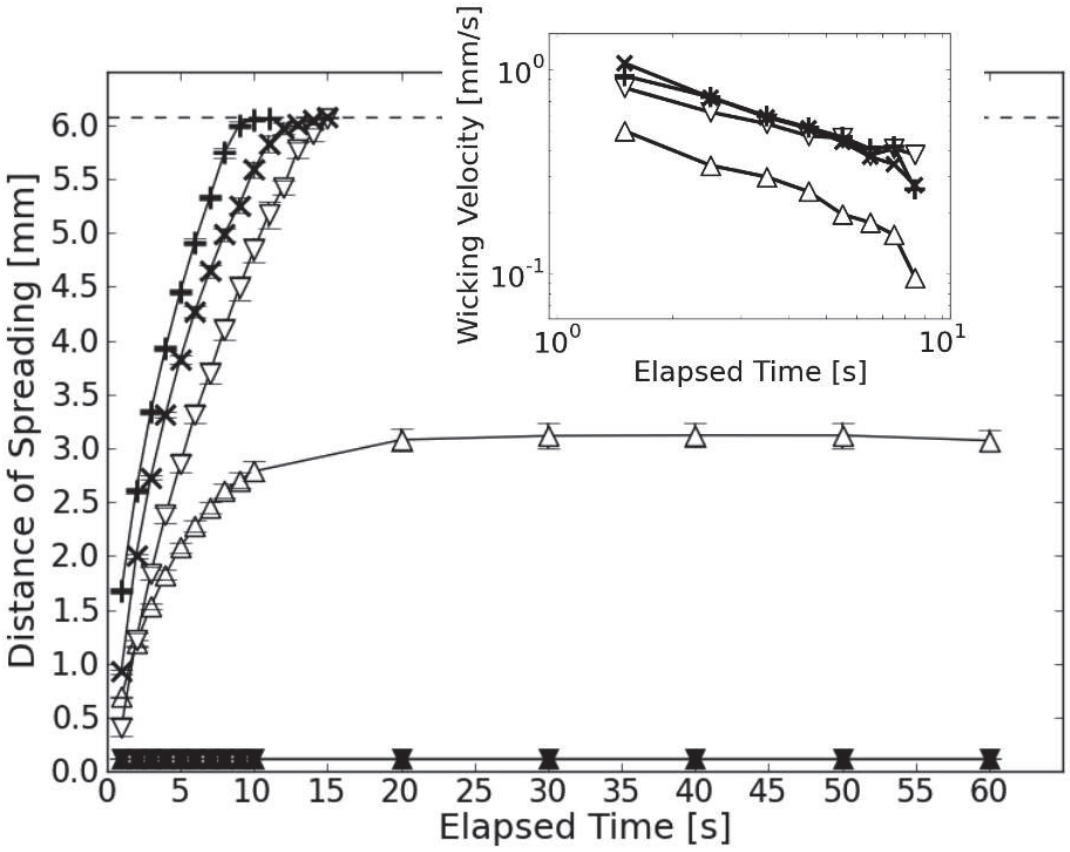

Figure 4.11. Distance of spreading of the wicking front as a function of time. The dashed-line indicates the total length of the channels. This plot quantifies the wicking process of 60% IPA fluids under open (△) and closed (▽) atmosphere, and 70% IPA fluids under open (×) and closed (+) atmosphere for the microfluidic device described in **Table 4.1**. The wicking velocities (in log-log scale) are presented in the inset. The velocity data is all found to scale roughly as $V \propto t^{-0.5}$.

completely through the micro-channel array. In experiments where the test fluid IPA ratio was 70%, covering the PDMS device increased the wicking speed. These experiments confirmed that the higher evaporation rate of IPA compared to water leads to lowering of IPA concentration locally at the fluid front. The increase contact angle results in a transition from a concave to a convex meniscus causing the propagation of the fluid front to stall. It was found by experiment that, under a solvent vapor saturated environment, a test fluid of 40% IPA could wick into the micro-channels while a test fluid of 35% IPA could not wick into the channels at all.

As shown in **Figure 4.9**, the 90% IPA test fluid was observed to completely wick through the micro-channels in both the easy and the hard wicking direction. The entire wicking process took about 60 seconds in the hard wicking direction compared to about 5 seconds in the easy direction. Other than wicking asymmetry, this is another example of how the simplified 2D model, while in many cases is adequate for explaining qualitative trends, misses out on some of the important aspects of physics. This observation is not a result of evaporation, but rather a case where 3D effects need to be taken into account. To obtain a more accurate quantitative prediction of the wicking behavior, 3D simulations based on the Surface Evolver were employed [Brakke (1992), Y. Chen (2005)]. Two representative 3D menisci obtained from the simulations, one spreading in the easy wicking direction and the other spreading in the hard wicking direction, are shown in **Figure 4.12**. In general, the shapes of the 3D menisci computed by simulations are not fundamentally distinct from what were expected using the 2D model. The major difference is the a sloped front profile on the vertical plane as a result of the micro-channel having a wet, solid bottom and a top open to air. In most cases, these differences are not enough to keep the simplified 2D model from providing satisfactory qualitative predictions consistent with the experimental observations of asymmetric wicking behaviors. There are, however, a number of limiting cases where predicting the 3D characteristics of the meniscus is critical to understanding the observed wetting behavior. One such case is a special example of Plateau-Rayleigh instability under geometric confinements which occurs where the vertical walls meet the floor of the micro-channels. This instability has been examined in a number of previous studies and is known to occur at a critical combination of geometry and contact angle [Brakke (1996), Rejmer (1999), Finn (2002), Kitron-Belinkov (2007)]. For a 90° wedge, with side-walls exactly perpendicular to the floor, the critical contact angle is 45°. Below this angle, the fluid will wick indefinitely along the wedge. The critical contact angle decreases as the inner angle of the wedge increases. One of the ramifications of this instability is that it enables wicking on the hard direction for fluids with relatively low contact angles even though our simplified 2D model would exclude it. As shown in **Figure 4.12**, this is because the Plateau-Rayleigh instability allows the meniscus to extend along the lower front corners of the micro-structures. When the meniscus reaches the inside wall of the channel, the

boundary condition is altered to one which favors forward wicking and the front moves down the channel to the next feature, albeit relatively slowly.

So far, all the discussions have been based on the same device structure whose geometric parameters are listed in **Table 4.1**. In these experiments, the only parameter that has been varied was the contact angle and interfacial tension. The next step was to investigate the effects of variation of each geometric parameter of the device structure on the wicking behavior. A range of geometric parameters tested are presented in **Table 4.1**. Qualitatively, it was observed that lowering the height, h, of the structures to $h = 22$ μm, while keeping other parameters the same, led to a lower degree of wicking asymmetry by both promoting wicking on the hard direction and diminishing wicking on the easy direction. This agrees with the intuition that 3D effects are more pronounced on structures with lower aspect ratios, because the Laplace pressure is dictated by the mean curvature, which is dictated by the two principle curvatures. Moreover, a smaller value of opening width, a, led to a higher degree of wicking asymmetry, as one would predict based on the simplified 2D model. In terms of the tilting angle, ϕ, on one hand it is better to have smaller tilting angle to induce a large front curvature difference between opposite spreading directions, but on the other hand, the 3D effects makes it necessary to also consider the spacing between consecutive fins along the micro-channels and between the fins and the side-wall of the channels. This restricts tilting angle within a certain range based on the values of the other geometric parameters d, a, and w. We observed that a 27° tilting angle produced larger wicking asymmetry, in terms of the extend and speed, than a 45° tilting angle in most cases.

The capability of precisely calculating the 3D meniscus shape (by using simulations based on the Surface Evolver) allows for a model that can more accurately predict the wicking behavior. To establish this model, we examined the easy and hard wicking directions separately. First, in the hard direction, it has been explained previously that the Plateau-Rayleigh instability causes any fluid with contact angle (to the PDMS surface), θ_{mat}, lower than 45° to wick through. This critical contact angle is only affected by the angle at which the fin-like structures meet the bottom of the channel. For fluids with θ_{mat} higher than 45°, simulations has been performed with the channel height fixed at 55 μm, and the resulted are listed in **Table 4.2**. In **Table 4.2**, it is shown that for a fin-tilting angle of 90°, whenever

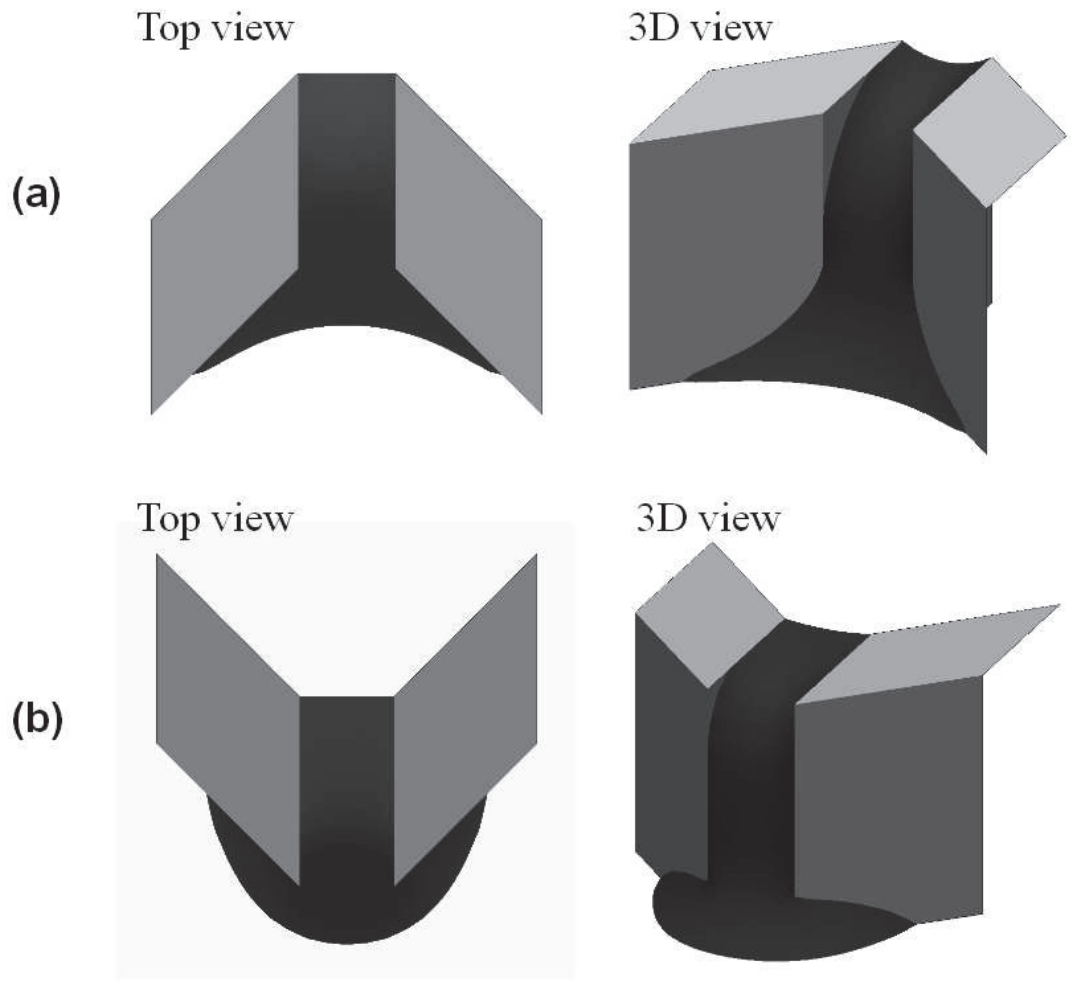

Figure 4.12. Representative 3D menisci (shown in dark color) resulted from Surface Evolver simulations of a wetting fluid ($\theta = 40°$) at the opening between tilted arms on opposite sides. A top view and a 3D view of the menisci formed when the fluid spreads on (a) the easy wicking and (b) the hard wicking directions are included.

θ_{mat} is greater than 50° the fluid does not propagate (denoted as recede, or "rec", in the table). This indicates that on the hard direction, if θ_{mat} is greater than 50°, the fluid does not propagate, because it is harder for a fluid to wick in the hard direction than under a 90°tilting angle. It should be mentioned that the criterion on which advance / recede was determined in the simulations was whether the system energy decreased (corresponding to advance) or increased (corresponding to recede) as the volume of fluid increased (by 1% $\sim$ 5%). Second, on the easy direction, again, for θ_{mat} below 45°, fluid always wick. For θ_{mat} above 45°, under fixed channel height, the wicking behavior is predicted to be mainly controlled by the tilting angle of the fins, ϕ. Results shown in **Table 4.2** suggest that the projected (from the top view) contact angle, θ_{proj} (schematically defined in **Figure 4.13**), is mainly influenced by θ_{mat} and rather insensitive to ϕ, i.e., a certain θ_{mat} always produces very similar θ_{proj} across many different ϕ values. This can be explained by the fact that, when zoom in close enough to the corner where the propagating front meets the tilted fin, the tip of the fluid forms a tetrahedron (because the local curvature of any point on the meniscus has to be finite), as shown in **Figure 4.14 (a)**. The shape of this tetrahedron only depends on θ_{mat}, and once the shape is determined, θ_{proj} can be calculated as:

$$\cos\theta_{proj} = \frac{1}{\tan\theta_{mat}} = \frac{\cos\theta_{mat}}{\sin\theta_{mat}}. \tag{4.3}$$

As shown in **Figure 4.14 (b)**, good agreements can be demonstrated between the simulation results and the analytical solution. Based on this equation, some θ_{proj} are calculated and listed in **Table 4.3** for reference. In the 2D model represented by **Figure 4.7**, the dynamics of the wetting fluid on the easy wicking direction is controlled by the sum of ϕ and θ_{mat}. Taking into account the 3D effect, θ_{mat} should be replaced by θ_{proj}. The combination of ϕ and θ_{proj} can be represented by the front forward angle, ω, as shown in **Figure 4.13**, and the advance / recede criterion, from the 2D viewpoint, becomes whether ω is less or greater than 0°. Clearly, this criterion is only true when the meniscus has zero curvature on the vertical direction. Based on the results listed in **Table 4.2**, a strong correlation between the ω values and the fluid behavior (whether or not advance) can be concluded. This indicates that, under a fixed channel height, the curvature on the vertical direction is

Table 4.2. Results of 3D simulations for investigating effects of tilting angles on the wicking behavior. Results include the projected contact angle, θ_{proj}, the front forward angle, ω, and the wicking behavior (advance or recede).

ϕ	90°	90°	90°	90°	90°	60°	60°	60°
θ_{mat}	50°	60°	65°	70°	75°	50°	60°	70°
θ_{proj}	33°	54°	60°	66°	72°	34°	54°	67°
ω	33°	54°	60°	66°	72°	4°	24°	37°
Adv. / Rec.	rec	rec	rec	rec	rec	adv	rec	rec
ϕ	45°	45°	45°	45°	30°	30°	30°	
θ_{mat}	50°	55°	60°	70°	50°	60°	70°	
θ_{proj}	33°	46°	55°	69°	34°	55°	68°	
ω	−12°	1°	10°	24°	−26°	−5°	8°	
Adv. / Rec.	adv	adv	rec	rec	adv	adv	rec	

Table 4.3. Results of θ_{proj} calculated for a range of θ_{mat} based on the analytical solution (**Equation 4.3**).

θ_{mat}	50°	55°	60°	65°	70°	75°	80°
$\theta_{proj,cal}$	33.0°	45.6°	54.7°	62.2°	68.7°	74.5°	79.8°

approximately unchanged. The effect due to this vertical curvature is shifting the advance / recede criterion from $\omega = 0°$ to $\omega = 6°$ by estimation. From this set of simulation results, it is clear that the 2D model captured most of the qualitative trends, and the 3D model provides improvements for the quantitative predictions.

4.4 Conclusions of the Wicking Channel Project

The ability to passively control the spreading of fluids is of tremendous importance in the development of efficient microfluidic devices and in the understanding of flow within them. In this chapter, we introduced a new type of open microfluidic channels that are capable of producing asymmetric wicking with a wide range of wetting fluids. This "microfluidic diode" behavior is based on direction-dependent Laplace pressure induced by asymmetric structures. Specifically, an array of ten parallel micro-channels were fabricated with the addition of periodic tilted fins that extended into the channels at a specific angle and period. A mixture of IPA and water introduced from a reservoir was shown to rapidly wick through the channels only in a predefined direction. The pressure-driven nature of this fluid flow was

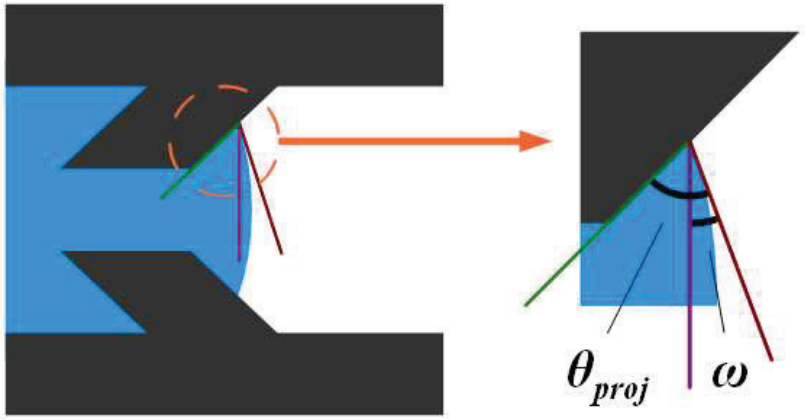

Figure 4.13. Schematics of the projected contact angle, θ_{proj}, and the front forward angle, ω, from the top view.

verified by studying the time dependence of wicking distance. Spreading of the same fluid in the opposite direction was completely prohibited by the presence of the tilted fins. Detailed examinations of the basic mechanism which produces this effect were predicted by a simple 2D theory and investigated in depth by full 3D simulations. We found that for test fluids of many different IPA-water mixing ratios, the simplified 2D model was adequate to provide qualitative predictions. For test fluids with low IPA ratios, evaporation effects that led to changing of composition needed to be included in the mechanism. For test fluids with high IPA ratios, Plateau-Rayleigh instability of the 3D fluid system can quantitatively modify the wicking behavior. Multiple physical, chemical, and geometric parameters were varied to systematically study their individual effects on the wicking behaviors. It was found that a lower fin-tilting angle, a larger fin length or a smaller opening width, and a larger structure height all resulted in a higher degree of wicking asymmetry.

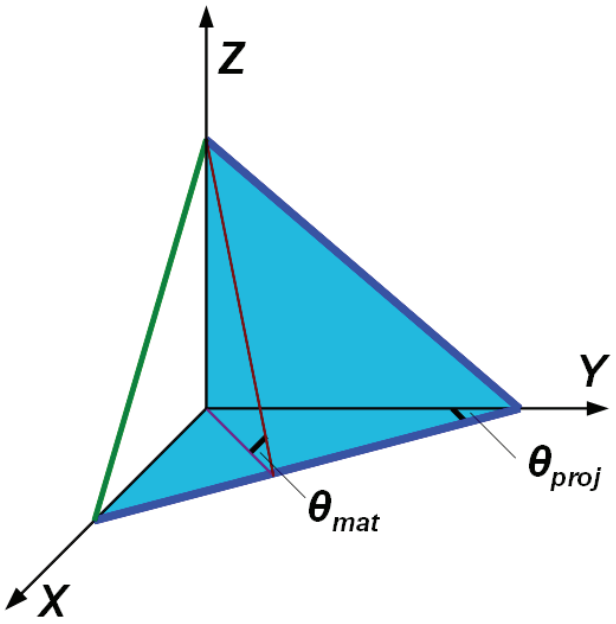

(a)

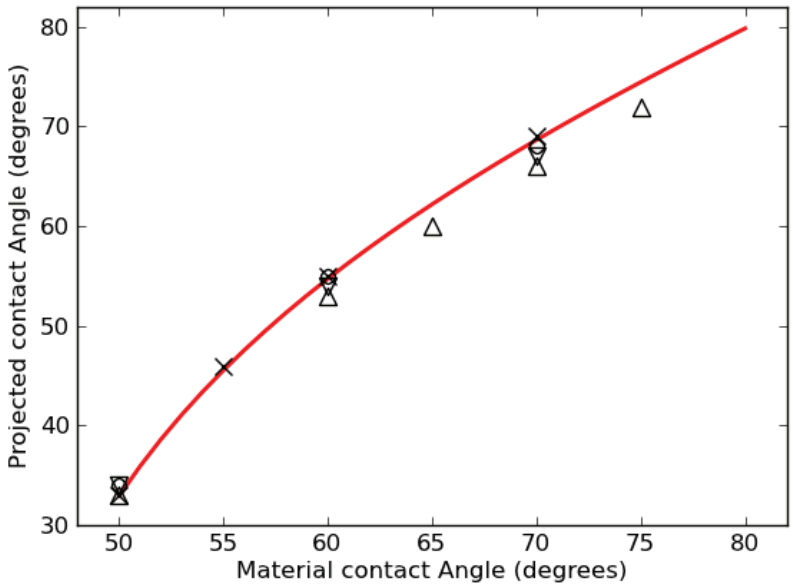

(b)

Figure 4.14. Calculation of projected contact angle, θ_{proj}. (a) Schematics of the tetrahedron formed at the tip of the advancing front. (b) Comparisons of the analytical solution (solid line) and the results of Surface Evolver simulations (scattered symbols).

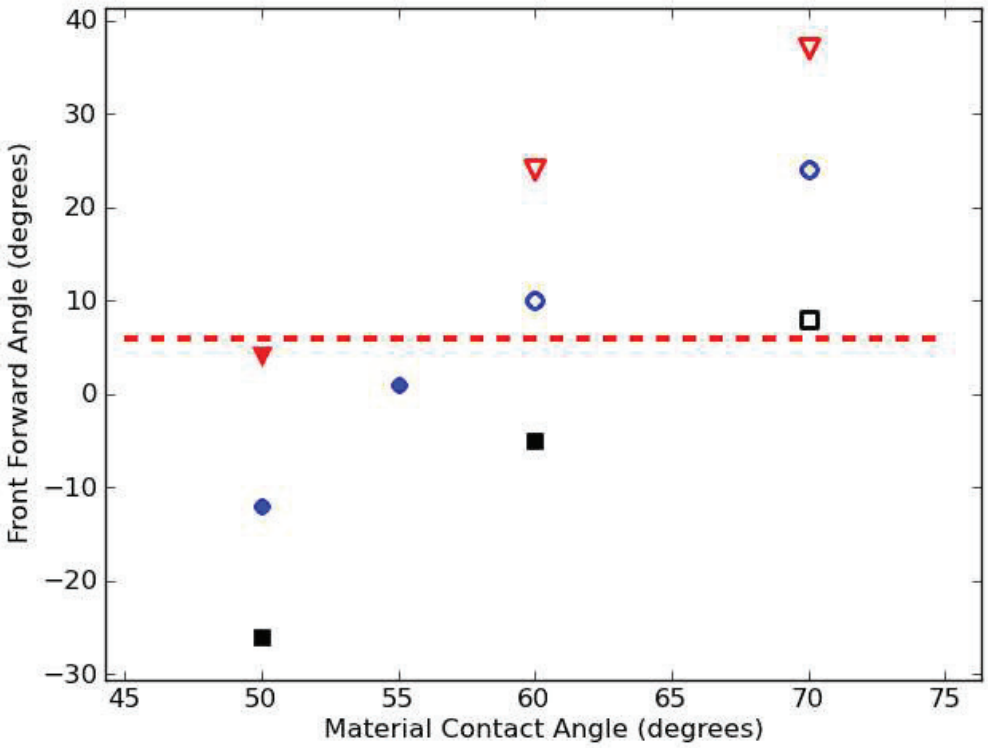

Figure 4.15. Plot of the front forward angle, ω, as a function of the material contact angle θ_{mat} for fin-tilting angle of 60° (▼), 45° (●), and 30° (■). Solid symbols denote spontaneous advancing while hollow symbols represent cases where the fluid front does not propagate. The dashed line corresponds to $\omega = 6°$, which is the estimated division between the advancing and the receding cases.

CHAPTER 5
CONCLUSIONS

It is important to study surface-tension effects, because they dominate small-scale fluid systems. My research on surface-tension effects mainly consists of three projects. They are presented in previous chapters of this dissertation. In these three projects, we have, simply put, modeled a type of systems (**Chapter 2**), produced a type of surfaces (**Chapter 3**), and designed a type of devices (**Chapter 4**). The specific findings of each individual project have been concluded in their respective chapters. These findings are not isolated pieces of information, they are connected by surface tension in principle, and by the menisci (free surface of fluids) as the media. Our starting point was the lotus effect. It is believed that, in order to support a large shear-free water-air interface, a hierarchical structure is crucial, so our first goal was to make hierarchical surfaces. We first attempted using the menisci formed in specially shaped capillaries to produce hierarchical structures. Although we could understand and quantify the shape of the menisci in great details with the help of simulations, the products of CFL experiments failed to preserve high-aspect-ratio structures useful for studying the lotus effect. Then we experimented with EBL and successfully demonstrated fabrication hierarchical structures with full and partial coverages of secondary features. With these hierarchical structures, we were able to study not only the lotus effect, but also another type of superhydrophobicity − the petal effect. These two effects both inhibit water from spreading, but they differ in the adhesion to water. When experimenting with one of the EBL techniques, we realized we had the ability to precisely control the hierarchical structures, so we tried making asymmetric hierarchical structures to study directional wicking. After finding out that that was not a good design for asymmetric wick device, we switched to tilted-fins-decorated microfluidic channels and successfully demonstrated asymmetric wicking.

We can start to see patterns: (1) Corners are important, because corners represent surface curvatures, or excess of surface areas. In **Chapter 2** (Capillary Force Lithography), a corner can be regarded as being able to exert a virtual pulling force that reshapes the meniscus. Sharpness of the corners is important in determining the shape a meniscus adopt. In **Chapter 3** (superhydrophobic surfaces), the transition between the top and the sidewall is an important indication of the slope of the sidewall, which dictates the adhesion between a fluid and a surface. Again, sharpness of the corners is important in determining the wetting property. In **Chapter 4** (wicking channels), a corner represents asymmetry, e.g., the tilting angle, and thus controls the fluid motion. (2) The Rayleigh-Plateau instability is important. It is intimately connected to corners, and it manifests itself, in many cases, as a "wedge" effect − basically, too tight of a wedge produces instability. (3) Geometry of the boundary influence the global behavior of a system, because the system as a whole is small enough to be viewed as the vicinity of the boundary.

At the end of this dissertation as I look back and review all these interesting projects and think of the many other intriguing phenomena related to surface tension, I realized the fact that the capillary length of water on earth is 2.7 mm may be significant. Small-scale (a few millimeters and below) systems are influenced much more significantly by surface tension than everyday objects, and as a result, they behave much differently than the way fluid flows at large scales (several centimeters and above). The transition between these two "world" is right at our finger tips. The easy access to the "small" scale with modern microscopy and micro-fabrication techniques make it possible to arrange assemblies of micro- and/or nano- scale objects such that they exhibit collective properties at the macroscopic scale.

Looking forward, I think continuations of the studies presented in this dissertation may include: (1) For the CFL project, since right now the main limiting factor is the mechanical properties of the imprinted materials, when new materials with structural strength and suitable for imprinting are developed, they should be experimented to see whether sharp corners can be preserved. (2) For the SHS project, although we know that the profile of the secondary features are important, we have not achieved consistent control over the sidewall slope in fabrications. More advanced EBL or charged-particle lithographic techniques may be needed for that purpose. (3) For the wicking channel project, there are two aspects

that can be improved. First, microscope images of the meniscus during fluid propagation should be added to serve as direct evidence of the purposed mechanism and to provide more detailed quantifications during various stages of spreading. Second, a hydrophilic material or surface treatments should be applied to the fabrication of the devices so that they are more suitable for aqueous solution.

BIBLIOGRAPHY

K. Autumn, Y. A. Liang, S. T. Hsieh, W. Zesch, W. P. Chan, T. W. Kenny, R. Fearing, and R. J. Full, "Adhesive force of a single gecko foot-hair", Nature, vol. 405, no. 6787, pp. 681−685, Jun. 2000.

T. Baldacchini, J. E. Carey, M. Zhou, and E. Mazur, "Superhydrophobic Surfaces Prepared by Microstructuring of Silicon Using a Femtosecond Laser", Langmuir, vol. 22, no. 11, pp. 4917−4919, May 2006.

D. R. Ballerini, X. Li, and W. Shen, "An inexpensive thread-based system for simple and rapid blood grouping", Anal. Bioanal. Chem., vol. 399, no. 5, pp. 1869−1875, Feb. 2011.

W. Barthlott, T. Schimmel, S. Wiersch, K. Koch, M. Brede, M. Barczewski, S. Walheim, A. Weis, A. Kaltenmaier, A. Leder, and H. F. Bohn, "The Salvinia Paradox: Superhydrophobic Surfaces with Hydrophilic Pins for Air Retention Under Water", Advanced Materials, vol. 22, no. 21, pp. 2325−2328, 2010.

A. Bateni, A. Ababneh, J. A. W. Elliott, A. W. Neumann, and A. Amirfazli, "Effect of gravity and electric field on shape and surface tension of drops", Advances in Space Research, vol. 36, no. 1, pp. 64−69, 2005.

K. Beard, "Terminal Velocity and Shape of Cloud and Precipitation Drops Aloft", J. Atmos. Sci., vol. 33, no. 5, pp. 851−864, 1976.

D. J. Beebe, G. A. Mensing, and G. M. Walker, "Physics and applications of microfluidics in biology", Annu. Rev. Biomed. Eng., vol. 4, pp. 261−286, 2002.

B. Bhushan, Y. C. Jung, and K. Koch, "Micro-, nano- and hierarchical structures for superhydrophobicity, self-cleaning and low adhesion", Phil. Trans. R. Soc. A, vol. 367, no. 1894, pp. 1631−1672, May 2009.

B. Bhushan and Y. C. Jung, "Natural and biomimetic artificial surfaces for superhydrophobicity, self-cleaning, low adhesion, and drag reduction", Progress in Materials Science, vol. 56, no. 1, pp. 1−108, Jan. 2011.

J. Bico and D. Quere, "Self-propelling slugs", J. Fluid Mech., vol. 467, pp. 101−127, Sep. 2002.

B. Bilenberg, S. Jacobsen, M. S. Schmidt, L. H. D. Skjolding, P. Shi, P. Boggild, J. O. Tegenfeldt, and A. Kristensen, "High resolution 100 kV electron beam lithography in SU-8", Microelectron. Eng., vol. 83, no. 4−9, pp. 1609−1612, Sep. 2006.

M. L. Blow, H. Kusumaatmaja, and J. M. Yeomans, "Imbibition through an array of triangular posts", J. Phys. Condes. Matter, vol. 21, no. 46, Nov. 2009.

M. L. Blow and J. M. Yeomans, "Anisotropic imbibition on surfaces patterned with polygonal posts", Philos. Trans. R. Soc. A-Math. Phys. Eng. Sci., vol. 369, no. 1945, pp. 2519−2527, Jun. 2011.

L. F. Boesel, C. Greiner, E. Arzt, and A. del Campo, "Gecko-Inspired Surfaces: A Path to Strong and Reversible Dry Adhesives", Advanced Materials, vol. 22, no. 19, pp. 2125−2137, 2010.

K. A. Brakke, "The Surface Evolver", Experimental Mathematics, vol. 1, no. 2, pp. 141−165, 1992.

K. A. Brakke, "The surface evolver and the stability of liquid surfaces", Philos. Trans. R. Soc. Lond. Ser. A-Math. Phys. Eng. Sci., vol. 354, no. 1715, pp. 2143−2157, Sep. 1996.

C. M. Bruinink, M. Peter, P. A. Maury, M. De Boer, L. Kuipers, J. Huskens, and D. N. Reinhoudt, "Capillary force lithography: Fabrication of functional polymer templates as versatile tools for nanolithography", Advanced Functional Materials, vol. 16, no. 12, pp. 1555−1565, Aug. 2006.

P. Brunet, J. Eggers, and R. D. Deegan, "Vibration-induced climbing of drops", Phys. Rev. Lett., vol. 99, no. 14, Oct. 2007.

M. A. Burns, B. N. Johnson, S. N. Brahmasandra, K. Handique, J. R. Webster, M. Krishnan, T. S. Sammarco, P. M. Man, D. Jones, D. Heldsinger, C. H. Mastrangelo, and D. T. Burke, "An integrated nanoliter DNA analysis device", Science, vol. 282, no. 5388, pp. 484−487, Oct. 1998.

M. Byun, R. L. Laskowski, M. He, F. Qiu, M. Jeffries-EL, and Z. Lin, "Controlled evaporative self-assembly of hierarchically structured regioregular conjugated polymers", Soft Matter, vol. 5, no. 8, p. 1583, 2009.

M. Cavallaro, L. Botto, E. P. Lewandowski, M. Wang, and K. J. Stebe, "Curvature-driven capillary migration and assembly of rod-like particles", PNAS, vol. 108, no. 52, pp. 20923−20928, Dec. 2011.

A. del Campo and C. Greiner, "SU-8: a photoresist for high-aspect-ratio and 3D sub-micron lithography", Journal of Micromechanics and Microengineering, vol. 17, no. 6, pp. R81−R95, Jun. 2007.

M. Chaudhury and G. Whitesides, "How to Make Water Run Uphill", Science, vol. 256, no. 5063, pp. 1539−1541, Jun. 1992.

H. Chen, E. Kern, C. Ziegler, and A. Eychmuller, "Ultrasonically Assisted Synthesis of 3D Hierarchical Silver Microstructures", J. Phys. Chem. C, vol. 113, no. 44, pp. 19258−19262, Nov. 2009.

H. Chen, J. Cogswell, C. Anagnostopoulos, and M. Faghri, "A fluidic diode, valves, and a sequential-loading circuit fabricated on layered paper", Lab on a Chip, vol. 12, no. 16, p. 2909, 2012.

Y. Chen, B. He, J. H. Lee, and N. A. Patankar, "Anisotropy in the wetting of rough surfaces", J. Colloid Interface Science, vol. 281, no. 2, pp. 458−464, Jan. 2005.

Y. K. Chen and S. H. Collicott, "Investigation of the symmetric wetting of vane-wall gaps in propellant tanks", AIAA J., vol. 42, no. 2, pp. 305−314, Feb. 2004.

S. J. Choi and S. Y. Huh, "Direct Structuring of a Biomimetic Anti-Reflective, Self-Cleaning Surface for Light Harvesting in Organic Solar Cells", Macromolecular Rapid Communications, vol. 31, no. 6, pp. 539−544, 2010.

K. H. Chu, R. Xiao, and E. N. Wang, "Uni-directional liquid spreading on asymmetric nanostructured surfaces", Nature Materials, vol. 9, no. 5, pp. 413−417, May 2010.

P. Concus, R. Finn, and M. Weislogel, "Measurement of critical contact angle in a microgravity space experiment", Experiments in Fluids, vol. 28, no. 3, pp. 197−205, 2000.

D. R. S. Cumming, S. Thoms, S. P. Beaumont, and J. M. R. Weaver, "Fabrication of 3 nm wires using 100 keV electron beam lithography and poly(methyl methacrylate) resist", Appl. Phys. Lett., vol. 68, no. 3, pp. 322−324, Jan. 1996.

G. B. Demirel, N. Dilsiz, M. Cakmak, and T. Caykara, "Molecular design of photoswitchable surfaces with controllable wettability", Journal of Materials Chemistry, vol. 21, no. 9, p. 3189, 2011.

R. D. Desautels, E. Skoropata, Y. Y. Chen, H. Ouyang, J. W. Freeland, and J. van Lierop, "Increased surface spin stability in $\gamma-Fe_2O_3$ nanoparticles with a Cu shell", Journal of Physics: Condensed Matter, vol. 24, no. 14, p. 146001, Apr. 2012.

D. C. Duffy, J. C. McDonald, O. J. A. Schueller, and G. M. Whitesides, "Rapid prototyping of microfluidic systems in poly(dimethylsiloxane)", Anal. Chem., vol. 70, no. 23, pp. 4974−4984, Dec. 1998.

J. Dumais and Y. Forterre, "'Vegetable Dynamicks': The Role of Water in Plant Movements", Annual Review of Fluid Mechanics, vol. 44, no. 1, pp. 453−478, 2012.

D. Erickson and D. Q. Li, "Integrated microfluidic devices", Anal. Chim. Acta, vol. 507, no. 1, pp. 11−26, 2004.

J. Feng and J. P. Rothstein, "Simulations of novel nanostructures formed by capillary effects in lithography", J. Colloid Interface Sci., vol. 354, no. 1, pp. 386−395, Feb. 2011. (a)

J. Feng, M. T. Tuominen, and J. P. Rothstein, "Hierarchical Superhydrophobic Surfaces Fabricated by Dual-Scale Electron-Beam-Lithography with Well-Ordered Secondary Nanostructures", Advanced Functional Materials, vol. 21, no. 19, pp. 3715−3722, Oct. 2011. (b)

J. Feng and J. P. Rothstein, "Novel microfluidic diodes: one-way wicking in open microchannels controlled by channel topography", Submitted to Lab on a Chip, 2012.

X. J. Feng and L. Jiang, "Design and Creation of Superwetting/Antiwetting Surfaces", Advanced Materials, vol. 18, no. 23, pp. 3063−3078, 2006.

X. Q. Feng, X. Gao, Z. Wu, L. Jiang, and Q. S. Zheng, "Superior water repellency of water strider legs with hierarchical structures: Experiments and analysis", Langmuir, vol. 23, no. 9, pp. 4892−4896, Apr. 2007.

R. Finn, Equilibrium Capillary Surfaces. Springer-Verlag, 1986, Chapter 6.

R. Finn, "Capillary Surface Interfaces", Not. AMS, vol. 46, no. 7, pp. 770−781, 1990.

R. Finn, "Eight remarkable properties of capillary surfaces", The Mathematical Intelligencer, vol. 24, no. 3, pp. 21−33, 2002.

L. Gao and T. J. McCarthy, "A perfectly hydrophobic surface ($\theta_A/\theta_R = 180°/180°$)", J. Am. Chem. Soc., vol. 128, no. 28, pp. 9052−9053, Jul. 2006. (a)

L. Gao and T. J. McCarthy, "Contact angle hysteresis explained", Langmuir, vol. 22, no. 14, pp. 6234−6237, Jul. 2006. (b)

L. Gao and T. J. McCarthy, "The 'lotus effect' explained: Two reasons why two length scales of topography are important", Langmuir, vol. 22, no. 7, pp. 2966−2967, Mar. 2006. (c)

P. G. de Gennes, "Wetting: statics and dynamics", Rev. Mod. Phys., vol. 57, no. 3, pp. 827−863, Jul. 1985.

P. G. de Gennes, "The dynamics of reactive wetting on solid surfaces", Physica A, vol. 249, no. 1−4, pp. 196−205, Feb. 1998.

P. G. de Gennes, F. Brochard-Wyart, and D. Quere, "Capillarity and Wetting Phenomena: Drops, Bubbles, Pearls, Waves", Springer, 2003. Chapter 1 and 2.

C. Greiner, E. Arzt, and A. del Campo, "Hierarchical Gecko-Like Adhesives", Advanced Materials, vol. 21, no. 4, pp. 479−482, 2009.

W. Gu, X. Y. Zhu, N. Futai, B. S. Cho, and S. Takayama, "Computerized microfluidic cell culture using elastomeric channels and? Braille displays", Proc. Natl. Acad. Sci. U. S. A., vol. 101, no. 45, pp. 15861−15866, Nov. 2004.

W. Han, M. Byun, L. Zhao, J. Rzayev, and Z. Lin, "Controlled evaporative self-assembly of hierarchically structured bottlebrush block copolymer with nanochannels", Journal of Materials Chemistry, vol. 21, no. 37, p. 14248, 2011.

E. Hauser and A. Michaels, "Interfacial Tension at Elevated Pressures and Temperatures .1. a New and Improved Apparatus for Boundary-Tension Measurements by the Pendent-Drop Method", Journal of Physical and Colloid Chemistry, vol. 52, no. 7, pp. 1157−1165, 1948.

H. K. Holden and H. K. Holden, "Activated Carbon Filter", U.S. Patent 361167812-Oct-1971.

K. Holmberg, D. O. Shah, and M. J. Schwuger, "Handbook of applied surface and colloid chemistry". Wiley, 2002. pp. 219

J. M. Jung, F. Stellacci, and H.-T. Jung, "Generation of Various Complex Patterned Structures From a Single Ellipsoidal Dot Prepattern by Capillary Force Lithography", Advanced Materials, vol. 19, no. 24, pp. 4392−4398, 2007.

M. S. Khan, G. Thouas, W. Shen, G. Whyte, and G. Garnier, "Paper Diagnostic for Instantaneous Blood Typing", Anal. Chem., vol. 82, no. 10, pp. 4158−4164, May 2010.

M. Kitron-Belinkov, A. Marmur, T. Trabold, and G. V. Dadheech, "Groovy drops: Effect of groove curvature on spontaneous capillary flow", Langmuir, vol. 23, no. 16, pp. 8406−8410, Jul. 2007.

H. Ko, Z. Zhang, K. Takei, and A. Javey, "Hierarchical polymer micropillar arrays decorated with ZnO nanowires", Nanotechnology, vol. 21, no. 29, p. 295305, Jul. 2010.

K. Koch, B. Bhushan, and W. Barthlott, "Multifunctional surface structures of plants: An inspiration for biomimetics", Progress in Materials Science, vol. 54, no. 2, pp. 137−178, Feb. 2009. (a)

K. Koch, B. Bhushan, Y. C. Jung, and W. Barthlott, "Fabrication of artificial Lotus leaves and significance of hierarchical structure for superhydrophobicity and low adhesion", Soft Matter, vol. 5, no. 7, p. 1386, 2009. (b)

D. M. Koller, N. Galler, H. Ditlbacher, A. Hohenau, A. Leitner, F. R. Aussenegg, and J. R. Kren, "Direct fabrication of micro/nano fluidic channels by electron beam lithography", Microelectronic Engineering, vol. 86, no. 4−6, pp. 1314−1316, Apr. 2009.

Y. Kwon, N. Patankar, J. Choi, and J. Lee, "Design of Surface Hierarchy for Extreme Hydrophobicity", Langmuir, vol. 25, no. 11, pp. 6129−6136, Jun. 2009.

D. J. Laser and J. G. Santiago, "A review of micropumps", J. Micromech. Microeng., vol. 14, no. 6, pp. R35−R64, Jun. 2004.

B. Lautrup, "Physics of Continuous Matter: Exotic and Everyday Phenomena in the Macroscopic World", Second Edition. Taylor & Francis US, 2009. Chapter 5.

L. Lin, M. Liu, L. Chen, P. Chen, J. Ma, D. Han, and L. Jiang, "Bio-Inspired Hierarchical Macromolecule − Nanoclay Hydrogels for Robust Underwater Superoleophobicity", Advanced Materials, vol. 22, no. 43, pp. 4826−4830, 2010.

Y. W. Lin, W. L. Tseng, and H. T. Chang, "Using a layer-by-layer assembly technique to fabricate multicolored-light-emitting films of CdSe@CdS and CdTe quantum dots", Advanced Materials, vol. 18, no. 11, p. 1381−1386, Jun. 2006.

D. Lopez-Romero, C. A. Barrios, M. Holgado, M. F. Laguna, and R. Casquel, "High aspect-ratio SU-8 resist nano-pillar lattice by e-beam direct writing and its application for liquid trapping", Microelectron. Eng., vol. 87, no. 4, pp. 663−667, Apr. 2010.

A. W. Martinez, S. T. Phillips, and G. M. Whitesides, “Three-dimensional microfluidic devices fabricated in layered paper and tape”, Proc. Natl. Acad. Sci. U. S. A., vol. 105, no. 50, pp. 19606−19611, Dec. 2008.

A. W. Martinez, S. T. Phillips, Z. Nie, C. M. Cheng, E. Carrilho, B. J. Wiley, and G. M. Whitesides, “Programmable diagnostic devices made from paper and tape”, Lab Chip, vol. 10, no. 19, pp. 2499−2504, 2010.

J. A. Mattson, H. B. Mark Jr., M. D. Malbin, W. J. Weber Jr., and J. C. Crittenden, “Surface chemistry of active carbon: Specific adsorption of phenols”, Journal of Colloid and Interface Science, vol. 31, no. 1, pp. 116−130, Sep. 1969.

J. C. McDonald and G. M. Whitesides, “Poly(dimethylsiloxane) as a material for fabricating microfluidic devices”, Accounts Chem. Res., vol. 35, no. 7, pp. 491−499, Jul. 2002.

H. D. Mittelmann and A. Zhu, “Capillary surfaces with different contact angles in a corner”, Microgravity Sci. Technol, vol. 9, pp. 22−27, 1996

M. D. Morariu, N. E. Voicu, E. Sch?ffer, Z. Lin, T. P. Russell, and U. Steiner, “Hierarchical structure formation and pattern replication induced by an electric field”, Nature Materials, vol. 2, no. 1, pp. 48−52, 2003.

F. Mugele and J. C. Baret, “Electrowetting: From basics to applications”, J. Phys. Condes. Matter, vol. 17, no. 28, pp. R705−R774, Jul. 2005.

E. Munch, M. E. Launey, D. H. Alsem, E. Saiz, A. P. Tomsia, and R. O. Ritchie, “Tough, Bio-Inspired Hybrid Materials”, Science, vol. 322, no. 5907, pp. 1516−1520, Dec. 2008.

J. L. Osborn, B. Lutz, E. Fu, P. Kauffman, D. Y. Stevens, and P. Yager, “Microfluidics without pumps: reinventing the T-sensor and H-filter in paper networks”, Lab Chip, vol. 10, no. 20, 2659−2665, 2010.

D. K. Owens and R. C. Wendt, “Estimation of the surface free energy of polymers”, Journal of Applied Polymer Science, vol. 13, no. 8, pp. 1741−1747, 1969.

H. Princen, I. Y. Zia, and S. Mason, “Measurement of interfacial tension from the shape of a rotating drop”, Journal of Colloid and Interface Science, vol. 23, no. 1, pp. 99−107, Jan. 1967.

C. Py, P. Reverdy, L. Doppler, J. Bico, B. Roman, and C. N. Baroud, “Capillary Origami: Spontaneous wrapping of a droplet with an elastic sheet”, Phys. Rev. Lett., vol. 98, no. 15, Apr. 2007.

K. Rejmer, S. Dietrich, and M. Napiorkowski, “Filling transition for a wedge”, Phys. Rev. E, vol. 60, no. 4, pp. 4027−4042, Oct. 1999.

R. Roe, Bacchett.vl, and P. Wong, “Refinement of Pendent Drop Method for Measurement of Surface Tension of Viscous Liquid”, J. Phys. Chem., vol. 71, no. 13, pp. 4190, 1967.

C. Said-Mohamed, J. Niskanen, D. Lairez, H. Tenhu, P. Maioli, N. Del Fatti, F. Valle, and L.-T. Lee, “Polymer-Modulated Optical Properties of Gold Sols”, J. Phys. Chem. C, vol. 116, no. 23, pp. 12660−12669, 2012.

M. Salerno and R. Cingolani, “High throughput electron beam lithography on insulating substrates for photonic devices”, Journal of Micromechanics and Microengineering, vol. 17, no. 12, pp. 2414−2419, Dec. 2007.

F. Sauvage, F. Di Fonzo, A. Li Bassi, C. S. Casari, V. Russo, G. Divitini, C. Ducati, C. E. Bottani, P. Comte, and M. Graetzel, “Hierarchical TiO_2 Photoanode for Dye-Sensitized Solar Cells”, Nano Letters, vol. 10, no. 7, pp. 2562−2567, Jul. 2010.

J. Shieh, F. J. Hou, Y. C. Chen, H. M. Chen, S. P. Yang, C. C. Cheng, and H. L. Chen, "Robust Airlike Superhydrophobic Surfaces", Advanced Materials, vol. 22, no. 5, p. 597−601, Feb. 2010.

R. Shuttleworth, "The Surface Tension of Solids," Proceedings of the Physical Society. Section A, vol. 63, no. 5, pp. 444−457, May 1950.

T. M. Squires and S. R. Quake, "Microfluidics: Fluid physics at the nanoliter scale", Rev. Mod. Phys., vol. 77, no. 3, pp. 977−1026, Jul. 2005.

K. Y. Suh, Y. S. Kim, and H. H. Lee, "Capillary force lithography", Advanced Materials, vol. 13, no. 18, pp. 1386−1389, Sep. 2001.

K. Y. Suh and H. H. Lee, "Capillary force lithography: Large-area patterning, self-organization, and anisotropic dewetting", Advanced Functional Materials, vol. 12, no. 6−7, pp. 405−413, Jun. 2002.

K. Y. Suh, P. Kim, and H. H. Lee, "Capillary kinetics of thin polymer films in permeable microcavities", Applied Physics Letters, vol. 85, no. 18, pp. 4019−4021, Nov. 2004.

D. E. Sullivan, "Surface tension and contact angle of a liquid−solid interface", The Journal of Chemical Physics, vol. 74, no. 4, pp. 2604−2615, Feb. 1981.

G. Vazquez, E. Alvarez, and J. Navaza, "Surface-Tension of Alcohol Plus Water from 20°C to 50°C", J. Chem. Eng. Data, vol. 40, no. 3, pp. 611−614, Jun. 1995.

B. Vonnegut, "Rotating Bubble Method for the Determination of Surface and Interfacial Tensions", Review of Scientific Instruments, vol. 13, no. 1, p. 6, 1942.

W. Wang, R. Xie, X.-J. Ju, T. Luo, L. Liu, D. A. Weitz, and L.-Y. Chu, "Controllable microfluidic production of multicomponent multiple emulsions", Lab on a Chip, vol. 11, no. 9, p. 1587, 2011.

G. S. Watson, B. W. Cribb, and J. A. Watson, "How Micro/Nanoarchitecture Facilitates Anti-Wetting: An Elegant Hierarchical Design on the Termite Wing", ACS Nano, vol. 4, no. 1, pp. 129−136, Jan. 2010.

G. M. Whitesides, "The origins and the future of microfluidics", Nature, vol. 442, no. 7101, pp. 368−373, 2006.

H. Wong, S. Morris, and C. Radke, "Three-dimensional menisci in polygonal capillaries", Journal of Colloid and Interface Science, vol. 148, no. 2, pp. 317−336, Feb. 1992.

A. H. F. Wu, K. L. Cho, I. I. Liaw, G. Moran, N. Kirby, and R. N. Lamb, "Hierarchical surfaces: an in situ investigation into nano and micro scale wettability", Faraday Discussions, vol. 146, p. 223, 2010.

H. Wu, D. Lin, and W. Pan, "High Performance Surface-Enhanced Raman Scattering Substrate Combining Low Dimensional and Hierarchical Nanostructures", Langmuir, vol. 26, no. 10, pp. 6865−6868, May 2010.

J. Wu, J. Xia, Y. Zhang, W. Lei, and B. Wang, "A simple method to fabricate the different extents of superhydrophobic surfaces", Physica E: Low-dimensional Systems and Nanostructures, vol. 42, no. 5, pp. 1325−1328, Mar. 2010.

Q. Xiao, T. Yang, A. Ursache, and M. T. Tuominen, "Clusters of interacting single domain Co nanomagnets for multistate perpendicular magnetic media applications", Journal of Applied Physics, vol. 103, no. 7, pp. 07C521−07C521−3, Mar. 2008.

R. Xiao, K. H. Chu, and E. N. Wang, "Multilayer liquid spreading on superhydrophilic nanostructured surfaces", Applied Physics Letters, vol. 94, no. 19, pp. 193104−193104, May 2009.

Y. Xiu, L. Zhu, D. W. Hess, and C. P. Wong, "Biomimetic Creation of Hierarchical Surface Structures by Combining Colloidal Self-Assembly and Au Sputter Deposition", Langmuir, vol. 22, no. 23, pp. 9676−9681, Nov. 2006.

Y. Xiu, S. Zhang, V. Yelundur, A. Rohatgi, D. W. Hess, and C. P. Wong, "Superhydrophobic and Low Light Reflectivity Silicon Surfaces Fabricated by Hierarchical Etching", Langmuir, vol. 24, no. 18, pp. 10421−10426, Sep. 2008.

Y. Xiu, Y. Liu, D. W. Hess, and C. P. Wong, "Mechanically robust superhydrophobicity on hierarchically structured Si surfaces", Nanotechnology, vol. 21, no. 15, p. 155705, Apr. 2010.

H. Yang and P. Jiang, "Scalable fabrication of superhydrophobic hierarchical colloidal arrays", Journal of Colloid and Interface Science, vol. 352, no. 2, pp. 558−565, Dec. 2010.

X. Yao, Q. Chen, L. Xu, Q. Li, Y. Song, X. Gao, D. Quere, and L. Jiang, "Bioinspired Ribbed Nanoneedles with Robust Superhydrophobicity", Advanced Functional Materials, vol. 20, no. 4, pp. 656−662, 2010. (a)

X. Yao, L. Xu, and L. Jiang, "Fabrication and Characterization of Superhydrophobic Surfaces with Dynamic Stability", Advanced Functional Materials, vol. 20, no. 19, pp. 3343−3349, 2010. (b)

A. L. Yarin, "Drop impact dynamics: Splashing, spreading, receding, bouncing...", in Annual Review of Fluid Mechanics, vol. 38, Palo Alto: Annual Reviews, 2006, pp. 159−192.

F. Zhang and H. Y. Low, "Anisotropic Wettability on Imprinted Hierarchical Structures", Langmuir, vol. 23, no. 14, pp. 7793−7798, Jul. 2007.

G. Zhang and D. Wang, "Colloidal Lithography − The Art of Nanochemical Patterning", Chemistry − An Asian Journal, vol. 4, no. 2, pp. 236−245, 2009.

W. Zhao, L. Wang, and Q. Xue, "Fabrication of Low and High Adhesion Hydrophobic Au Surfaces with Micro/Nano-Biomimetic Structures", J. Phys. Chem. C, vol. 114, no. 26, pp. 11509−11514, Jul. 2010.